MULTIVARIATE ANALYSIS OF LEAF TISSUE MORPHOGENESIS

A Dissertation

Submitted to the Faculty

of

Purdue University

by

Samuel A. Belteton

In Partial Fulfillment of the

Requirements for the Degree

of

Doctor of Philosophy

May 2020

Purdue University

West Lafayette, Indiana

THE PURDUE UNIVERSITY GRADUATE SCHOOL
STATEMENT OF DISSERTATION APPROVAL

Dr. Daniel B. Szymanski, Chair

Department of Botany and Plant Pathology

Dr. Christopher J. Staiger

Department of Botany and Plant Pathology

Dr. Anjali S. Iyer-Pascuzzi

Department of Botany and Plant Pathology

Dr. David M. Umulis

Department of Agricultural and Biological Engineering

Approved by:

Dr. Jason R. Cannon

Head of the School Graduate Program

Dr. Christopher J. Staiger

Head of Botany and Plant Pathology

Dedicated to my parents who sacrificed too much.

ACKNOWLEDGMENTS

I would like to thank Dan Szymanski for his mentoring throughout my PhD work. There are a lot good memories from working in your lab that I will always carry with me. I would also like to thank my graduate committee; Dr. Anjali S. Iyer-Pascuzzi, Dr. Christ Staiger, and Dr. Umulis for their feedback and patience.

I want to thank all the undergrads that I had the privileged of mentoring. I especially want to thank previous and current members of the lab; Makoto, Zach, Uma, Youngwoo, and Eileen. You made the lab a second home.

Finally, I want to thank Liz for your patience and being my support during difficult times. To my brother David and my sister Nancy for being a constant source of inspiration and admiration. To my parents, Gloria and Samuel, thank you for all your support and for always believing in me. You always see the best version of me.

TABLE OF CONTENTS

Page

Page

LIST OF TABLES

LIST OF FIGURES

ABSTRACT

Belteton, Samuel A. Ph.D., Purdue University, May 2020. Multivariate analysis of leaf tissue morphogenesis. Major Professor: Daniel B. Szymanski.

Leaf size and shape are strongly influenced by the growth patterns of the epidermal tissue. Pavement cells are the prevalent cell type in the epidermis and during cell expansion they undergo a drastic shape change from a simple polyhedral cells to puzzled-shaped cell. The role of these cell protrusions, more commonly referred to as lobes, remains unknown but their formation has been proposed to help increase the structural integrity of the epidermal tissue. How the symmetry breaking event that initiates a lobe is controlled remains unknown, however pharmacological and genetic disruption of the microtubule system has been shown to interfere not only with lobe initiation but also with lobe expansion. Additionally, the role of microtubules in the pattering of microfibril deposition, the load-bearing structure of the cell wall, makes the microtubule system a good candidate to evaluate its dynamics as a function of shape change. Two main mechanical models for lobe initiation are evaluated here, one where microtubules serve as stable features suppressing local expansion and one where microtubules, similarly to the anisotropic expansion patterning in hypocotyl cells, promote the local anisotropic expansion of the cell resulting in lobe formation. The main method to evaluate these models was through the use of long-term time-lapse image analysis using a plasma-membrane marker for accurate shape change quantification and a microtubule marker to quantify their location, persistence, and density as a function of cell shape change. Using the junctions where three cells come together, cells were sub-divided into segments and the shape of these segments were tracked using a new coordinate system that allowed the detection of new lobes as which can arise from $\sim$300 deflections. By mapping sub-cellular processes, such as microtubule

persistence, to this coordinate system, correlations of microtubule organization and shape change was possible. Additionally, a subset of microtubules bundles that splay across the anticlinal and periclinal walls, perpendicular and parallel to the leaf surface respectively, were identified as marking the location and direction of lobe formation. Disrupting the cell boundary by partially digesting pectin, a main component in the middle lamella, revealed the cell-autonomous morphogenesis mechanism in pavement cells. Under pectinase treatment, cell invaginations were produced and similarly to lobes their initiation was microtubule and cellulose dependent. Lastly, stress prediction using finite-element models, based from live-cell images, co-localized regions of high cell wall stress with both microtubule persistence and shape shape locations in both lobing and invaginated segments. Together, a model of cellular shape change is presented where microtubules translate cell wall stresses to tissue morphogenesis.

1. INTRODUCTION

1.1 The morphogenesis of the plant epidermal tissue

The leaf is the location where most of the photosynthetic reactions take place and its size is strongly correlated with gross primary production [1]. Being such a crucial organ in plants, understanding how its size and shape is controlled has been an active field of plant biology. While acting as a protective tissue that surrounds the underlying photosynthetic cells, the epidermis tissue of the leaf must remain flexible enough to withstand constant mechanical perturbations such as those from high wind and insect herbivory. Central to this thesis, the epidermis tissue act as a biomechanical shell that has a very important role in the restriction or promotion of organ level growth. In classic experiments using the transmembrane brassnisosteroid receptor mutant, *bri1* - which has a dwarf phenotype, normal seedling growth was restored when a functional protein was targeted exclusively to the epidermis layer [2].

A major unanswered question is to understand how cell growth behaviors can scale to influence tissue - and organ-level phenotypes. At the cellular level, the prominent cell type of the epidermal tissue, the pavement cell, undergoes a drastic shape change from a simple polyhedral cell to a puzzle-shaped cell. While not universal, the majority of plant species develop lobed-shape pavement cells [3]. The importance of these cell protrusions is not known, but it has been hypothesized that a lobed cell shape might increases the structural integrity of the epidermis tissue or coordinate local polarized growth to affect organ level shape change [4].

Understanding the biomechanics and cytoskeletal programming of lobed pavement cells is a longstanding challenge in the field. Unlike other morphogenesis systems, such as root hairs or trichomes, these cells are glued to its neighboring cells via a pectin-rich middle lamella (Fig 1.1 B,C). Lobe formations events are episodic [5,6] and these

periods that are permissive for lobe formation have been shown to occur during at at 1-2, and 5-7 days after germination. In-between these periods of lobe formation, isotropic expansion periods occur where the cell shape remains relative unchanged. Adding to this complexity, the areal growth rates between neighboring cells [7] and even the growth rates of the cell walls within a cell can vary greatly [5, 8]. The complexity has not been adequately accounted for in the literature, and presently it is not possible to create predictions on how, when, or why lobes form.

Leaf epidermal cells provide an excellent model system to analyze multi-scale growth control processes in which the activities of protein complexes and intracellular polymers scale-up to control morphogenesis at cell and organ-level spatial scales. Cell wall growth is defined as the irreversible expansion of the cell after turgor pressure exceeds the cell wall's yielding threshold [9]. To avoid rupture, the cell wall must be reinforced. Cellulose fibers are the main load-bearing elements of plant cells and microtubule organization directs their deposition serving as track for cellulose synthase [10]. During cell expansion, if the deposition of cellulose is random such as in the case of the cellulose synthesis mutant *any1*, the shape of the cell expands in an isotropic, equal in all directions, manner occasionally bursting [11]. The same isotropic cell expansion is seen when seedlings are treated with oryzalin, a well know microtubule de-polymerizing drug [12] and with treatment with isoxaben, a chemical that blocks the delivery of cellulose synthase to the plasma-membrane [13]. This disruption of shape is not exclusive to the cellulose and microtubule system. For example, the *SPIKE1* null mutant, a guanine exchange factor upstream of the *ARP2/3* complex and a key player for cortical actin organization [14], has a lobeless pavement cell phenotype [15]. It is also critical to distinguish between lobe formation and lobe maintenance/expansion mechanism. The former is the ability for a cell to create local protrusion and the latter is the mechanism which expands or maintains the already form lobe. The lack of spatiotemporal developmental shape analysis in the literature has led to confusion, misinterpretation, and numerous highly divergent view of how this process is programmed. For example, population level analysis of cells at un-

known developmental stages has led to mutants that affect cell size, lobe initiation, or lobe outgrowth all being classified as lobe initiation genes [16–19]

from either genetic or pharmacological studies prevents separating these possibly different mechanisms. A benefit of utilizing these cells to quantify how sub-cellular process affect cell and even organ shape change is that unlike animal cells whose shape are highly flexible, plant cells maintain their shape due to the rigid material of the cell wall.

1.2 Mechanical models for lobe formation

Mechanical models for lobe initiation vary depending based on the analysis performed. One of the leading models for cell interdigitation comes from epithem-cells of the hydathodes in *Pilea cadierei* [20]. Microtubules were found at locations where the once polyhedral cell had obtained a sinuous periphery and increased the extracellular spaces between cells. This model was then extrapolated to the epidermis of the leaves of the fern *Vigna sinensis* [21]; where cell pads were created at the junction of the anticlinal and outer-periclinal wall (See Fig 1.3 for cell wall locations). In both of these cell types, the interpretation was that microtubules act as stable long-lived tracks for cellulose deposition. This in turn, results in local thickening of the cell wall restricting its expansion and the surrounding regions would expand creating the flanks of these lobes (Fig 1.2). There are several concerns with this interpretation. First, while the cell pads seen in *Vigna sinensis* epidermis were spatially correlated with microtubule presence, the cell wall thickening did not continue to the entire of the anticlinal wall height. Second, while there was strong evidence of microtubule dependent shape change, it was not clear if the microtubule organization preceded the lobe formation or if it was established after the feature was established. Although limited primarily to TEM and light microscopy analysis of fixed cells, these studies provided a good starting point to evaluate shape change and identify putative molecular players that might be involved.

Assumptions based on commonly observed, although not universal, microtubule organization at the convex side of a lobe apex promoted a growth restriction model for lobe formation (Fig 1.2). Snapshots of lobed cells with microtubule markers have shown that outer-periclinal microtubules are often observed at the convex side of a lobe apex, which is consistent with the results from *Vigna sinensis* leaves [16, 22]. Unfortunately, even without time-lapse analysis of the microtubule organization, the local growth restriction model became the framework unto which the *PIN* based patterning of *ROP* GTPase signal pathway was mapped. In these model analysis already lobed cells were used to investigate the organization of the cytoskeleton and their patterns were assumed to have remained unchanged prior to lobe formation, a more detail breakdown of the *PIN* model is presented in chapter 2. Limited time-lapse analysis of microtubule patterns in lobing cells by Armour et al, 2015, reinforced the model of stable microtubules at lobing regions. In this study, the analysis of microtubule organization prior to lobe detection was limited to one time-point and population level analysis of the microtubule at the apex of a lobe used both newly formed and established lobes. The problem with this approach is that it combines two potential different mechanisms of lobe formation and lobe maintenance.

Another approach to analyze epidermal cell morphogenesis has been focused on examining the mechanical properties of the cell wall and how its local composition can lead to symmetry breaking events. To more efficiently analyze the hypothesis of cell morphogenesis as a consequence of locally modified cell wall mechanical properties, finite element modeling has proved to be an indispensable tool. Finite element (FE) modeling refers to a computer simulation based on the known physical behaviors of thin-walled pressurizing shells in response to physical stresses on the system. The surface of the shell is divided into a mesh of discrete elements, and at each element node, the distortion of the material (strain) in response to an internal pressurization force on the material (stress) is calculated using neo-Hookean models of a deformable solid. The FE model is appropriate for thin walled pressurized plant cells, and can be adapted to any geometry. In pollen tube cells [23] and in trichome cell branches [24]

this type of simulation has been successful in obtaining insights about the required subcellular cell wall composition or cytoskeletal organization of the cell required to obtain the observed shape change. The power of the system comes from the predictions of the model that suggest experiments to determine the subcellular location and type of cell wall material properties that are needed to explain growth patterns. Unlike the aforementioned cells, leaf epidermal cells are in contact with several cells that are growing at different rates [5, 8]. Despite this complexity, simplified finite element modeling has put forth two main mechanism for lobe formation; symmetry breaking due to growth restriction driven by cell wall stresses [25] and symmetry breaking due to cell wall buckling under compressive stresses at the anticlinal wall [26].

Simulations of hypothetical cells of varying shape complexity resulted in predicted stresses patterns that decreased with an increase of lobes [27]. It was then hypothesized that as the cell expands local regions of the wall were restricted to give rise to lobe formations which would compensate for the increased cell wall stresses. By looking exclusively at the anticlinal wall, an alternating pattering of cell wall stiffness under tension stress produces undulations along the wall [25]. However, recent evaluation of this modeling scheme with published parameters, only resulted in a small fraction of magnitude change in the shape [28]. More importantly when a 3D cell model was constructed by incorporating the periclinal walls the slight shape change was completely undetected. An alternative model of symmetry breaking events was proposed when 3D cell clusters were pressurized and compressive forces were predicted [26] (Fig 1.3). Further evaluation using box shape cells, these compressive forces resulted in buckling to occur which was seen as an initial method for lobe formation. However, this force was not enough to explain the growth of these features and the involvement of microtubules as the driving force for lobe elongations rather than initiation was proposed. Reliable experimental methods to analyze sub-cellular material properties are necessary to evaluate if these compressive forces exist. There presently is no genetic data to support this model either.

While finite element modeling can provide informative data, it is useful only if biologically relevant validation and refinement modeling is conducted. The trend of using finite element model on the epidermal tissue can be distilled to the following: simulations of simple shape cells and extrapolating the obtained mechanical data to lobed cells. Stress is highly dependent on the shape of the cell, but also the morphology of its neighbors; the patterns obtained after lobes have been formed most likely do not reflect that stress prior to lobe initiations. This highlights the importance of time-lapse imaging and accurate cell shape outlines to establish the state of the tissue prior to shape change, but also to monitor how these changes affect the sub-cellular stress and cytoskeletal organization.

Lobes emerge as small ∼300 nm deflections in the anticlinal cell wall boundary that appear at time-scales of 10s of minutes [29]. The lack of high-temporal and -spatial resolution time-lapse analysis of pavement cells shape change has limited the field. Additionally, lack of time resolved cytoskeletal protein location in these lobing cells has been very limited and specially prior to lobe initiation. Without clear patterns prior to lobe initiation it is difficult to evaluate how these sub-cellular systems direct cellular morphogenesis. Here, the growth restriction model (Fig 1.2) will be evaluated by first accurately investigating the shape phenotype of mature pavement cells from key players in the *PIN*-centric restriction model using a newly developed cell shape algorithm. To analyze the stability of microtubules, long-term analysis of microtubules at the anticlinal wall as a function of location and time was performed. Lastly, the evaluation of the local anisotropic cell expansion mechanical model (Fig 1.4) will be conducted. In this model, microtubules serve as tracks for microfibril deposition, controlling the local expansion in a small patch of the outer periclinal wall. This model is based on known cell expansion patterns such as those seen in hypocotyl cells where the microfibril alignment restricts radial expansion while axial expansion, which is perpendicular to microfibril alignment, is permitted. Similarly, in pavement cell persistent microfibril deposition would restrict cell expansion in the direction of the microfibrils but the expansion transversely to them would be

permissive leading to a lobe formation. To evaluate this model, long-term high-spatial and -temporal analysis was conducted in double-tagged transgenic line in which the plasma-membrane marker was utilized for accurate cell periphery quantification and a microtubule marker to utilized to track their location. A new method to quantify the shape change of the cell periphery was developed (Chapter 4) and microtubule localization was correlated to these sites of lobe formation. To evaluate the patterning of microtubules, a 3D finite element model was built from live-cell images prior to lobe formation. Finally, partial degradation of pectin in the middle lamella provided a way to interfere with cell boundary conditions providing a new method to analyze cellular morphogenesis in uncoupled cells (Chapter 4).

1.3 Figures

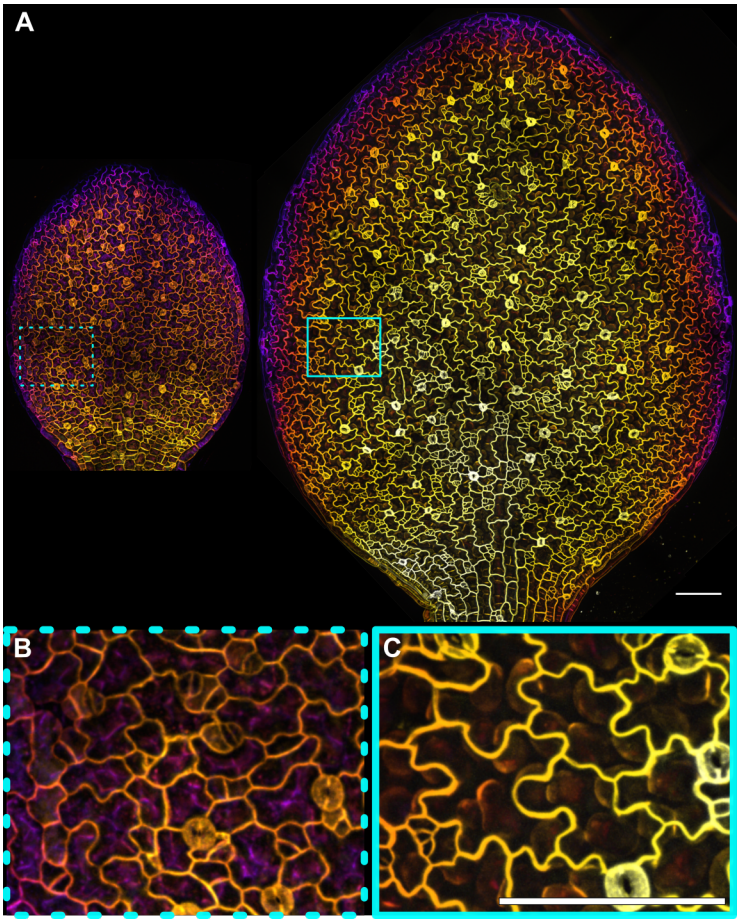

Fig. 1.1. Organ and cell level shape change in *A. thaliana* cotyledons. (A) Representative cotyledons at 1 days after germination (DAG) [left] and 2 DAG [Right]. (B) Representative pavement cell morphology at 1 DAG. (C) Representative pavement cell morphology at 2 DAG, showing an increased in cell area and lobe formation/expansion. Scale bars = 100 μm.

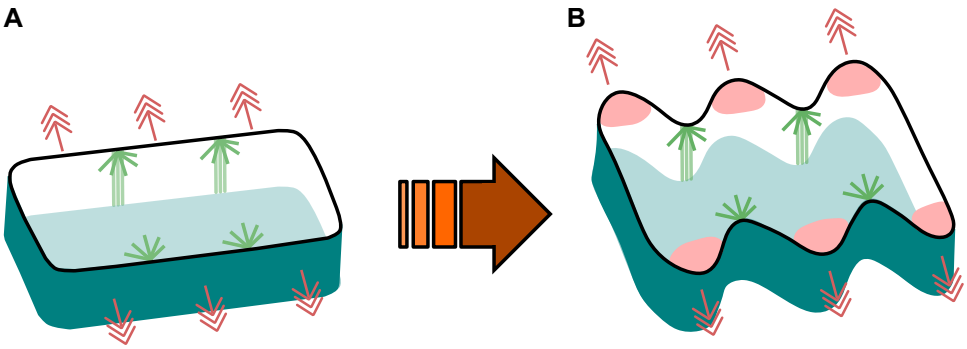

Fig. 1.2. Growth restriction model for lobe formation. (A) Stable microtubules at the anticlinal and outer-periclinal wall locally restrict cell expansion. (B) Local restriction in an expanding cell where adjacent unrestricted regions expand creating the undulated cell shape phenotype. Modified from [30].

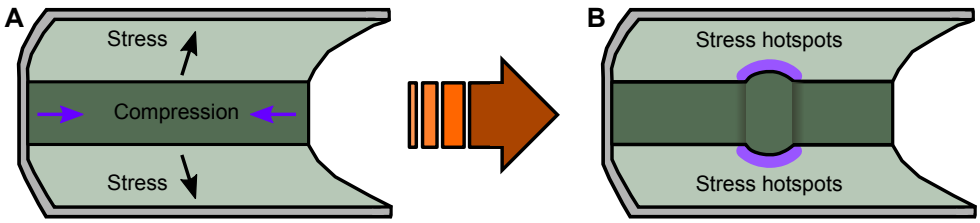

Fig. 1.3. Lobe formation due to cell buckling. (A) Stress directed towards the outer- and inner-periclinal wall produces compression forces on the anticlinal wall. (B) Symmetry breaking events due to compression forces produces regions of high cell wall stresses which are amplified by the response of the microtubules system. Modified from [26].

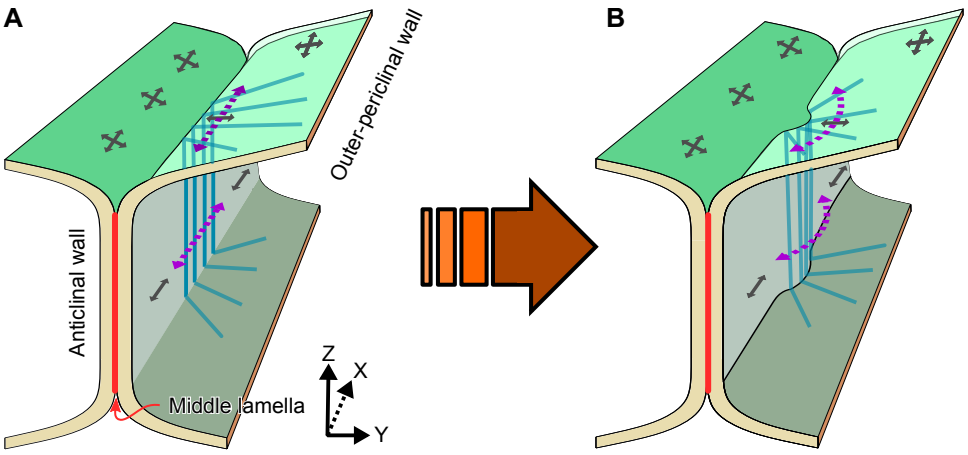

Fig. 1.4. Local anisotropic expansion model for lobe formation. (A) Mechanical model for lobe formation where microtubules serving as tracks for microfibril deposition promote the local expansion perpendicular to the microfibril alignment. (B) Persistent anisotropic expansion creates symmetry breaking events at both the anticlinal and outer-periclinal wall resulting in lobe formation.

2. LOBEFINDER

Chapter 2 was published in Plant Physiology in August 2016. The author contributions are as follows. David Umulis and Daniel Szymanski conceived the image-analysis method. Tzu-Ching Wu wrote the LobeFinder code. Samuel Belteton generated the image data and evaluated the code and its outputs. Daniel Szymanski, David Umulis, Tzu-ching Wu, and Samuel Belteton wrote the article.

Breakthrough Technologies

LobeFinder: A Convex Hull-Based Method for Quantitative Boundary Analyses of Lobed Plant Cells[1][OPEN]

Tzu-Ching Wu[2], Samuel A. Belteton[2], Jessica Pack, Daniel B. Szymanski*, and David M. Umulis*

Department of Agricultural and Biological Engineering (T.-C.W., J.P., D.M.U.), Department of Botany and Plant Pathology (S.A.B., D.B.S.), Department of Agronomy (D.B.S.), Department of Biological Sciences (D.B.S.), and Weldon School of Biomedical Engineering (D.M.U.), Purdue University, West Lafayette, Indiana 47907

ORCID ID: 0000-0001-5462-524X (J.P.).

Dicot leaves are composed of a heterogeneous mosaic of jigsaw puzzle piece-shaped pavement cells that vary greatly in size and the complexity of their shape. Given the importance of the epidermis and this particular cell type for leaf expansion, there is a strong need to understand how pavement cells morph from a simple polyhedral shape into highly lobed and interdigitated cells. At present, it is still unclear how and when the patterns of lobing are initiated in pavement cells, and one major technological bottleneck to addressing the problem is the lack of a robust and objective methodology to identify and track lobing events during the transition from simple cell geometry to lobed cells. We developed a convex hull-based algorithm termed LobeFinder to identify lobes, quantify geometric properties, and create a useful graphical output of cell coordinates for further analysis. The algorithm was validated against manually curated images of pavement cells of widely varying sizes and shapes. The ability to objectively count and detect new lobe initiation events provides an improved quantitative framework to analyze mutant phenotypes, detect symmetry-breaking events in time-lapse image data, and quantify the time-dependent correlation between cell shape change and intracellular factors that may play a role in the morphogenesis process.

The size, shape, and angle of leaves are important adaptive traits in natural populations and key determinants of yield in agronomic settings (Zhu et al., 2010). Therefore, it is important to understand the cellular events that collectively, at the levels of the tissues and organs, lead to the formation of durable, lightweight, and appropriately sized leaf blades for efficient light capture (Walter et al., 2009). In Arabidopsis (*Arabidopsis thaliana*), the growth properties of the epidermis may have particular importance in terms of organ size control (Savaldi-Goldstein et al., 2007), and the growth behaviors of the sectors of the epidermis and individual cells can correlate with organ-level growth behaviors (Zhang et al., 2011; Kuchen et al., 2012). In dicots, the basic cellular unit of the epidermis is the jigsaw puzzle piece-shaped pavement cell, the division and expansion of which drive leaf expansion (Asl et al., 2011).

The biomechanics of pavement cell shape change are complicated (Panteris and Galatis, 2005; Geitmann and Ortega, 2009; Szymanski and Cosgrove, 2009; Szymanski, 2014). Turgor pressure is the driving force for cell expansion. However, the magnitude and directions of cell wall tension forces are difficult to predict because of the presence of adjacent neighboring cells both in the plane of the epidermis and in the underlying mesophyll tissue (Szymanski, 2014). The shape of the cell itself also may influence the stress patterns in the wall, and regions of high cell curvature are predicted to have increased wall stress compared with other domains of the cell (Sampathkumar et al., 2014). The growth trajectory or strain response of the cell also is strongly influenced by heterogeneity in the cell wall, and a current challenge is to understand how differences in cell wall thickness and local cellulose-dependent cell wall anisotropy might contribute to polarized growth in this cell type (Panteris and Galatis, 2005; Szymanski, 2014).

The developmental control of lobe initiation in cotyledons and leaves also is poorly understood. In one early model, lobe initiation was proposed to direct organ shape, with cell elongation and lobe initiation occurring independently in populations of cells to influence organ growth in length and width, respectively (Tsuge et al., 1996; Fu et al., 2002). Other studies, which relied on cell shape measurements from populations of unsynchronized cells, detected correlations between cell size and lobe number, implying a continuous process of cell expansion and lobe initiation (Qiu et al., 2002; Fu et al., 2005). Neither of these models appears to be correct, based on several recent studies that employ either long-term time-lapse imaging of pavement cell morphogenesis

[1] This work was supported by the National Science Foundation (grant nos. IOS/MCB 1249652 and MCB 1121893 to D.B.S.).

[2] These authors contributed equally to the article.

* Address correspondence to dszyman@purdue.edu and dumulis@purdue.edu.

The author responsible for distribution of materials integral to the findings presented in this article in accordance with the policy described in the Instructions for Authors (www.plantphysiol.org) is: David M. Umulis (dumulis@purdue.edu).

D.M.U. and D.B.S. conceived the image-analysis method; T.C.-W. and J.P. wrote the LobeFinder code; S.A.B. generated the image data and evaluated the code; D.B.S., D.M.U., S.A.B., and T.C.-W. wrote the article.

[OPEN] Articles can be viewed without a subscription.

www.plantphysiol.org/cgi/doi/10.1104/pp.15.00972

(Zhang et al., 2011; Elsner et al., 2012) or cell population analyses that analyzed cells from developmentally staged leaves over time intervals spanning days (Andriankaja et al., 2012) or weeks (Staff et al., 2012). The clear outcome from these studies is that the frequency of lobe initiation clearly depends on the developmental stage and location on the leaf. However, in many instances, lobe initiation is unpredictable. For example, a given cell's anticlinal (perpendicular to the leaf surface) walls are in contact with several neighboring cells. New lobes can form along either one or several of these cell boundaries, and the factors that define the probability of forming a new lobe at a particular location are not known. Lobe initiation, therefore, is episodic, and morphogenesis appears to include both anisotropic growth during lobe initiation and lobe expansion as well as extended phases of symmetrical cell expansion in which the cell size increases but the overall geometry of the cell remains essentially unchanged (Zhang et al., 2011).

One major limitation in the field is the lack of a robust and objective method to identify new lobes. The discussion above on the cellular and developmental control of lobe formation is based largely on the subjective evaluation of pavement cell segments as being either lobed or unlobed. This has generated confusion and variability in the literature with regard to detecting phenotypes and comparing the severity of phenotypes among different mutants. In some instances, the end points of a midline skeleton of individual pavement cells have been used to estimate lobe number (Le et al., 2006; Staff et al., 2012); however, this method is not very accurate and appears to underestimate lobe number. As an alternative, dimensionless shape descriptors like circularity ($4\pi \times$ cell area/perimeter^2), a ratio that approaches 1 for more circular cells and gets smaller as cells become more lobed, are used to test for differences among cells in the complexity of their cell shape (Kieber et al., 1993; Le et al., 2003; Djakovic et al., 2006; Le et al., 2006; Zhang et al., 2008). The major weakness of this approach is that it does not directly reflect lobe number, and there are many equally plausible explanations in which reductions in either lobe initiation or lobe expansion could lead to similar differences in cell shape complexity. In this article, we describe a highly useful convex hull-based MatLab program termed LobeFinder that operates on cell perimeter coordinates extracted from images of pavement cells and returns an array of useful cell shape data, including a value for lobe number and a map of their positions. Based on median scores of manually identified features from a diverse population of pavement cells, LobeFinder predictions outperformed the alternative method of binary image skeletonization and subjective human scoring. The development, validation, limitations, and uses of LobeFinder are described below.

RESULTS

Currently, quantification methods of lobe formation are often focused on the localization of specific factors related to cellular shape change, such as the distribution of actin filaments, the presence of anticlinal microtubule bundles, and qualitative descriptions of cell shape (Fu et al., 2002, 2005). However, because there is no known marker protein for lobe initiation, and because lobe counting results vary greatly between laboratories and among individuals (see below), there is a strong need for a standardized computational approach to measure the number and location of pavement cell lobes.

A number of commercial and open-source software applications are available to quantify the geometry of cell shapes. These methods can be broadly separated into two categories: quantification of descriptive scalar properties such as circularity, roughness, perimeter, area, etc. that describe the shape by descriptive parameters (Russ, 2002; Robert et al., 2008); and image-segmentation approaches that we broadly define here as methods that reduce the pixel information in the raw image into segments or a reduced set of data points that have greater biological meaning (Marcuzzo et al., 2008), such as converting an image of a cell into segmented regions for nucleus, cytoplasm, Golgi, endoplasmic reticulum, etc. automatically. These approaches offer a reduction in the size of the data and a transformation of pixel intensity data into classifications that directly inform the biology of the problem. The Medial Axis Transform (Staff et al., 2012) has been used to quantify pavement cell geometry. The Medial Axis Transform uses the midline points of cells to quantify cell shape differences by tracking the percentage change in angles between linear segments of the branches along the central axes or skeleton. A similar method for tracking the midline of a cell is available as the FIJI plugin AnalyzeSkeleton method (Arganda-Carreras et al., 2010; Schindelin et al., 2012).

In the analysis of pavement cell shape, the most widely used computational method to identify lobes is based on the AnalyzeSkeleton algorithm that detects the midline of irregularly shaped objects, categorizing the pixel properties of the surrounding area and choosing the best path to detect areas of image continuity. Based upon the number of neighboring pixels, some pixel points are ignored or favored over others and a skeletonized representation of the central axes of the cell's shape and structure is formed. In this method, individual cells are extracted manually from a confocal image of a field of pavement cells (Fig. 1). A midline skeleton is calculated from the binary image, and the skeleton end points are extended to the cell perimeter, depending on the magnitude of the protrusion, to map positions of predicted lobes. As shown in Figure 1, the skeletonize method is not very accurate, and only about half of the lobes that would be identified by a trained scientist are accurately identified with this method. Therefore, this method is useful in determining generalized lobing events, usually well after a new lobe has formed, but is unable to detect slight variations in wall geometry that signify recent lobing events.

Outline of LobeFinder

To overcome the limitations of the previous methods in identifying the position and number of lobes in

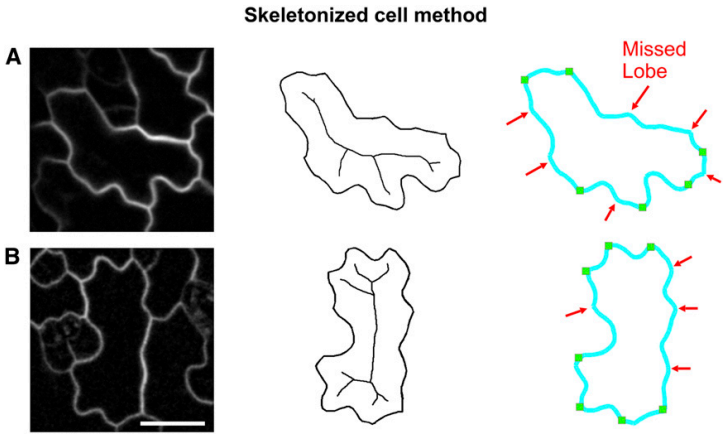

Figure 1. The AnalyzeSkeleton processing technique of lobe identification does not accurately identify pavement cell lobes. Left, Representative confocal images of early stage cotyledon pavement cells. Middle, Calculated midline skeletons of the corresponding pavement cells. Right, Summary of the accuracy of the AnalyzeSkeleton method. Green squares indicate correctly identified lobe points based on the extensions of the skeleton end points, and red arrows indicate missed lobe points compared with voting results. Bar = 20 μm.

pavement cells, we developed a new cell geometry analysis approach named LobeFinder. LobeFinder operates on user-supplied cell boundary coordinates that are extracted from high-resolution confocal images of pavement cells of various sizes and shapes. The algorithm is based on a multistep process starting with a convex hull of the cell boundary and a sequence of processing events to robustly identify lobes (Graham, 1972). First, cell boundaries are segmented from the original image. For our analysis of cell boundary variation and lobe detection, existing segmentation methods utilizing gradient vector field SNAKEs or a related approach (Ma and Manjunath, 2000; Roeder et al., 2010) were not sufficiently accurate, frequently merging cells or creating additional cells from an irregularly shaped lobe. The recently published semiautomated method for pavement cell segmentation termed CellECT improves the efficiency of three-dimensional pavement cell segmentation and includes user input to reduce errors (Delibaltov et al., 2016). In the future, CellECT could be modified to output a single set of splined coordinates that accurately depict the boundary of the anticlinal cell wall. We anticipate that as cell segmentation methods improve, LobeFinder will be integrated into an image-processing work flow to enable high-throughput cell phenotyping. However, at present, manual segmentation is the only reliable method to extract cell coordinates, and this can be easily achieved using the polygon selection tool that is available in ImageJ. The ImageJ segmentation tool is advantageous because it allows the user to adjust the position of the cell boundary points and add or delete points as needed.

For this study, confocal images were at a resolution of 3.95 or 2.55 pixels μm^{-1}. After testing a range of sampling densities along the cell perimeter, we found that sampling frequencies of 0.5 to 1.5 points μm^{-1} were sufficient to yield accurate results for cell shape analyses using LobeFinder because lobe detection was consistent in this range. Sampling frequencies of one point every 2 μm or less led to obvious mismatches between the cell shapes in the raw image and the segmented cells. We recommend sampling cell perimeters at 1 point μm^{-1} and selecting the spline function within ImageJ to smooth the manual tracing and provide a high density of interpolated points.

Following extraction of the cell perimeter by segmentation, the center of mass of each cell is calculated and moved to the origin. The overall cell size is normalized and scaled by a constant factor to calculate lobe numbers (Fig. 2A). Following analysis, the outputs are rescaled back to micrometers for the outputs reported in the graphical user interface (GUI). This allows the use of the same relative metrics and LobeFinder settings to determine if a lobe is present for cells of different ages and sizes. The normalization step also allows raw images at multiple different resolutions to be processed in LobeFinder. To remove artifacts introduced by the uneven sampling of perimeter points during manual cell segmentation and reorientation, the cell perimeter data are approximated by a cubic spline interpolation.

The output of the preprocessing steps is a cell perimeter that is scaled, aligned with the center of mass, smoothed and resampled (cubic spline interpolation), and ready for further analysis. To acquire the minimal polygon that surrounds the entire set of coordinates that define the cell boundary (Fig. 2B), we employ the MatLab function convhull, which returns the coordinates of the convex polygon (hull) that contains all the coordinate points of the cell set. The convex hull provides two important features for further analysis: first, it provides information for the minimum convex set that encompasses the entire cell; and second, it provides a convenient coordinate system onto which the cell boundary properties are easily mapped (Fig. 2B, middle). Both of these outputs will serve to subsequently identify key points and structures.

Pavement cells do not typically produce an outline where all of the extrema at the lobe tips are located precisely on the hull. For example, in Figure 2B (upper

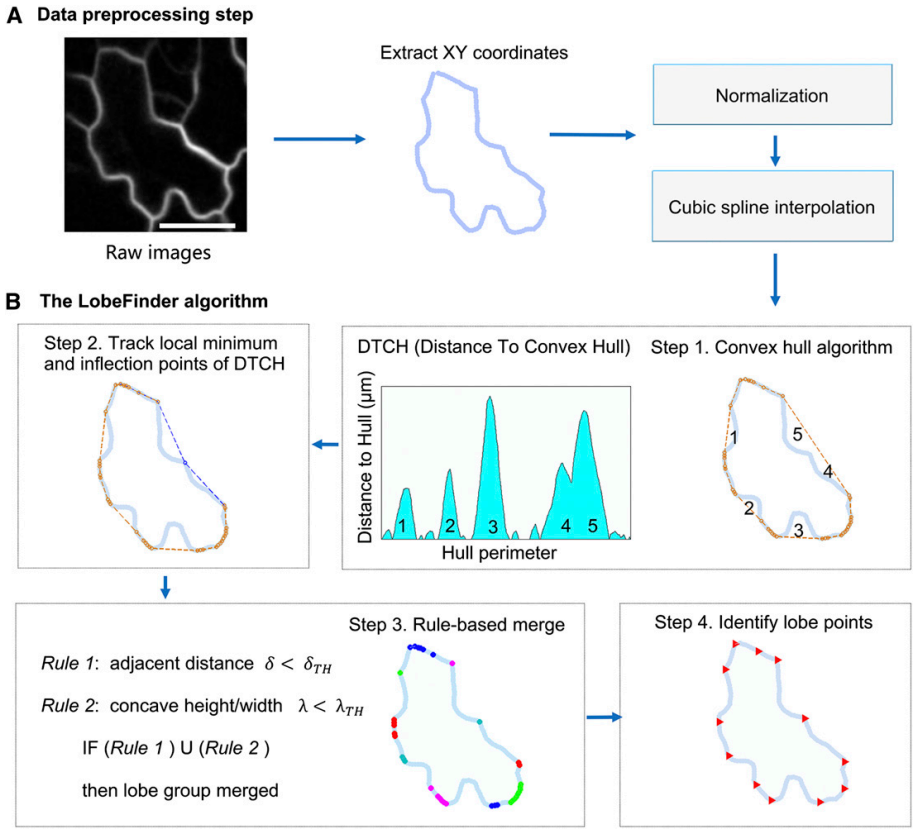

Figure 2. Overview of the LobeFinder logic and work flow. A, Cell perimeter positions are manually segmented from raw images, scaled, and resampled. Bar = 20 μm. B, A convex hull, defined as the minimal polygon that encloses the entire given cell perimeter, is computed (step 1), then the perimeter is scanned for missed lobe points (the extrema between segments 4 and 5) using the PeakFinder algorithm within MatLab (step 2). The optimized values for thresholds (δ_{TH} and λ_{TH}) for rule-based lobe geometry and spacing are used to identify putative lobe points (step 3); then, groups of lobe points are merged, and the final set of predicted lobe positions is extracted (step 4).

right), the convex hull produces a line that does not separate regions 4 and 5 by the lobe that is located between the regions, since the lobe does not land on the hull itself. To adjust the hull, the distance between the cell and the hull is calculated and plotted on an axis of position versus distance (Fig. 2B). Using the orthogonal distance to the convex hull to the cell perimeter, the local minima are retrieved, and the convex hull is then refined to capture the interior local minima points. To determine whether there are interior lobe points between adjacent points on the convex hull, we use the program PeakFinder (Yoder, 2011) to determine both local and absolute extrema between hull(i) and hull(j), points on the cell periphery coincident with the hull. PeakFinder identifies the location of the missed lobes, and the hull used to encapsulate the cell is modified to contact the lobe point (Fig. 2B, step 2). These additional processing steps capture the majority of interior lobes that would otherwise be missed, since they do not lie on the hull surrounding each cell. The resulting hull is termed the refined hull because it no longer conforms to the strict definition of a convex hull. The distance to the refined hull (DTRH) plots contain highly useful information on the local patterns of growth. Therefore, the cell and its refined hull are rescaled back to their real dimensions, and the DTRH coordinates are available to be exported within the LobeFinder program. In rare instances, there are relatively large pavement cells in which a cell lobe is bulbous. In these instances, the path of the cell perimeter doubles back on itself on one axis, creating multiple solutions for the DTRH plot. In this subregion of the cell, the PeakFinder routine uses only the smallest distance value, and this can lead to erroneous hull refinements and lobe calls. This morphology is rare in our data set, but a bulbous morphology is the default state in the crenulated boundary of many

monocot leaf epidermal cells. For these species, LobeFinder would likely perform well in analyzing early events associated with lobe initiation but likely would fail to accurately count the lobes of fully expanded cells.

Following adjustment of the convex hull, the goal of the algorithm is to identify which of the points on the cell perimeter correspond to the positions of the protrusions. Additionally, not every point on the hull corresponds to a physical lobe on the pavement cell, and to some extent, the identification of a lobe on the cell is subjective in nature, with different individuals identifying different lobe positions and numbers. One design goal of the algorithm is to mimic the expert observer's approach to identify the geometric features, albeit by an objective computer algorithm. This goal informed the design of the geometric parameters for lobe geometry and spacing that were developed to optimize lobe identification. For each data point in the set of convex hull points (Fig. 2B, step 3), the distance between neighboring points is calculated. This distance between hull points determines if the algorithm should consider adjacent lobe points as part of the same lobe. To cull points on the hull and leave only those that are identified as the center of a lobe, two parameters (δ and λ) for the initial identification of lobes are used: the scaled spacing distance between lobe points (δ) and a ratio of the height (distance between hull and cell boundary) to the width (distance of hull segment) between prospective lobe points (λ). The distance between a lobe point and the convex hull is zero; however, there must be a region between lobes where the distance is nonzero and above some threshold value. This module of the program calibrates LobeFinder to reduce the number of misleading or incorrect lobe points on the convex hull. This calibration is effective in most cases. However, because the parameters are tuned to be sensitive for small deviations in boundary shape, cells with relatively simple shapes with extended domains of the cell boundary that are close to the threshold values for δ and λ are most likely to have false positives.

LobeFinder Optimization and Evaluation

The principal method for the identification of lobes and lobing segments in pavement cells relies on observer-based inspection and identification of lobing events. An important research goal is to standardize pavement cell phenotyping and to create an objective computational method that can accurately quantify cellular geometry and be applied to time-lapse data and large ensembles of images to efficiently calculate population statistics. Therefore, it is necessary to ensure that the algorithm produces consistent and accurate observations.

As an initial test of the sensitivity of the output to variability in an individual's choice of boundary points for cell segmentation, three pavement cells of varying sizes and shapes were manually segmented three times and analyzed using LobeFinder. For each of these cells, the area, perimeter, and circularity values for the technical replicates were either identical or differed by a fraction of 1%. For the technical replicates, the LobeFinder outputs for lobe number were more variable, with the coefficients of variation for lobe number varying between 0.06 and 0.1. This level of variabilty in the measurement of lobe number was much less than that observed when multiple individuals used subjective criteria to score an identical cell. For example, in our test population of pavement cells (Supplemental Fig. S1), the coefficient of variation for lobe number ranged from 0.03 to 0.21, with 10 of the 15 cells having a coefficient of variation greater than 0.1. In the LobeFinder program, variability in lobe number most often occurred along relatively straight cell perimeter segments with one tracing including a very small feature that was absent in another. The cause for this is discussed further below, but this result makes clear the importance of accurate sampling along the cell perimeter.

Fifteen randomly selected pavement cells (Supplemental Fig. S1) from a time-lapse data set were used to more thoroughly compare the accuracy of LobeFinder with that of existing methods. The cells had sizes that ranged from 280 to 1,588 μm^2 and circularity values that ranged from 0.32 to 0.81. We evaluated how well LobeFinder outputs of lobe number and lobe position would agree with the scores generated by researchers with experience in the analysis of pavement cell shape. For each of the images (examples shown in Fig. 3), six experienced pavement cell scientists visually inspected 8.5- $\times$ 11-inch printouts of each cell and identified lobe locations for each raw image. These data were used to determine the accuracy of lobe point position detection and to calculate the number of lobes present for each cell (Fig. 3, C and D). A few of the cells used in the calibration of LobeFinder are shown in Figure 3A. The complete set of images (Supplemental Fig. S1) and a summary of the cell and convex hull properties (Supplemental Table S1) are provided in "Supplemental Data." A summary of the LobeFinder and voter results is shown in Figure 3, E and F. We next benchmarked LobeFinder and the existing skeletonize method against the images manually curated by members of the two laboratories. The subjective nature of the manual scoring of lobe number is evident in the plots of lobe number (Fig. 3, E and F), with many cells having four or more features that were ambiguous. Therefore, the median lobe number from the manually curated data was used as a standard for comparison.

Overall, the skeletonize method greatly underestimated lobe numbers (Fig. 3E). Following an initial calibration to optimize the threshold values of δ and λ, the LobeFinder outputs for lobe number closely matched the median lobe numbers from the manually curated images (Fig. 3F). The LobeFinder lobe number error was 5.7 times lower than that of the skeletonize method (Fig. 3G). The accuracy of the manual lobe counts was similar to that of LobeFinder when averaged across all individuals (Fig. 3G); however, for a given cell, there was considerable spread in the lobe counts among the individuals (Fig. 3F). For example, the error rate among the individuals differed by more

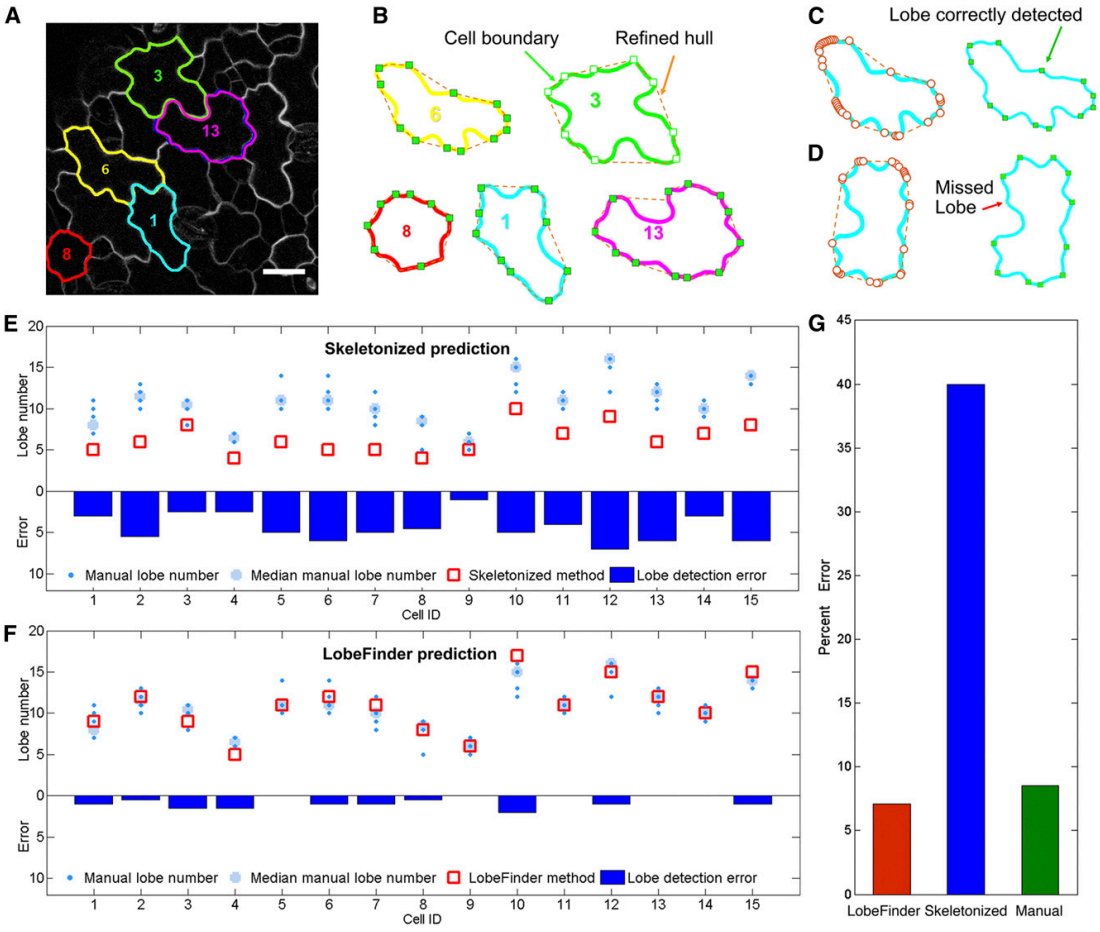

Figure 3. Evaluation of LobeFinder accuracy using a calibration data set and parameter optimization. A, Example of a raw image containing five cotyledon pavement cells in the calibration data set. Bar = 20 μm. B, Outlines of extracted cells showing the cell boundary and the unrefined convex hull. C and D, Example output of LobeFinder for two cells in which the correctly identified (green squares) and missed (red arrow) lobes are marked. E, Comparison of the skeletonize method with manually curated results. The light blue circles are the median values from manual lobe identification results for each cell, with individual independent values in small dark blue dots, and red boxes are lobe numbers predicted by the skeletonize method. The dark blue bars plot the absolute value of the differences between the lobe number count from the skeletonize method and the median value from the manual results. F, Comparison of the LobeFinder method with manually curated results. The symbols and bars are as described in E, but here, the red boxes are the lobe numbers predicted by LobeFinder. The dark blue bars are the absolute value differences between the lobe number count from LobeFinder and the median value from manual results. G, Comparison of the percentage errors of the LobeFinder, skeletonize, and manual scoring methods that were calculated using the median lobe number as the correct value for each cell.

than 20% for eight of the 15 cells, even though each of the six individuals was similarly trained to score the presence of lobes. This observation reinforces the strong need for objective methods for the quantitative analysis of cells with highly variable shapes and sizes.

Two different types of features were typically identified as a lobe. First, there were instances of an undulation along a cell perimeter segment that was independent of a three-way cell wall junction. This is the classic example of interdigitated growth among two adjacent cells, and we define these features as type I lobes. A second class of cell protrusions, defined here as type II lobes, were instances in which a protrusion was located at a three-way cell wall junction. These tripartite junctions form during cytokinesis, and in some, but not all, cases, the cell can grow asymmetrically at this location, generating a protrusion with a shape that often is indistinguishable from type I lobes. However, the

growth mechanism that generates a type II lobe may resemble intrusive growth (Jura et al., 2006), in which one cell expands asymmetrically at the interface of two adjacent cells. This form of asymmetric growth likely differs from that which generates lobes that are independent of tripartite junctions. There is certainly a need to distinguish between these different types when one analyzes phenotypes and gene function. Currently, this is a weakness of LobeFinder, because the program operates on the coordinates of individual cells and information on the cell wall patterns of its neighboring cells is lost. At present, if a user wishes to distinguish type I and type II lobes, one can use the graphical output from LobeFinder to identify the subset of lobes that fall on three-way cell wall junctions. In the future, we hope to use a semiautomated cell segmentation program like CellECT (Delibaltov et al., 2016) to simultaneously extract cell coordinates from fields of cells and track the positions of three-way cell wall boundaries.

To quantitatively evaluate the performance of the algorithm for lobe location, we compared the positions of the predicted lobes against the manually determined lobes within a specified tolerance (0.025 radians). If LobeFinder identified the proper location within the tolerance, it was identified as a true positive (TP; Supplemental Fig. S2). If a predicted LobeFinder point was not within 0.025 radians of a manually identified point, it was considered a false positive (FP). Missed lobe points were defined as false negatives (FN). We did not calculate true negatives, since this would be an ambiguous number to determine and it would not inform the evaluation of the method. Related to these quantities, we also calculated the sensitivity [TP/(TP + FN)] and the false discovery rate (FDR) [FP/(TP + FP)]. Both of these measures are used to determine the effectiveness of the algorithm.

A high sensitivity and a low FDR are the primary objectives for the application of LobeFinder as a tool for the reliable and automated measurement of cell shape properties. Nine different combinations of the parameters δ and λ were tested that covered a wide range of parameter values. The highest parameter values yielded decreased sensitivity and increased false positives; however, there was a fairly broad range of parameter combinations that yielded a sensitivity of approximately 0.8 and an FDR of approximately 0.25 (Supplemental Fig. S2). This indicates a relatively low dependence of the algorithm on the specific parameters. The optimized parameter combinations yielded an average sensitivity of 0.95 or higher and an average FDR of less than 0.2 (Supplemental Fig. S2).

Identification of New Lobes in Time-Lapse Images of Pavement Cells

The lobe number, shape, and size properties of pavement cells were analyzed in populations of cells at different intervals of cotyledon development. We applied the LobeFinder program to identify lobes in three time-lapse data sets of pavement cell growth. The first data set represents early growth from 38 h after germination (HAG) to 56 HAG. This slightly overlaps with the second data set from 48 to 120 HAG. The third data set covers 72 to 120 HAG. Data sets 2 and 3 were part of a previous analysis of pavement cell growth (Zhang et al., 2011), and the raw images were reanalyzed here using LobeFinder. Example cells from these three different data sets are shown in Figure 4, A to C. Each showed combinations of symmetrical lateral expansion, with data sets 1 and 2 including more cells that initiated new lobes during the time interval. For example, in the cell that is representative of the 72- to 120-HAG data set, we observed no change in lobe number over the course of time, but it increased in size (Fig. 4C, left to right). In contrast, the cell in the 48- to 120-HAG data set initiated five new lobes (Fig. 4B, left to right), while the cell in the 38- to 55-HAG data set added three new lobes in the time span of 27 h (Fig. 4A, left to right). There is a great deal of variability in pavement cell size and lobe number as a function of cotyledon and leaf development (Elsner et al., 2012; Staff et al., 2012). As a result, in the relatively small windows of time analyzed here, there are examples in which lobe number and cell area are not strictly correlated with developmental time (Table I; Supplemental Table S1). However, differences in lobe initiation rates of individual cells within the time intervals were apparent. Overall, the average number of new lobes per cell was about 2.5 for the 38- to 55-HAG and 48- to 120-HAG populations and 0.5 for the 72- to 20-HAG population (Table I). The percentages of cells in all data sets that grew new lobes were 33% for 72 to 120 HAG, 93% for 48 to 120 HAG, and 80% for 38 to 55 HAG (Table I). These LobeFinder outputs and the average number of lobes per cell at each time point (Table I) indicate that lobing events are prevalent in early stages of growth and that lobing events slow down at some point between 56 and 72 HAG. These results are consistent with the conclusions of a previous study (Zhang et al., 2011).

Additional scalar metric outputs from LobeFinder also correlate with different phases of pavement cell growth; however, they do not directly inform the generation of new lobes. Specifically, for example, the circularity of the individual cells decreases between the two time points (Table II), likely due to the increased expansion of lobes that are initiated primarily in the first 2.5 d after germination. This would also explain the observed decreases in the convexity (ratio of hull perimeter to cell perimeter) and solidity (ratio of hull area to cell area) of pavement cells. Overall, the identification of lobing events and the scalar metrics are consistent with the existence of a permissive developmental window for active lobe formation early in cotyledon development.

Another output from LobeFinder that is useful for cell analyses is a plot of the distance from the refined hull to the cell boundary, which provides a graphical representation of the magnitudes and directions of cell shape change near the cell periphery. This is due to the fact that, as lobes expand, their height and width

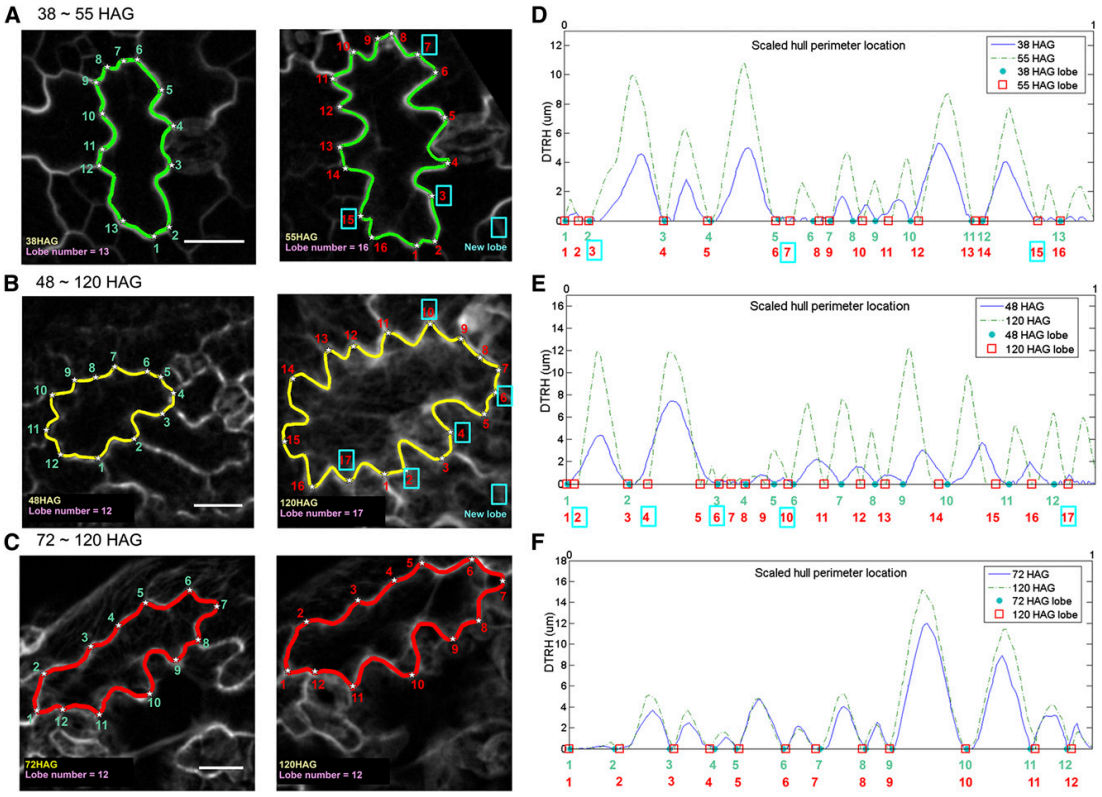

Figure 4. LobeFinder can be used to detect new lobes and quantify growth patterns in time-lapse images. A to C, Examples of raw images of pavement cells with manually segmented cell shapes at three different intervals of cotyledon development. A, Pavement cell at 38 (left) and 55 (right) HAG. B, Pavement cell at 48 (left) and 120 (right) HAG. C, Pavement cell at 72 (left) and 120 (right) HAG. The blue boxes indicate the detection of new lobes and their location in the images and on the DTRH plots. D to F, DTRH plots for pavement cells that were rescaled to their original size. The *x* axes of these plots are the scaled distance along the convex hull perimeter at the two different time points to enable visual comparisons of similar relative positions along the cell boundary at the two time points. The blue line is the DTRH at the initial time point, and the dotted green line is the DTRH at the final time point. The time points in D to F correspond to those of A to C, respectively, and are shown in the legend for each plot. The blue dots and red boxes on the *x* axis identify lobe locations in the initial and final time points, respectively. Bars = 20 μm.

increase, leading to corresponding changes in the DTRH plots. At the distal tips of cell protrusions, the DTRH is zero and corresponds to a lobe point of the cell of interest in the LobeFinder output. The shape of the cell boundary between lobes is captured by the contour of the DTRH, which is at a local maximum at the most concave position between lobes. Therefore, in a time-lapse experiment, the DTRH plots reflect the local growth behaviors of the adjacent protruding cell and the shape change at the interface between the two cells. In Figure 4, D to F, the DTRH was plotted for each cell at the two different time points. The position along the hull is plotted on the *x* axis, and this is scaled to the hull length of the initial time point to enable the DTRH values from

Table I. *Lobe number quantification for cotyledon pavement cells at different developmental stages using LobeFinder*
For 38 to 55 HAG, *n* = 10 cells; for 48 to 120 HAG, *n* = 12 cells; and for 72 to 120 HAG, *n* = 12 cells.

Parameter	38 to 55 HAG		48 to 120 HAG		72 to 120 HAG	
	38 h	55 h	48 h	120 h	72 h	120 h
Averaged lobe number	9.60 ± 2.68	12.10 ± 2.99	8.27 ± 2.89	10.87 ± 2.59	11.17 ± 2.89	11.67 ± 2.46
Percentage with lobe initiation	80		93		33	
Average new lobes per cell	2.50 ± 2.46		2.60 ± 1.68		0.50 ± 2.07	

Table II. *Cell shape descriptors of cells analyzed with LobeFinder*

Feature	38 to 55 HAG		48 to 120 HAG		72 to 120 HAG	
	38 h	55 h	48 h	120 h	72 h	120 h
Circularity	0.60 ± 0.09	0.46 ± 0.11	0.62 ± 0.10	0.49 ± 0.11	0.45 ± 0.13	0.42 ± 0.12
Roundness	0.69 ± 0.06	0.63 ± 0.06	0.70 ± 0.09	0.64 ± 0.09	0.63 ± 0.08	0.61 ± 0.07
Convexity	0.93 ± 0.04	0.85 ± 0.07	0.94 ± 0.03	0.87 ± 0.06	0.84 ± 0.10	0.82 ± 0.10
Solidity	0.86 ± 0.03	0.79 ± 0.05	0.85 ± 0.06	0.80 ± 0.06	0.77 ± 0.06	0.75 ± 0.05

different time points to be compared at similar relative positions along the hull perimeter. During the 72- to 120-HAG interval (Fig. 4F), growth is highly symmetrical and lobe initiation is rare (Zhang et al., 2011). The corresponding DTRH plots were consistent with this result, because the contours of the plots at the two time points were highly symmetrical with well-aligned peaks. It is important to note that the peak widths for the later time points are compressed because the x axis is scaled. However, as shown previously (Zhang et al., 2011), pavement cell growth during this phase is not perfectly symmetrical, and there were subregions of the DTRH plots that were not symmetrical (Fig. 4F), indicating that some local warping of cell shape occurred during growth. The paired DTRH plots for cells that form new lobes (Fig. 4, E and F) reflected a composite growth behavior. In some regions of the cell-cell interface, growth appeared symmetrical, with proportional increases in peak height and width at similar relative positions. The DTRH plots also revealed an obvious contribution of polarized growth to the shape change, because new peaks were detected. In addition, many of the peaks were shifted in position along the hull perimeter, reflecting symmetry breaking during lobe initiation and the accumulation of local warping during the growth interval.

DISCUSSION

LobeFinder is a novel convex hull-based tool to quantify the local boundary characteristics of a closed geometric shape and identify key features such as pavement cell lobes. The ability of LobeFinder to consistently and accurately identify and position lobes within a pavement cell is an important advance, because currently there is no reliable method to quantify the convoluted shape of pavement cells. Manual definition of lobe number (Fu et al., 2005; Xu et al., 2010) or a feature such as the pavement cell neck width (the shortest distance across the cell between two indentations; Lin et al., 2013) is subjective and variable. Variation in human scoring is a major problem: we document here significant variability in lobe number scoring, even among well-trained individuals (Fig. 3, E and G). The lack of standardized phenotyping methods can contribute to differing conclusions regarding whether a particular mutant has a pavement cell phenotype (Xu et al., 2010; Gao et al., 2015). Manual cell scoring is also time consuming. It requires careful inspection of the cell boundary and the manual annotation of each feature in the image file that is scored as a lobe. Skeletonization of segmented, binary images of cells can identify pavement cell protrusions (Staff et al., 2012), and in some instances, it can be used to detect significant differences between mutant and wild-type plants (Le et al., 2006). However, the skeletonize technique is very inaccurate and tends to miss approximately 40% of all lobes (Fig. 3G). LobeFinder has a much greater accuracy compared with the skeletonize method and performs with an accuracy that is only achieved by averaging the votes of several individuals with extensive experience in pavement cell analysis (Fig. 3G).

The availability of an accurate method to directly identify pavement cell lobes is important because scalar shape descriptors such as circularity are sensitive to multiple features of a cell geometry and do not contain information on the local cell features that are most useful for understanding cell growth behavior. For example, differences between cells in their scalar descriptors could reflect differences in lobe number, reduced lobe expansion, or altered diffuse growth in the midregion of the cells. This point is important because it is often assumed that any mutant with a reduced perimeter-to-area ratio has a lobe initiation defect. LobeFinder directly analyzes the local geometry of the cell and identifies lobes. In this regard, it is a powerful phenotyping tool that can be used to compare populations of cells and cell shape over time. However, the LobeFinder program is not perfect, and because of the local shape and spacing thresholds that are used for lobe detection, there are instances, most often along extended domains of low curvature, in which false positives occasionally are reported. Overall, LobeFinder has great potential for the community, and we anticipate that LobeFinder, provided as a user-friendly program in MatLab (Supplemental Fig. S3), will allow others to use this program to analyze mutants and objectively test for direct effects on lobe initiation.

A major advantage of LobeFinder is that it creates a coordinate system to quantify local growth behaviors at the interface of two cells. Alternative approaches to lobe detection, such as quantification of the local curvature of the cell perimeter using variation in the tangent to the cell boundary as a function of cell perimeter, could operate on splined images to identify regions of local curvature that accurately identify lobes. However, this strategy would not generate a coordinate system to analyze growth. Here, we use LobeFinder and plots of the DTRH in time-series data to illustrate a method to quantify local growth behaviors of an irregularly shaped cell (Fig. 4). For example, the DTRH plots could be

analyzed further in time-lapse experiments to generate spatial maps of how the magnitude and direction of growth at the interface of two cells change. These plots clearly indicate the timing, location, and pattern of polarized growth along the interface of interdigitating pavement cells. Importantly, these plots do not reveal the subcellular patterns of growth that explain the shape change. To solve this problem, convex hull-based growth analysis coupled with the use of fiducial marks on the cell wall to track growth patterns (Zhang et al., 2011; Elsner et al., 2012; Staff et al., 2012) could provide improved methods to analyze the subcellular heterogeneity in polarized growth. While this article was being written, a report appeared in which externally applied particles were used to track the growth patterns of the outer wall in fields of developing pavement cells (Armour et al., 2015). The utility of externally applied particles to analyze the growth of the anticlinal wall is uncertain. However, the combined use of DTRH plots, high-density cell wall marking, and time-lapse imaging has the potential to reveal how the polarized growth of individual cells and cell clusters can operate at broader spatial scales to dictate the growth patterns of leaf sectors and even whole organs (Zhang et al., 2011; Kuchen et al., 2012; Remmler and Rolland-Lagan, 2012).

LobeFinder also has immediate applications in terms of more quantitatively dissecting the molecular control of lobe initiation. Hull-based methods and the DTRH plots establish a perimeter coordinate system onto which the temporal and spatial patterns of lobe formation can be graphed (Fig. 4). This is a boon for further analysis, such as the correlation of spatial geometric features with the localization of the cell wall and intracellular signaling and structural factors that are believed to control symmetry breaking. Specifically, LobeFinder can provide the convex hull coordinate system to test for correlations between the local accumulation of proteins such as auxin efflux carriers (Fu et al., 2005; Xu et al., 2010) or microtubules (Panteris et al., 1993; Qiu et al., 2002; Panteris and Galatis, 2005; Ambrose et al., 2007; Kirik et al., 2007; Zhang et al., 2011) and lobe initiation. In this manner, an array of GFP-tagged proteins can be tested to determine those whose localization and activity at the cell cortex specify symmetry-breaking events.

Currently, the greatest limitation for LobeFinder is that it operates on cell coordinates from manually segmented cells. Manual segmentation is a reliable, but time-consuming, process, presenting a major bottleneck for high-throughput phenotyping. As discussed previously, the use of individual, segmented cells also makes it impossible to distinguish between type I and type II lobes, which complicates one's ability to test for alterative genetic control mechanisms and differing contributions of the lobe types to cell expansion. The obvious solution is an automated cell segmentation program that accurately extracts cell boundary coordinates and marks three-way cell wall junctions in the data set. Currently, there is no existing segmentation method to accurately extract pavement cell coordinates from fields of cells and track three-way junctions. However, the development of watershed-based cell segmentation coupled with user-guided validation in a program like CellECT (Delibaltov et al., 2016) has the potential to be integrated with LobeFinder to create a more robust and efficient cell analysis pipeline.

We show here that LobeFinder is an effective new tool for pavement cell phenotyping and growth analysis. We believe that this algorithm has a broader utility for the quantification of many lobed cell types (Panteris and Galatis, 2005) and the analysis of objects with closed and highly irregular geometric shapes at any spatial scale. For example, there is great interest in the quantitative analysis of leaf shape, and the complex boundary shapes of many types of leaves could be analyzed with LobeFinder. In this context, LobeFinder, could complement other leaf shape analysis programs like LeafProcessor (Backhaus et al., 2010). Similar hull-based methods could operate on projected images of shoots and roots to analyze whole-plant architecture over time. We also believe that LobeFinder could have broad applications in other fields, such as human medicine and environmental science. For example, the progression of irregularly shaped tumors could be quantified over time and correlated with other features such as tumor location or drug treatment regimes. The local spatial dynamics of spreading plumes of contamination, floods, and the retraction of glaciers could be similarly analyzed and tested for cross correlations with any variable of interest. Our efforts will focus on the use and integration of LobeFinder within a completely automated image-analysis platform, with the goal of accelerating discovery in the field of leaf morphogenesis.

MATERIALS AND METHODS

Annotation and Use of the LobeFinder Program

To run LobeFinder, start an instance of MatLab on the workstation (PC, MAC, or Linux) and change the working directory to the install location of LobeFinder. The script and all functions that make up LobeFinder are located in one MatLab m-file: LobeFinder_GUI.m. To run LobeFinder, first create a directory to which all regions of interest (ROIs) of cell perimeter coordinates obtained by manual segmentation are saved. Start the LobeFinder GUI by typing LobeFinder_GUI at the MatLab workspace prompt and < Enter > . This will open an instance of the LobeFinder GUI in a separate window (Supplemental Fig. S3). To import files, click on the Open Folder button to select the folder that contains the ROI files. At this point, one can select the checkboxes for the types of data output files to be generated (CSV, Figures, or MatLab file) as well as the resolution of the images from which the ROIs were extracted. Once the folder and options have been selected, click on the Run button to start the ROI processing. The total number of ROI files being processed will be shown in the image number box on the GUI. To view the results from the LobeFinder processing, select the image number from the image number box. This will populate the GUI with the measured parameters as well as an image of the refined hull, the cell boundary, identified lobe points, and DTRH plot. Moving the cursor over the perimeter of the cell will allow its corresponding position on the DTRH plot to be seen. Depending on the output options selected, a new folder in the directory of LobeFinder will be created ([Output]_NameOfInputFolder) with up to three folders (CSV, FIG_cell, and FIG_dtrh). The CSV folder contains one MatLab mat-file Lobe_result.mat, which contains all results and geometric scalar properties for each ROI in the directory, a CellDescriptors.csv file containing all single-value measurements such as area, perimeter, etc. for all ROIs, and

individual DTRH_[nameOfROI] files containing *xy* values for DTRH plots. FIG_cell and FIG_dtrh folders will contain images of cells and DTRH plots as displayed in the LobeFinder GUI. ROILobeFinder is available for download at the Dryad Digital Repository (http://doi.org/10.5061/dryad.cs78t).

Plant Material and Growth Conditions

Arabidopsis (*Arabidopsis thaliana*) seeds were grown on one-half-strength Murashige and Skoog medium with 1% Suc and 0.8% Bacto agar under constant illumination at 22°C. Seeds were treated with a 6-h light pulse, cold treated for 3 d, and then placed in the growth chamber. Germination was checked 36 h after plating, and only seedlings with a barely visible radicles were used for further analysis.

Time-Lapse Imaging of Lobe Initiation

For time-point imaging, cell outlines were detected using a tubulin:GFP marker for data sets 2 and 3 as described previously (Zhang et al., 2011). For data set 1, from 38 to 55 HAG, 10 cells were analyzed. For data set 2, from 48 to 120 HAG, 12 cells were analyzed. For data set 3, from 72 to 120 HAG, 12 cell were analyzed. For data set 1, the PIN7:GFP (Blilou et al., 2005) plasma membrane marker was used. The seedlings were mounted in water using a petroleum jelly gasket to form a chambered microscope slide. After initial imaging, the slides were returned to the growth chamber until the next imaging session. Samples were imaged using a Bio-Rad 2100 laser scanning confocal microscope mounted on a Nikon Eclipse E800 stand. Images were obtained with a 60× 1.2 numerical aperture water objective. Samples were excited with a 488-nm laser, and fluorescence signal was collected using a 490-nm long-pass dichroic and a 500- to 550-nm band-pass emission filter. Selected planes from confocal image stacks were converted to maximum intensity projects and were traced with the polygon selection tool in FIJI 4.0 (Schindelin et al., 2012). The coordinates from the ROIs from the manually segmented cells were used as the input for LobeFinder.

Supplemental Data

The following supplemental materials are available.

Supplemental Figure S1. Examples of raw confocal images of pavement cells and skeletonization results for the 15 cells that were used to validate LobeFinder.

Supplemental Figure S2. Sensitivity and accuracy analysis of LobeFinder performance.

Supplemental Figure S3. Snapshot of the graphical user interface of LobeFinder.

Supplemental Table S1. Morphological properties of pavement cells measured using LobeFinder.

Received June 24, 2015; accepted May 24, 2016; published June 10, 2016.

LITERATURE CITED

Ambrose JC, Shoji T, Kotzer AM, Pighin JA, Wasteneys GO (2007) The *Arabidopsis* CLASP gene encodes a microtubule-associated protein involved in cell expansion and division. Plant Cell **19:** 2763–2775

Andriankaja M, Dhondt S, De Bodt S, Vanhaeren H, Coppens F, De Milde L, Mühlenbock P, Skirycz A, Gonzalez N, Beemster GT, et al (2012) Exit from proliferation during leaf development in Arabidopsis thaliana: a not-so-gradual process. Dev Cell **22:** 64–78

Arganda-Carreras I, Fernández-González R, Muñoz-Barrutia A, Ortiz-De-Solorzano C (2010) 3D reconstruction of histological sections: application to mammary gland tissue. Microsc Res Tech **73:** 1019–1029

Armour WJ, Barton DA, Law AM, Overall RL (2015) Differential growth in periclinal and anticlinal walls during lobe formation in *Arabidopsis* cotyledon pavement cells. Plant Cell **27:** 2484–2500

Asl LK, Dhondt S, Boudolf V, Beemster GTS, Beeckman T, Inzé D, Govaerts W, De Veylder L (2011) Model-based analysis of Arabidopsis leaf epidermal cells reveals distinct division and expansion patterns for pavement and guard cells. Plant Physiol **156:** 2172–2183

Backhaus A, Kuwabara A, Bauch M, Monk N, Sanguinetti G, Fleming A (2010) LEAFPROCESSOR: a new leaf phenotyping tool using contour bending energy and shape cluster analysis. New Phytol **187:** 251–261

Blilou I, Xu J, Wildwater M, Willemsen V, Paponov I, Friml J, Heidstra R, Aida M, Palme K, Scheres B (2005) The PIN auxin efflux facilitator network controls growth and patterning in *Arabidopsis* roots. Nature **433:** 39–44

Delibaltov DL, Gaur U, Kim J, Kourakis M, Newman-Smith E, Smith W, Belteton SA, Szymanski DB, Manjunath BS (2016) CellECT: cell evolution capturing tool. BMC Bioinformatics **17:** 88

Djakovic S, Dyachok J, Burke M, Frank MJ, Smith LG (2006) BRICK1/HSPC300 functions with SCAR and the ARP2/3 complex to regulate epidermal cell shape in *Arabidopsis*. Development **133:** 1091–1100

Elsner J, Michalski M, Kwiatkowska D (2012) Spatiotemporal variation of leaf epidermal cell growth: a quantitative analysis of Arabidopsis thaliana wild-type and triple cyclinD3 mutant plants. Ann Bot (Lond) **109:** 897–910

Fu Y, Gu Y, Zheng Z, Wasteneys G, Yang Z (2005) Arabidopsis interdigitating cell growth requires two antagonistic pathways with opposing action on cell morphogenesis. Cell **120:** 687–700

Fu Y, Li H, Yang Z (2002) The ROP2 GTPase controls the formation of cortical fine F-actin and the early phase of directional cell expansion during *Arabidopsis* organogenesis. Plant Cell **14:** 777–794

Gao Y, Zhang Y, Zhang D, Dai X, Estelle M, Zhao Y (2015) Auxin binding protein 1 (ABP1) is not required for either auxin signaling or Arabidopsis development. Proc Natl Acad Sci USA **112:** 2275–2280

Geitmann A, Ortega JK (2009) Mechanics and modeling of plant cell growth. Trends Plant Sci **14:** 467–478

Graham RL (1972) An efficient algorithm for determining the convex hull of a finite planar set. Inf Process Lett **1:** 132–133

Jura J, Kojs P, Iqbal M, Szymanowska-Pulka J, Wloch W (2006) Apical intrusive growth of cambial fusiform initials along the tangential walls of adjacent fusiform initials: evidence for a new concept. Aust J Bot **54:** 493–504

Kieber JJ, Rothenberg M, Roman G, Feldmann KA, Ecker JR (1993) *CTR1*, a negative regulator of the ethylene response pathway in *Arabidopsis*, encodes a member of the raf family of protein kinases. Cell **72:** 427–441

Kirik V, Herrmann U, Parupalli C, Sedbrook JC, Ehrhardt DW, Hülskamp M (2007) CLASP localizes in two discrete patterns on cortical microtubules and is required for cell morphogenesis and cell division in Arabidopsis. J Cell Sci **120:** 4416–4425

Kuchen EE, Fox S, de Reuille PB, Kennaway R, Bensmihen S, Avondo J, Calder GM, Southam P, Robinson S, Bangham A, et al (2012) Generation of leaf shape through early patterns of growth and tissue polarity. Science **335:** 1092–1096

Le J, El-Assal Sel-D, Basu D, Saad ME, Szymanski DB (2003) Requirements for *Arabidopsis ATARP2* and *ATARP3* during epidermal development. Curr Biol **13:** 1341–1347

Le J, Mallery EL, Zhang C, Brankle S, Szymanski DB (2006) *Arabidopsis* BRICK1/HSPC300 is an essential WAVE-complex subunit that selectively stabilizes the Arp2/3 activator SCAR2. Curr Biol **16:** 895–901

Lin D, Cao L, Zhou Z, Zhu L, Ehrhardt D, Yang Z, Fu Y (2013) Rho GTPase signaling activates microtubule severing to promote microtubule ordering in Arabidopsis. Curr Biol **23:** 290–297

Ma WY, Manjunath BS (2000) EdgeFlow: a technique for boundary detection and image segmentation. IEEE Transactions on Image Processing **9:** 1375–1388

Marcuzzo M, Quelhas P, Campilho A, Mendonça AM (2008) Automatic cell segmentation from confocal microscopy images of the Arabidopsis root. *In* 2008 5th IEEE International Symposium on Biomedical Imaging: From Nano to Macro. IEEE, pp 712–715

Panteris E, Apostolakos P, Galatis B (1993) Microtubules and morphogenesis in ordinary epidermal cells of *Vigna sinensis* leaves. Protoplasma **174:** 91–100

Panteris E, Galatis B (2005) The morphogenesis of lobed plant cells in the mesophyll and epidermis: organization and distinct roles of cortical microtubules and actin filaments. New Phytol **167:** 721–732

Qiu JL, Jilk R, Marks MD, Szymanski DB (2002) The *Arabidopsis SPIKE1* gene is required for normal cell shape control and tissue development. Plant Cell **14:** 101–118

Remmler L, Rolland-Lagan AG (2012) Computational method for quantifying growth patterns at the adaxial leaf surface in three dimensions. Plant Physiol **159:** 27–39

Robert C, Noriega A, Tocino A, Cervantes E (2008) Morphological analysis of seed shape in Arabidopsis thaliana reveals altered polarity in mutants of the ethylene signaling pathway. J Plant Physiol **165:** 911–919

Roeder AH, Chickarmane V, Cunha A, Obara B, Manjunath BS, Meyerowitz EM (2010) Variability in the control of cell division underlies sepal epidermal patterning in *Arabidopsis thaliana*. PLoS Biol **8:** e1000367

Russ JC (2002) The Image Processing Handbook, Ed 4. CRC Press, Boca Raton, FL

Sampathkumar A, Krupinski P, Wightman R, Milani P, Berquand A, Boudaoud A, Hamant O, Jönsson H, Meyerowitz EM (2014) Subcellular and supracellular mechanical stress prescribes cytoskeleton behavior in Arabidopsis cotyledon pavement cells. eLife **3:** e01967

Savaldi-Goldstein S, Peto C, Chory J (2007) The epidermis both drives and restricts plant shoot growth. Nature **446:** 199–202

Schindelin J, Arganda-Carreras I, Frise E, Kaynig V, Longair M, Pietzsch T, Preibisch S, Rueden C, Saalfeld S, Schmid B, et al (2012) Fiji: an open-source platform for biological-image analysis. Nat Methods **9:** 676–682

Staff L, Hurd P, Reale L, Seoighe C, Rockwood A, Gehring C (2012) The hidden geometries of the *Arabidopsis thaliana* epidermis. PLoS ONE **7:** e43546

Szymanski DB (2014) The kinematics and mechanics of leaf expansion: new pieces to the Arabidopsis puzzle. Curr Opin Plant Biol **22:** 141–148

Szymanski DB, Cosgrove DJ (2009) Dynamic coordination of cytoskeletal and cell wall systems during plant cell morphogenesis. Curr Biol **19:** R800–R811

Tsuge T, Tsukaya H, Uchimiya H (1996) Two independent and polarized processes of cell elongation regulate leaf blade expansion in *Arabidopsis thaliana* (L.) Heynh. Development **122:** 1589–1600

Walter A, Silk WK, Schurr U (2009) Environmental effects on spatial and temporal patterns of leaf and root growth. Annu Rev Plant Biol **60:** 279–304

Xu T, Wen M, Nagawa S, Fu Y, Chen JG, Wu MJ, Perrot-Rechenmann C, Friml J, Jones AM, Yang Z (2010) Cell surface- and rho GTPase-based auxin signaling controls cellular interdigitation in Arabidopsis. Cell **143:** 99–110

Yoder N (2011) PeakFinder. http://www.mathworks.com-/matlabcentral/fileexchange/25500

Zhang C, Halsey LE, Szymanski DB (2011) The development and geometry of shape change in Arabidopsis thaliana cotyledon pavement cells. BMC Plant Biol **11:** 27

Zhang C, Mallery EL, Schlueter J, Huang S, Fan Y, Brankle S, Staiger CJ, Szymanski DB (2008) *Arabidopsis SCAR*s function interchangeably to meet actin-related protein 2/3 activation thresholds during morphogenesis. Plant Cell **20:** 995–1011

Zhu XG, Long SP, Ort DR (2010) Improving photosynthetic efficiency for greater yield. Annu Rev Plant Biol **61:** 235–261

3. REASSESSING THE ROLES OF PIN PROTEINS AND ANTICLINAL MICROTUBULES DURING PAVEMENT CELL MORPHOGENESIS

Chapter 3 was published in Plant Physiology in January 2018. The author contributions are as follows. Samuel Belteton and Daniel Szymanski conceived the project. Samuel Belteton conducted the live-cell imaging and develop the image quantification methods and code. Bryon Donohoe used TEM to analyze cell wall thickness. Enrico Scarpella and Megan G. Sawchuck created the PIN live-cell probes and pin mutants. All authors analyzed their own data. Samuel Belteton and Daniel Szymanski wrote the article with contributions from all authors.

Reassessing the Roles of PIN Proteins and Anticlinal Microtubules during Pavement Cell Morphogenesis[1][OPEN]

Samuel A. Belteton,[a] Megan G. Sawchuk,[b] Bryon S. Donohoe,[c] Enrico Scarpella,[b] and Daniel B. Szymanski[a,d,e,2]

[a]Department of Botany and Plant Pathology, Purdue University, West Lafayette, Indiana 47907
[b]Department of Biological Sciences, University of Alberta, Edmonton, Alberta, Canada T6G 2R3
[c]Biosciences Center, National Renewable Energy Laboratory, Golden, Colorado 80401
[d]Department of Biological Sciences, Purdue University, West Lafayette, Indiana 47907
[e]Department of Agronomy, Purdue University, West Lafayette, Indiana 47907

ORCID IDs: 0000-0003-3733-4824 (S.A.B.); 0000-0002-2272-5059 (B.S.D.); 0000-0001-8255-424X (D.B.S.).

The leaf epidermis is a biomechanical shell that influences the size and shape of the organ. Its morphogenesis is a multiscale process in which nanometer-scale cytoskeletal protein complexes, individual cells, and groups of cells pattern growth and define macroscopic leaf traits. Interdigitated growth of neighboring cells is an evolutionarily conserved developmental strategy. Understanding how signaling pathways and cytoskeletal proteins pattern cell walls during this form of tissue morphogenesis is an important research challenge. The cellular and molecular control of a lobed cell morphology is currently thought to involve PIN-FORMED (PIN)-type plasma membrane efflux carriers that generate subcellular auxin gradients. Auxin gradients were proposed to function across cell boundaries to encode stable offset patterns of cortical microtubules and actin filaments between adjacent cells. Many models suggest that long-lived microtubules along the anticlinal cell wall generate local cell wall heterogeneities that restrict local growth and specify the timing and location of lobe formation. Here, we used Arabidopsis (*Arabidopsis thaliana*) reverse genetics and multivariate long-term time-lapse imaging to test current cell shape control models. We found that neither PIN proteins nor long-lived microtubules along the anticlinal wall predict the patterns of lobe formation. In fields of lobing cells, anticlinal microtubules are not correlated with cell shape and are unstable at the time scales of cell expansion. Our analyses indicate that anticlinal microtubules have multiple functions in pavement cells and that lobe initiation is likely controlled by complex interactions among cell geometry, cell wall stress patterns, and transient microtubule networks that span the anticlinal and periclinal walls.

Plant leaves are thin, mechanically durable organs. Their size and shape influence the efficiency of photosynthetic light capture and strongly influence crop yield (Zhu et al., 2010). The growth properties of the leaf epidermis can influence the morphology of the organ (Savaldi-Goldstein et al., 2007); therefore, there is a strong desire to understand how the division and growth of epidermal cells contribute to polarized growth at the level of tissues and organs. In the plant kingdom, an undulating cell shape is commonly generated in the leaf epidermis as polyhedral cells exit the cell division cycle and undergo an extended phase of polarized expansion (Panteris et al., 1993; Panteris and Galatis, 2005; Andriankaja et al., 2012). Interdigitated growth may give the leaf mechanical stability (Onoda et al., 2015; Sahaf and Sharon, 2016) and/or influence polarized growth at spatial scales that extend beyond that of individual cells (Elsner et al., 2012; Remmler and Rolland-Lagan, 2012).

The biomechanics of the lobing process is complex. As in all other plant cell types, turgor pressure provides the driving force for pavement cell morphogenesis, and the physical connectivity of adjacent cells strongly influences the resulting mechanical stresses in the cell wall (Szymanski, 2014). For example, mechanical simulations of the pavement cell wall predict that tension forces are maximal on the unpaired outer periclinal (parallel to the leaf surface) wall and at the interface of the periclinal and anticlinal (perpendicular to the leaf

[1] This work was supported by NSF MCB Grant No. 1121893 and MCB Grant No. 1715544 to D.B.S. and by Discovery Grants of the Natural Sciences and Engineering Research Council of Canada (NSERC) to E.S. B.S.D. was supported by the Center for Direct Catalytic Conversion of Biomass to Biofuels, an Energy Frontier Research Center funded by DOE, Office of Science, BES, under Award DE-SC0000997. M.G.S. was supported, in part, by an NSERC CGS-M Scholarship and an NSERC CGS-D Scholarship.

[2] Address correspondence to dszyman@purdue.edu.

The author responsible for distribution of materials integral to the findings presented in this article in accordance with the policy described in the Instructions for Authors (www.plantphysiol.org) is: Daniel B. Szymanski (dszyman@purdue.edu).

S.A.B. and D.B.S. conceived the project; S.A.B. conducted the live-cell imaging and developed the image quantification methods and code; B.S.D. used TEM to analyze cell wall thickness; E.S. and M.G.S. created the PIN live-cell probes and *pin* mutants; all authors analyzed their own data; S.A.B. and D.B.S. wrote the article with contributions from all authors.

[OPEN] Articles can be viewed without a subscription.
www.plantphysiol.org/cgi/doi/10.1104/pp.17.01554

surface) walls (Sampathkumar et al., 2014). These forces and the geometry of the cell likely contribute to the patterns of growth in lobed cells.

The molecular and biomechanical mechanisms that control lobe initiation are poorly understood. The directions and rates of plant cell expansion are determined by the mechanical properties of the cell wall (Baskin, 2005; Szymanski and Cosgrove, 2009; Cosgrove, 2016), and local modulation of the cellulose microfibril network is a central feature of all pavement cell growth models (Fu et al., 2005; Panteris and Galatis, 2005; Szymanski, 2014). Cellulose microfibrils are highly anisotropic with considerable tensile strength; as a result, bundles of aligned fibers in the cell wall can resist strain most effectively parallel to the fiber network and promote orthogonal strain (Baskin, 2005). Clear thresholds for microfibril alignment can explain the highly anisotropic strain of leaf trichomes (Yanagisawa et al., 2015).

In leaf epidermal pavement cells that already possess a lobed morphology, the correlation between the presence of microtubule bundles and a local convex shape is widespread in the plant kingdom (Panteris and Galatis, 2005). Localization analyses of lobed cells in many plant species detected clusters of anticlinal microtubules and adjacent regions of increased cellulose content at or near convex regions of the cell (Wernicke and Jung, 1992; Panteris et al., 1993; Kotzer and Wasteneys, 2006). Given that microtubules can pattern cellulose microfibril deposition (Paradez et al., 2006) and the correlation of anticlinal microtubules with convex regions of the lobed cells, a common idea is that anticlinal microtubules persist locally earlier in pavement cell morphogenesis and define lobe initiation sites.

Local regions of perpendicularly oriented microfibrils in the anticlinal wall have been proposed to locally resist strain and generate protrusions at adjacent cortical domains (Fu et al., 2005). However, longitudinal alignment of microtubules along the anticlinal wall is a permissive arrangement for transverse elongation of the anticlinal wall in the plane of the epidermis. For example, longitudinally aligned microtubules are observed not only at the convex region of lobes but also along the growing flanks and tips of pavement cell protrusions (Qiu et al., 2002; Zhang et al., 2011). An alternative model proposes that this arrangement of microtubules and microfibrils could enable increased local strain to accommodate the polarized expansion of both cells at the lobing interface (Szymanski, 2014). Stable anticlinal microtubules also are proposed to generate cell wall thickenings that locally resist strain during lobe formation (Panteris and Galatis, 2005). Thickened cell wall pads are present at or near the interface of the anticlinal and periclinal walls in lobed epidermal cells of many species (Panteris et al., 1994); however, to our knowledge, cell wall thickness gradients have not been detected throughout the entire height of the anticlinal wall, and similar cell wall pads or anticlinal thickenings have not been reported in Arabidopsis (*Arabidopsis thaliana*).

Periclinal microtubules frequently splay out from anticlinal microtubule bundles (Panteris et al., 1993, 1994). These splayed microtubules may be part of a transfacial network of microtubules and cellulose fibers that are proposed to generate local anisotropic strain and drive lobe initiation (Panteris and Galatis, 2005; Szymanski, 2014). Because stable anticlinal microtubules figure prominently in all current morphogenesis models, this article focuses primarily on their behaviors as a function of lobe formation.

Arabidopsis has been used as a genetic system to analyze the molecular mechanisms of lobe formation and leaf epidermal morphogenesis. Dozens of mutants that affect the microtubule, actin, and cell wall systems cause pavement cell shape defects (Wasteneys and Galway, 2003; Buschmann and Lloyd, 2008; Fujita et al., 2013; Jacques et al., 2014). In the cotyledon, pavement cell morphogenesis is more synchronous compared with leaves (Tsukaya et al., 1994). Using time-lapse imaging, it was shown that lobe initiation is not a continuous iterative process during cell expansion. Instead, it occurs predominantly during a permissive phase of seedling development up to ~2 d after germination (DAG; Zhang et al., 2011; Armour et al., 2015; Wu et al., 2016). Subsequently, the pavement cells expand for days and increase in area largely independent of lobe initiation (Zhang et al., 2011; Armour et al., 2015; Wu et al., 2016). In highly lobed pavement cells, anticlinal microtubules often are concentrated at the convex region of the cell (Wasteneys et al., 1997; Zhang et al., 2011), and this microtubule arrangement may reflect the ability of the microtubule network to maintain polarized lobe outgrowth and rearrange in response to local cell geometry and the predicted patterns of cell wall stress (Sampathkumar et al., 2014). Transverse microtubules within expanding lobes (concave cell domain) also may pattern microfibrils to reinforce highly polarized lobe outgrowth.

A Rho of Plants (ROP)- (Fu et al., 2005) and auxin- (Xu et al., 2010) centric cell shape control model proposes that polarized subcellular distributions of the PIN-FORMED1 (PIN1) auxin efflux carrier and extracellular AUXIN-BINDING PROTEIN1 (ABP1) generate staggered cortical domains of actin filaments and microtubule bundles that pattern lobe initiation. This model has been challenged by a recently generated null allele of *ABP1* that had no pavement cell phenotype (Gao et al., 2015). In this article, we describe a broader genetic analysis of the proposed auxin signaling network and demonstrate that there is no clear evidence for PIN-based control of lobe initiation.

A recent study analyzed microtubule localization as a function of lobe initiation and concluded that microtubules are stable features that mark lobe initiation sites (Armour et al., 2015). However, this analysis relied on imaging microtubules at a single time point before lobe initiation and lacked a plasma membrane marker to closely monitor the cell boundary. This latter technical issue made it difficult to detect subtle cell wall deformations that reflect the earliest events during lobe

formation. To more carefully analyze the ability of anticlinal microtubules to predict lobe initiation sites, we conducted long-term quantitative analyses of anticlinal microtubules and cell shape using two-color 3D imaging. We found that, in fields of cells that are competent to form lobes, microtubules are neither long-lived structures that predict sites of lobe initiation nor do they define specific sites of localized anticlinal cell wall thickening. Our data indicate that the anticlinal microtubules have multiple functions in lobing pavement cells, and the subset that controls lobe initiation remains unknown. We did detect cortical locations with persistent anticlinal microtubules, and our data suggest that tissue geometry and cell wall stress patterns may play important roles in patterning the microtubule cytoskeleton.

RESULTS

Genetic Analysis of the Plasma Membrane-Localized PINs

PIN1 is a central player in a current model of pavement cell shape control (Xu et al., 2010). To confirm this result, we analyzed the pavement cell phenotype of the *pin1-1* null mutant (Sawchuk et al., 2013). The proposed PIN signaling pathway has reported phenotypes in both cotyledons and true leaves (Fu et al., 2009; Xu et al., 2010). We primarily used the cotyledon system here because the cell types, shape change, and genetic control mechanisms are indistinguishable from those of leaves, and the confounding effect of patchy cell division is minimized. We analyzed *pin1-1* plants for pavement cell shape defects at 2, 5, and 10 DAG (Fig. 1); 10 DAG is the terminal phenotype at which cotyledon expansion ceases (Qiu et al., 2002). We used the recently described LobeFinder algorithm to measure cell shape and count lobes because it eliminates the unavoidable variability in lobe number scoring among individuals (Wu et al., 2016).

At 2 DAG, the number of lobes per cell was slightly higher in *pin1-1* compared with the wild type (Table I). However, this difference was not statistically significant later in development, as the lobe number of *pin1-1* and the wild type were indistinguishable at 5 and 10 DAG. Circularity is a dimensionless shape descriptor based on normalized cell perimeter-to-area ratios, with a circle having a circularity of 1. Circularity values decrease for wild-type cells as they adopt a more convoluted shape, and there were no differences between *pin1-1* and the wild type at any developmental stage (Table I). The pavement cells in the midblade of *pin1-1* and wild-type leaves were very similar in size and shape (Supplemental Fig. S1), indicating that *PIN1* had little or no effect on pavement cell lobing. This unexpected result prompted us to analyze the expression pattern of PIN1 in pavement cells that were undergoing lobe initiation using a validated live cell probe.

PIN1 was reported to have a polarized localization in lobes following microprojectile bombardment and transient overexpression (Xu et al., 2010; Guo et al., 2015). To analyze the expression pattern and localization of PIN1 in cotyledon pavement cells, we imaged *PIN1*::*PIN1*-GFP (Benková et al., 2003) using spinning disk confocal microscopy. In living cells, PIN1 signal was not detected in 2-DAG pavement cells (Fig. 2A), but it was highly expressed in root cortex as described previously (Yan et al., 2013). In young leaves that contain polyhedral pavement cells that were transitioning to polarized growth, PIN1 was expressed along the leaf margin, but not in other fields of pavement cells that were presumably in the process of lobe formation (Supplemental Fig. S2). These genetic and

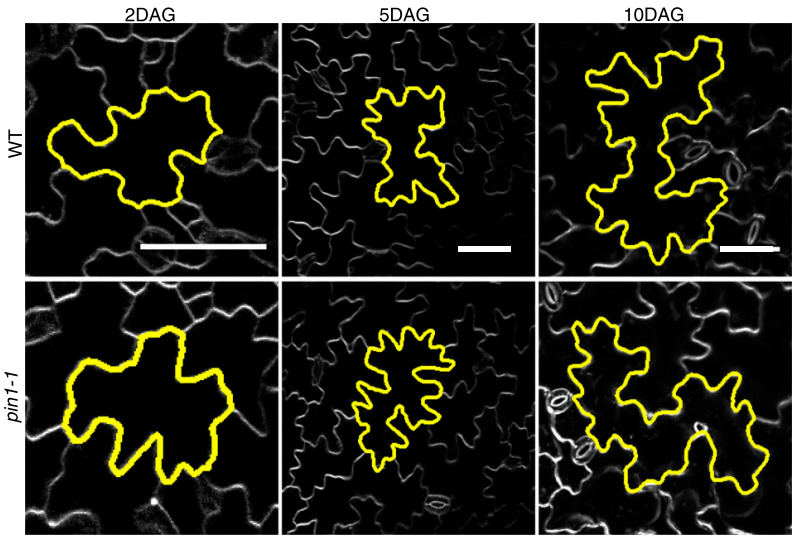

Figure 1. Pavement cells from *pin1-1* null mutants are indistinguishable from wild-type (WT) cells. Representative images of wild-type (top) and *pin1-1* (bottom) cotyledon pavement cells are shown. The time points at which the seedlings were imaged are labeled at top. Bars = 50 μm.

Table I. *Population-level analyses of cell area and shape in pin1-1 and wild-type pavement cells at 2, 5, and 10 DAG*

Values are means ± SD. Asterisks indicate significant statistical differences from the wild type at the same DAG by Wilcoxon-Mann-Whitney test ($P < 0.05$). $n \geq 44$.

Time	Genotype	Area	Circularity	Lobes
		μm^2		
2 DAG	*pin1-1*	1,428 ± 389	0.46 ± 0.09*	11 ± 2*
	Wild type	1,447 ± 481	0.49 ± 0.07	10 ± 2*
5 DAG	*pin1-1*	4,389 ± 2,615*	0.29 ± 0.08	16 ± 3
	Wild type	5,290 ± 2,452*	0.32 ± 0.09	16 ± 3
10 DAG	*pin1-1*	11,956 ± 5,045	0.22 ± 0.07	17 ± 4
	Wild type	10,111 ± 4,641	0.24 ± 0.07	16 ± 4

gene expression results indicated that PIN1 does not affect cell morphogenesis in the cotyledon and leaf epidermis.

We wanted to test the possibility that other plasma membrane-localized PIN proteins were involved in the process of lobe formation. The PIN family consists of eight proteins that can be subdivided into two major groups. The distinguishing characteristic of the group termed long PINs is a large hydrophobic loop (*PIN1*–*PIN4*, *PIN6*, and *PIN7*). The second group lacks this hydrophobic loop and is termed short PINs (*PIN5* and *PIN8*). Short PINs appear to localize to the endoplasmic reticulum (Zazímalová et al., 2010). Of the long PINs, *PIN6* localizes to the endoplasmic reticulum membrane as well (Sawchuk et al., 2013). *PIN2* is implicated in the gravitropism response and is expressed primarily in the root and the hypocotyl (Wiśniewska et al., 2006). PIN4 is expressed very weakly in the seedling epidermis and is a candidate pavement cell shape regulator (Zádníková et al., 2010). The expression patterns of PIN3 (Zádníková et al., 2010), PIN4, and PIN7 in the epidermis were tested directly. We found that all three PINs were expressed and plasma membrane localized in cotyledon pavement cells (Fig. 2B) and the root (Fig. 2C). We tested selected combinations of *pin* mutants for cell shape defects in 10-DAG pavement cells (Supplemental Fig. S3). The number of lobes per cell

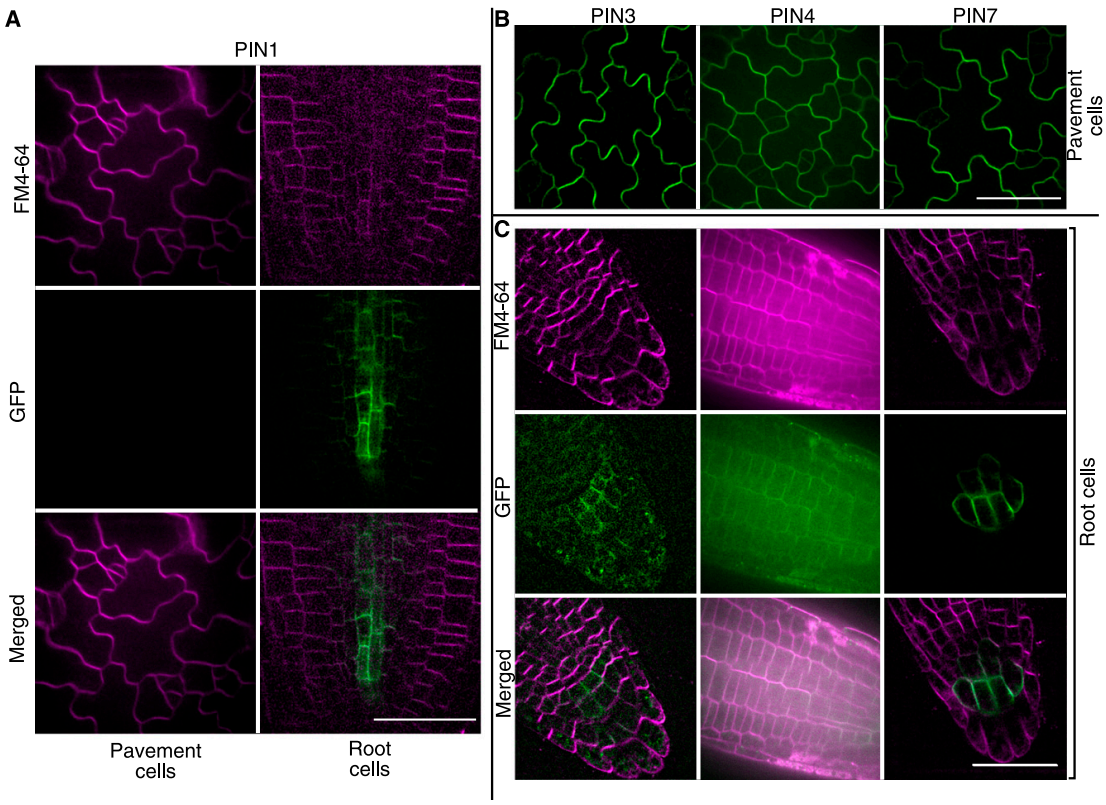

Figure 2. PIN3, PIN4, and PIN7, but not PIN1, are expressed in expanding cotyledon pavement cells. A, PIN1 is expressed in root cells but not in 2-DAG cotyledon pavement cells. B, PIN3, PIN4, and PIN7 are expressed in 2-DAG cotyledon pavement cells. C, Expression of PIN3, PIN4, and PIN7 in the root cortex. FM4-64 was used to visualize the plasma membrane when necessary. Bars = 50 μm.

were not significantly different for the single, double, and triple *pin* mutants (Table II). The *pin* quadruple mutant *pin1;3;4;7* had a slightly reduced lobe number that was statistically significant; however, cell area was reduced nearly by a factor of 2 in this dwarfed quadruple mutant, so the lobe per cell ratio was much higher than that of the wild type. The circularity of the *pin* quadruple pavement cells was higher than in the wild type, indicating that the degree of lobe outgrowth was affected, but not lobe initiation. In addition, the leaf pavement cells of the *pin* quadruple mutant were highly lobed (Supplemental Fig. S1). Our analyses indicated that plasma membrane PINs promote cell expansion, but they are not necessary for lobe formation in cotyledon and leaf pavement cells. We also failed to detect a phenotype for *ric4* (Table II; Supplemental Fig. S3), a proposed effector of ROP signaling in the PIN signaling network (Fu et al., 2005) that was placed in an actin-dependent pathway (Table II). To validate the use of LobeFinder as a useful tool to detect lobe number phenotypes, we conducted a similar analysis on the ARP2/3 complex mutant *distorted2* (*dis2*)*/arpc2*, which has a reported small reduction in lobe number compared with the wild type (El-Din El-Assal et al., 2004; Le et al., 2006). LobeFinder could reveal a significantly reduced lobe number in *dis2* (Table II; Supplemental Fig. S3). The results we present here are consistent with the negative results on ABP1 (Gao et al., 2015) and indicate that auxin efflux carriers do not control lobe initiation.

Table II. *Cell area and shape quantification of pin1, pin3, pin4, and pin7 mutant combinations and ric4-2*

Values are means ± SD. Asterisks indicate significant statistical differences between the null mutant line and the wild type by Wilcoxon-Mann-Whitney test ($P < 0.05$). $n \geq 44$; $n = 16$ for *ric4-2*.

Genotype	Area	Circularity	Lobes
	μm^2		
Wild type	10,111 ± 4,641	0.24 ± 0.07	16 ± 4
pin3	6,839 ± 3,177*	0.26 ± 0.08	16 ± 4
pin3;7	8,671 ± 5,543	0.28 ± 0.10	15 ± 4
pin3;4;7	7,834 ± 4,109*	0.22 ± 0.07	17 ± 4
pin1;3;4;7	4,797 ± 1,718*	0.33 ± 0.08*	15 ± 3*
ric4-2	5,169 ± 1,441*	0.26 ± 0.05	15 ± 2
dis2	9,098 ± 3,143	0.43 ± 0.12*	11 ± 4*

Development of an Image-Analysis Pipeline to Test for Correlations between Anticlinal Microtubule Behaviors and Lobe Initiation

We shifted our analysis to microtubule localization along the anticlinal wall as a function of lobe formation. Existing genetic and pharmacological data indicate that microtubules are involved in lobe formation (Burk et al., 2001; Whittington et al., 2001; Qiu et al., 2002; El-Din El-Assal et al., 2004; Ambrose et al., 2007; Armour et al., 2015); however, the details of how microtubules pattern the cell are under debate (Panteris and Galatis, 2005; Xu et al., 2010; Szymanski, 2014). A growth restriction model for lobe initiation includes a component in which anticlinal microtubule bundles persist for extended periods of time prior to a symmetry-breaking event generating local cell wall thickening, and this local thickening resists strain and leads to adjacent cell outgrowth and lobe initiation (Panteris and Galatis, 2005). In Arabidopsis, an initial growth restriction model was driven largely by the detection of anticlinal microtubule bundles at the convex regions of lobed cell types (Fu et al., 2002). To our knowledge, the article of Armour et al. (2015) is the only one to attempt to image microtubules in the same cell prior to and after lobe formation. They concluded that stable anticlinal microtubules predict lobe initiation sites. However, as mentioned above, this study had limited sampling and statistical analyses of microtubules prior to lobe formation. In addition, the cell boundary was inferred based on the cytosolic signal of the microtubule marker, raising doubts about the accuracy with which lobe initiation was detected. In our time-lapse imaging studies, we immediately noticed that anticlinal microtubules were quite transient. Therefore, we initiated a new approach in which long-term time-lapse imaging of anticlinal microtubules and the plasma membrane-localized protein was quantitatively analyzed to test for correlations between microtubule localization in the anticlinal cortex and cell shape change.

The first step was to develop methods to enable two-channel 3D imaging over the time scales of 6 to 16 h to capture lobe initiation events. The 1.5-DAG seedlings expressing both PIP2:mCherry (Nelson et al., 2007) and GFP:TUB6 (Abe et al., 2004; Abe and Hashimoto, 2005) were mounted in a chambered slide and imaged hourly, which allowed us to capture the ~300-nm cell boundary deformations without bleaching the microtubules (Fig. 3; Supplemental Movies S1 and S2). Our time-lapse imaging protocol did not adversely affect cell expansion, because the areal strain rates of individual pavement cells ranged from 5.2% to 9.6% per hour. These values were comparable to previously reported rates for pavement cells at the early growth stages (Zhang et al., 2011; Elsner et al., 2012; Armour et al., 2015). Segments are defined here as the shared cell wall between two three-way cell wall junctions, and their shape was traced manually at the junction of outer periclinal walls and the anticlinal wall.

The next challenge was to create a method to quantify the timing and location of a lobe initiation event within a cell segment. The LobeFinder algorithm serves this purpose (Wu et al., 2016); however, it operates on closed geometric shapes. Using the findpeaks algorithm in Matlab on these segments, we found that lobes began as very small but persistent local deflections in the cell boundary that became progressively larger (Supplemental Fig. S4). Three example segments at the beginning and end of the time lapse are shown within the cell field (Fig. 4, A and B), and the corresponding segmented images of the cell-cell boundary are displayed in Figure 4C. Lobe initiation events were defined as local prominence peaks of at least 286 nm or

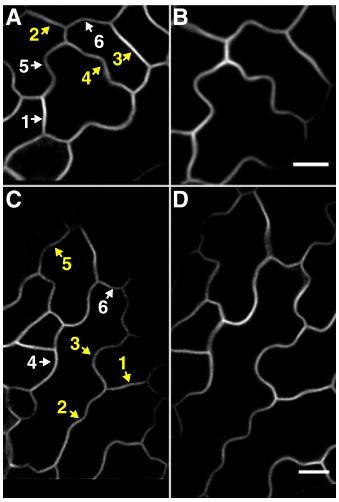

Figure 3. Pavement cell shape change at high temporal and spatial resolution. A and B, Example image field at time point 1 (A) and time point 11 (B) ~9 h later. For full time lapse, see Supplemental Movie S1. C and D, Example image field at time point 1 (C) and time point 11 (D) ~10 h later. For full time lapse, see Supplemental Movie S2. Yellow labels are defined as segments that produce a new lobe(s). White labels are defined as lobed segments that grow but do not have a symmetry-breaking event. Bars = 10 μm.

one pixel that persisted in subsequent images. Using such a small deviation to call an event was valid, because spurious lobes were not identified and all the features detected using this method expanded into easily recognizable lobes at later time points (Fig. 4C, segments II and III). With this algorithm, 86% ($n = 29$) of the lobes were detected continuously after their first appearance. For the other identified lobes, severe local warping within an adjacent region of the segment distorted the cell boundary in a way that the new lobe was still present but fell below our detection threshold momentarily (Supplemental Fig. S5; Supplemental Movie S3). This severe localized warping must include uneven lateral expansion rates along the anticlinal wall. This growth behavior invalidates a major assumption of uniform anticlinal wall expansion that was used to create a strain model to explain lobe initiation (Armour et al., 2015).

Based on this lobe detection method, we scored segments as either those that formed new lobes (lobing) or as those that were already lobed and failed to initiate any additional features (lobed; Fig. 3, A and C). In our time-lapse images, we observed segments in which an existing lobe(s) increased in height and width (Fig. 4C, segment I), relatively straight segments that produced one or more new lobes (Fig. 4C, segment II), and already lobed segments that produced additional lobes (Fig. 4C, segment III). In agreement with previous reports (Zhang et al., 2011; Elsner et al., 2012; Armour et al., 2015), we found that different segments of the same cells undergo very different types of shape change behaviors (Supplemental Movie S1, segments 3, 4, and 6). The geometric features of a cell segment that influence the probability that a new lobe will form are not known. There is evidence for a minimal lobe-spacing rule (Staff et al., 2012) and a weak correlation between the initial segment length and the probability of lobe formation (Wu et al., 2016). As expected, we found that lobes could form on segments with varying initial geometries; however, new lobes did not form within recently formed lobes. Instead, initiation tended to occur between an existing lobe and a three-way cell wall junction. This does not necessarily reflect direct inhibition within existing lobes. For example, the cytoskeletal polarizations, cell wall modifications, and geometric transformations that occur as the lobe expands may make the structure insensitive to the forces and/or signaling activities that promote lobe initiation.

In order to graph segment shape from the same cell over time, their Euclidian distances were normalized from 0 to 1 and the cell boundary features, termed lobe height, were plotted as a function of vertical distance from the cell edge to the line that connected the two three-way junctions (Fig. 4D). The absolute value of lobe height was plotted as a function of position along the segment, so that convex features of both cells at the segment interface could be captured and eventually compared with microtubule distributions (Fig. 4E). We restricted our cell shape-microtubule cross-correlation analyses to protrusions that crossed the baseline and allowed us to detect the convex regions of both cells. The full time course of shape change of segment III includes the expansion of existing lobes and the appearance of new features over time (Fig. 4F).

Quantification of Anticlinal Microtubule Positions over Time

Because anticlinal microtubules are a central component to all existing models of lobe initiation (Fu et al., 2005; Panteris and Galatis, 2005; Szymanski, 2014), including the auxin-based patterning model (Xu et al., 2010), we focused primarily on the localization and persistence of microtubules in the anticlinal cell wall. Current models predict that anticlinal microtubules are expected to accumulate at defined locations prior to lobe formation and persist at the apex of convex surfaces along the cell segment interface. Therefore, we set out to test for long-lived anticlinal microtubules at cortical locations that would give rise to future lobes. We developed methods to quantify the locations and persistence of anticlinal microtubules over extended periods of time for which high-resolution data also were available for cell shape. We were able to obtain high-quality images of anticlinal microtubules along the anticlinal wall using the validated GFP:TUB6 (Abe et al., 2004; Abe and Hashimoto, 2005) live cell microtubule marker (Fig. 5, A–C). Quantification of microtubule signals from a face-down view is possible

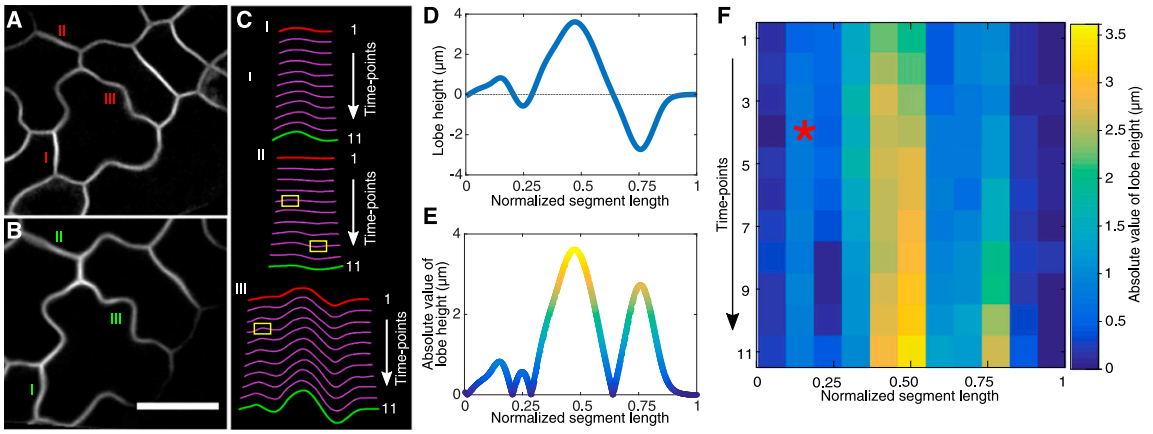

Figure 4. Development of a method to quantify the timing and location of lobe initiation in pavement cell segments that span three-way cell junctions. A and B, Live-cell images of the cell boundaries at time points 1 and 11, respectively. The total elapsed time between these two images is 9.8 h. Bar = 20 μm. C, Segmented cell boundaries illustrating different types of wall reshaping that occur in developing cells. Yellow boxes label the time points and locations of new lobe formation. Red and green segments correspond to the segments shown in A and B, respectively. D, A plot of lobe height defined as the orthogonal distance from the cell boundary to a reference line that connects the two three-way junctions. E, Absolute value of the lobe height in D color coded with a heat map to reflect differing lobe height along the segment length. F, Heat map of lobe height of segment III as a function of normalized segment length (*x* axis) over time (*y* axis). The red star shows new lobe formation.

(Armour et al., 2015); however, from this perspective, weak microtubule signals are missed and information about their orientation is lost. Therefore, we resliced the image stack through the *x*-*y* planes in the region of interest and quantified signals along the *x*-*z* plane, using face-on views of the anticlinal microtubules (Fig. 5, B and C). The microtubule signals along the anticlinal walls were summed as a function of position along the segment perimeter (Fig. 5C) at each time point, and their signal intensity was normalized from 0 to 1 (Fig. 5D). An example time-lapse movie of anticlinal microtubules in Figure 5 is provided as Supplemental Movie S4. Summing microtubule signals along the length of the anticlinal wall perimeter did not cause excessive peak broadening because they were oriented orthogonally to the leaf surface (Supplemental Fig. S6). This allowed us to plot microtubule signals in the cortex of the anticlinal surface as a function of location and time (Fig. 5E). At each time point, the heat map reflects the relative height, shape, and position of the microtubule peaks.

Anticlinal Microtubules Are Not Stable Structures That Predict the Sites of Lobe Initiation

It was immediately apparent that anticlinal microtubules were not strictly linked with the patterns of cell shape change. Microtubules were broadly distributed along the segment length at a given time point (Fig. 5E). The anticlinal microtubules were not stable features in the cortex, as the same peak was rarely if ever present in the subsequent image (Fig. 5E; Supplemental Movie S4). This broad localization and temporal instability of anticlinal microtubules were consistent among a population of lobing and lobed segments (Supplemental Figs. S7 and S8, respectively). Example images of the anticlinal microtubules are shown for each segment. These results strongly suggested that anticlinal microtubules or microtubule bundles are not stable features that predict lobe initiation and that they are not restricted to most convex regions of the cell cortex. The observed broad distribution of microtubules along the anticlinal wall suggests that microtubules are polymerized and depolymerized along extended convex regions of the cell and also is consistent with previous reports that showed that anticlinal microtubules also reside within the concave region of protruding lobes (Qiu et al., 2002; Zhang et al., 2011).

To more quantitatively analyze microtubule signals as a function of cell shape, we tested for cross correlations between cell shape (Fig. 4F) and microtubule signals (Fig. 5E) that were plotted on a common coordinate system. As mentioned above, we conducted this analysis without knowing in which cell the microtubule signals originated. This uncertainty stems from the fact that the thickness of the anticlinal cell wall is below the resolution of the light microscope, and even with the plasma membrane markers, we cannot clearly assign a microtubule to a particular cell. This technical issue exists for any study that analyzes anticlinal microtubules using live cell imaging. Bombardment of a microtubule marker into individual cotyledon pavement cells is possible, but by the time expression levels

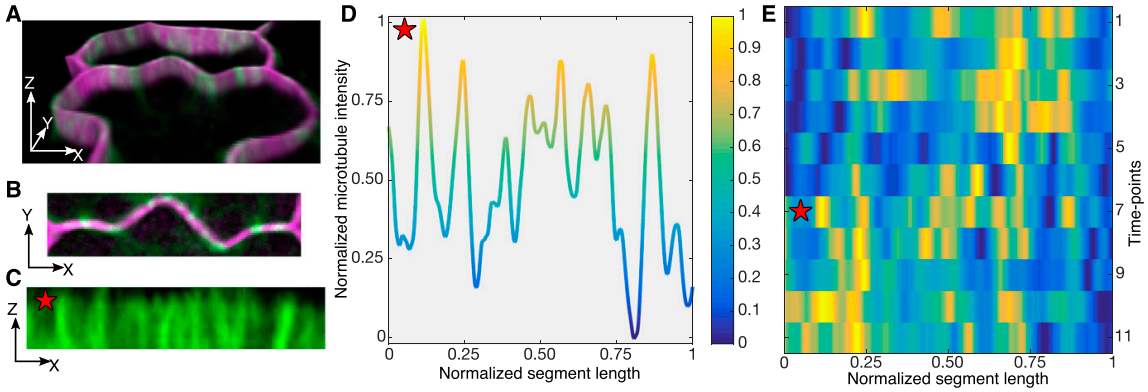

Figure 5. Quantification of microtubule signals and their positions along the segment. A, Live-cell image of a lobing segment: plasma membrane marker in magenta and microtubule marker in green. Cell volume is tilted to highlight the anticlinal wall. B, Projected face-on view of microtubules along the segment. C, The segment is digitally straightened and resliced to provide a face-on view of the microtubules along the anticlinal wall. D, The signal from C is summed as a function of segment location and normalized from 0 to 1. E, Heat map of the normalized microtubule signals as a function of normalized segment length (*x* axis) over time (*y* axis). The red star labels the time point and location of microtubule data that are displayed in C and D.

are detectable, the cells rarely initiate new lobes (Zhang et al., 2011). Another way to assign anticlinal microtubules to a particular cell is to trace the anticlinal microtubules from the anticlinal to the periclinal cell face of the occupied cell. However, our imaging setup was optimized to collect data as deeply as possible without saturating the signals from the anticlinal microtubules. We could not reliably trace microtubules back to an origin at the anticlinal cell face. This is not completely due to artifacts of poor image quality, as close inspection of the image stacks made it clear that many strong microtubule signals along the anticlinal cell face (Fig. 5C; Supplemental Movie S4) clearly terminated at the interface with the periclinal wall. It has been shown previously that only subsets of anticlinal microtubules in later stage cotyledon pavement cells are associated with a periclinal array (Zhang et al., 2011).

Nonetheless, the technical limitation of not knowing the cell of origin for the microtubule does not preclude a statistical test of the growth control model in which anticlinal microtubules are stable cortical landmarks that predict and mark lobe initiation sites (Fu et al., 2005; Panteris and Galatis, 2005; Armour et al., 2015). In this scenario, anticlinal microtubules should always localize to cortical regions that become convex regions of the cell and persist at the extreme convex regions of the cell after lobe formation. The extreme convex regions of the cell were accurately quantified in our lobe height heat maps (Fig. 4E) and allowed us to test for this expected correlation. We conducted Pearson cross-correlation analyses of microtubule signals and cell shape in seven lobing (Supplemental Fig. S7) and five lobed (Supplemental Fig. S8) segments. As expected, the overall Pearson correlation coefficient (PCC) values were very low as a function of time or space. The PCC values fluctuated due to microtubule peak instability over time, but overall, the correlations were low for both classes of cell segments.

A similar analysis was conducted on 5-DAG pavement cells. These cells are highly lobed and their shape change is symmetrical, as the cells increase in area but maintain their overall shape (Zhang et al., 2011). Subsets of convex regions of pavement cells at this stage have periclinal microtubules that splay from anticlinal microtubule bundles (Zhang et al., 2011; Sampathkumar et al., 2014). In cells at this stage, cell shape was quite stable over the time course (Supplemental Fig. S9, A–D). In each highly lobed segment, the anticlinal microtubules were broadly distributed along the cortical surface. In three of four segments, the signals were unstable over time. In one case, the microtubules were more stable but their locations were inversely correlated, with a convex cell shape residing at the distal flanks of a lobe (Supplemental Fig. S9C). Clearly, the geometry of the cell segment alone is not sufficient to predict anticlinal microtubule distributions in pavement cells at several developmental stages.

Although it was clear that there was no global correlation between cell segment shape and anticlinal microtubules, we wanted to test for an enrichment of microtubules at lobe apices compared with flanking regions in recently formed lobes. Therefore, we analyzed anticlinal microtubule distributions in a more directed manner as a function of the local lobe geometry. To do this, individual lobes were subdivided into apex and flanking regions of similar areas based on the full width at half-maximal lobe height (Fig. 6A). The flanking region was defined so that it was clearly separated from the convex regions of the adjacent cell. Microtubule occupancy was calculated simply as the percentage of time points at which a microtubule peak

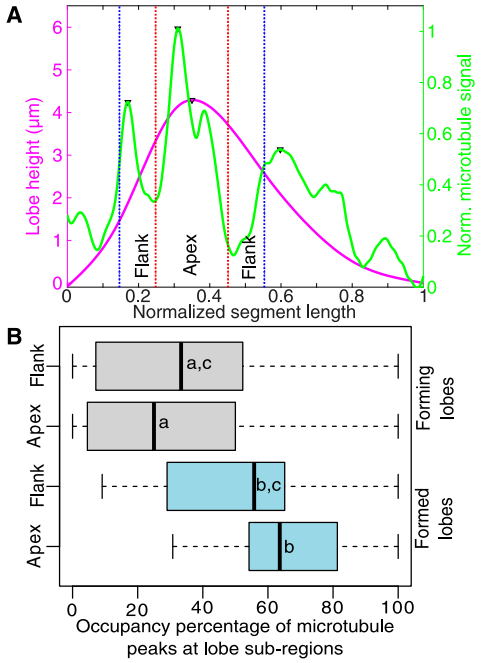

Figure 6. The microtubule peak occupancy at the lobe apex is not significantly higher than that of the adjacent flank regions. A, Example of lobe subdivision based on the lobe width (W) at half-maximal lobe height. The apex is 1/2 W centered at the lobe apex. The flank region total width is 1/2 W surrounding the apex region. B, Population-level analysis of microtubule signal peak occupancy for recently formed lobes (forming) and lobes present at the start of the time series (formed). Letters represent statistically equivalent groups.

was detected within either the apex or the flanking region. This analysis indicated that, for both lobing and lobed segments, the apex and the flank had similar microtubule peak occupancies (Fig. 6B). Our data suggest that anticlinal microtubules are not restricted to subregions within lobes. However, it is likely that there is some bias for microtubule localization within convex regions along the cell-cell interface, and in some cell segments, the microtubule signals may arise predominantly from the convex region of cells. As mentioned above, we cannot rule this out because we cannot define the cell of origin for most of the microtubules. However, our analyses indicate that, if this is occurring, it is occurring very broadly across the convex surface and the microtubules are unstable at the time scale of hours.

Although the anticlinal microtubules were not stable features of developing pavement cells, we wanted to evaluate if there were cortical domains along the anticlinal wall in which microtubules were more likely to reside. We plotted the microtubule signals as a type of persistence plot, summing the values of the microtubule signals along segment length over time (Fig. 7, A and C). Interestingly, there were peaks of accumulated signal for all lobing (Supplemental Fig. S10) and lobed (Supplemental Fig. S11) segments, suggesting that subregions of the cortex were more likely to polymerize and/or stabilize microtubules. In most cases, there were more microtubule persistence peaks than there were lobes, and their locations did not globally correlate with a particular geometric feature of the cell. However, there were examples in both lobing (Supplemental Fig. S10, B–E) and lobed segments (Supplemental Fig. S11, A–D), in which a subset of microtubule peaks were located near lobe apices. We next tested for microtubule persistence in cortical regions that would develop into lobes at a future time point. To do this, we identified the cortical domain that would generate a lobe, projected that cortical domain onto an equivalent region of the same segment at previous time points, and measured the accumulated microtubule signal in the cell segment up to the point of lobe initiation (Supplemental Fig. S12). Most of the lobing segments contained a subset of microtubule peaks at or near cortical regions that would subsequently become part of a lobe (Supplemental Fig. S12, A, B, D, F, and G) and other instances in which there was no obvious relationship between microtubule signals and lobe formation (Supplemental Fig. S12, C, E, and H). This does not rule out a role for persistent anticlinal microtubules during lobe formation: it simply shows that they are not restricted solely to convex or future convex regions of the cell. It is also likely that microtubules that influence lobe initiation were likely missed in hourly image acquisitions.

Although our time-lapse imaging was not optimized for individual periclinal microtubules, we tested for an enrichment of cortical microtubules along the periclinal wall prior to lobe formation. We were able to analyze the density of periclinal microtubules in two adjacent cells prior to lobe formation. It was reported previously that periclinal microtubules were enriched in the cell that would adopt a convex shape prior to lobe formation (Armour et al., 2015). We used our time-lapse image stacks to quantify the cortical occupancy of microtubules at opposing periclinal surfaces as a function of lobe initiation (Fig. 8, A–D). To do this, we focused on cell segments for which we had images of periclinal microtubules for at least seven time points prior to lobe initiation. The mean cortical occupancies (Higaki et al., 2010) of periclinal microtubules over time were calculated within opposing regions of interest (ROIs) in the two adjacent cells at the lobing interface. The ROIs were termed V, to denote the microtubule signals in the cell that would adopt a convex shape, and C, to denote the microtubule signals in the adjacent cell that would adopt a concave shape (Fig. 8D). In five of six lobing segments, there was no significant difference in the cortical occupancy of microtubules between the two cells, and in one instance, microtubules were more dense in the future concave-shaped cell (Fig. 8E). This latter observation is the opposite of what would be predicted from current models, and collectively, the

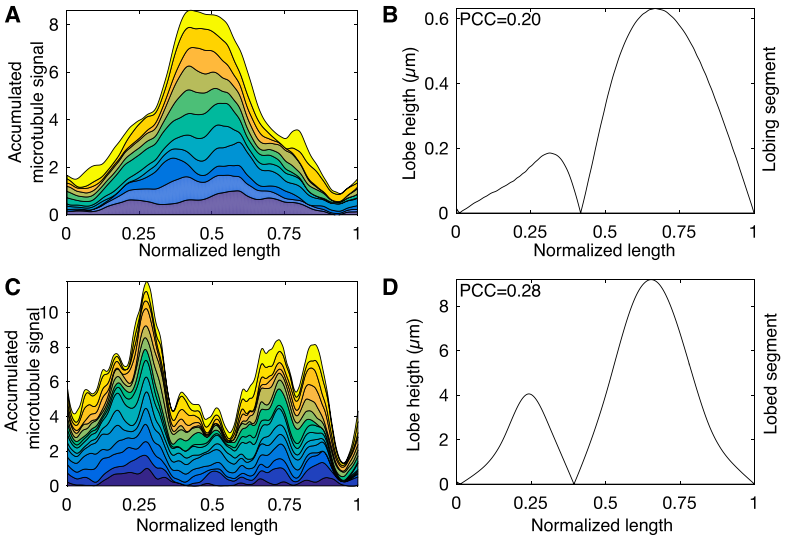

Figure 7. Persistence plots of microtubule signals show unequal accumulation of microtubule signals along a segment. A, Microtubule persistence plot of a segment that forms two new lobes. B, Absolute value of lobe height along the segment analyzed in A. C, Microtubule persistence plot for a lobed segment. D, Absolute value of lobe height along the segment analyzed in C. PCC values in B and C correspond to the correlation analysis between the microtubule persistence signal and the final segment shape.

above data indicate that simple differences in periclinal microtubule density in opposing cells are not sufficient to explain the location and timing of lobe initiation. However, it is likely that differences in microtubule alignment in opposing cells and the polymerization of microtubules that span the anticlinal and periclinal cell faces are important parameters that control lobe initiation.

Anticlinal Microtubule Signals Are Depleted Near Three-Way Cell Wall Junctions

The above analyses did not reveal a particular microtubule feature that could easily explain the patterns of lobe initiation. However, we did notice examples in which anticlinal microtubule signals and cell shape appeared to be correlated in early-stage pavement cells. These tended to be cases in which the initial segment shape was simple and a single broad lobe was present (Supplemental Fig. S11, A and C). This correlation appeared to be driven by the local depletion of anticlinal microtubules adjacent to three-way cell wall junctions. Previously, microtubules were reported to be depleted at three-way junctions at a single time point in lobed pavement cells (Higaki et al., 2016). Our time-lapse data showed that microtubule signals tended to be lower near three-way junctions in cell segments of varying geometries over time (Supplemental Figs. S10 and S11). To test for a robust pattern of localized microtubule depletion, the microtubule signals adjacent to the three-way junctions were compared with an equivalent proportion of the cell cortex in the center of the segment (Fig. 9, A and B). For both lobing and lobed segments, microtubule signals were reduced significantly near three-way junctions compared with the central region (Fig. 9C). The pattern correlates with the reduced magnitude of cell wall stress near three-way junctions that has been predicted by finite element computational models of pavement cell clusters (Sampathkumar et al., 2014).

Anticlinal Microtubule Bundles Are Not Correlated with Regions of Increased Cell Wall Thickness

Our time-lapse data indicated that anticlinal microtubules did not selectively persist at the lobe initiation sites and, therefore, were unlikely to define stable locations to direct the synthesis of a thick cellulose-rich cell wall. We wanted to conduct an independent test of the hypothesis that anticlinal microtubule bundles, defined as two or more microtubules in very close proximity, generate local regions of cell wall thickening in lobing pavement cells, using high-pressure freeze fixation and transmission electron microscopy (TEM) of paradermal sections of early-stage cotyledon pavement cells at 1.5 to 2 DAG. Thin sections were then analyzed for cell wall thickness in the regions that overlay an anticlinal microtubule bundle. Properly oriented paradermal sections were identified based on the appearance of the cell at low magnification and the gap in electron density in the plasma membrane lipid bilayer at high magnification. The railroad track-like appearance of the bilayer is only apparent in sections that are exactly parallel to lipid head groups and fatty acid chains. Microtubules in anticlinal microtubule bundles were clearly detected in cross sections and segmented from the images based on their appearance as hollow circles with a diameter of 20 to 22 nm adjacent

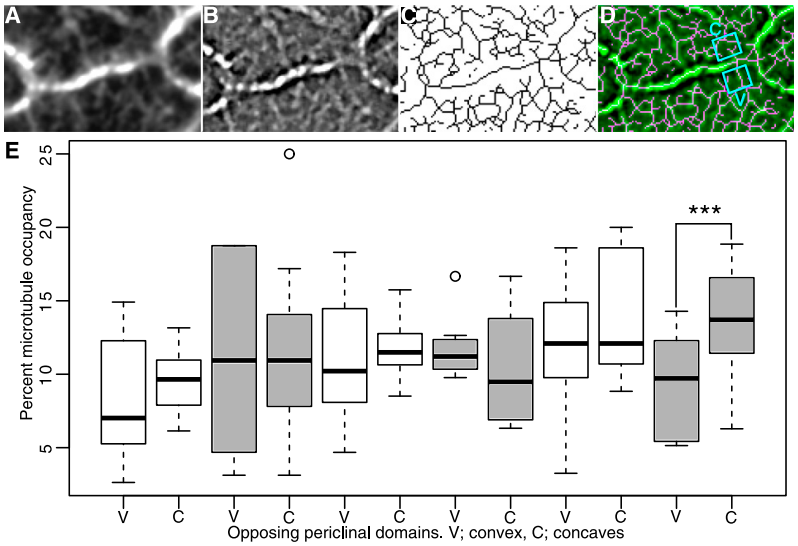

Figure 8. The cortical density of periclinal microtubules does not differ in opposing cells prior to lobe formation. A, Image of periclinal microtubules at the interface of a segment that will form a lobe. B, Processed microtubule image using the cortical occupancy method of Higaki et al. (2010). C, Skeletonized version of the processed image showing segmented microtubules. D, Overlay of the GFP:TUB6 image from B and the microtubule skeleton in C. The ROIs of the future convex (V) and future concave (C) cells are shown at the lobing interface. E, Box plots of the mean cortical occupancy of microtubules in paired convex (V) and concave (C) cells at the lobing interface. ***, Significant difference between the paired cell regions by Student's *t* test ($P < 0.05$).

to the plasma membrane (Fig. 10A). The cell wall also could be segmented from the images, and its thickness was measured as a function of the proximity to anticlinal microtubule bundles. The analysis was conducted on relatively long and straight sections of cell wall from six independent cells that were in a stage of permissive lobe initiation. Among the 36 regions of anticlinal wall that we detected and imaged by TEM, the cell wall thickness varied from approximately 80 to 200 nm. However, the heterogeneity could not be explained by the presence or absence of microtubules. For example, Figure 10C displays box plots of the cell wall thickness values at cell wall domains that overlay anticlinal microtubule bundles and a box plot of wall thickness at an adjacent segment of equal length free of anticlinal microtubule bundles. Among the 18 cell wall regions from six different cells, there was no clear correlation between the presence of anticlinal microtubule bundles and cell wall thickness. In general, microtubules were closely associated with the plasma

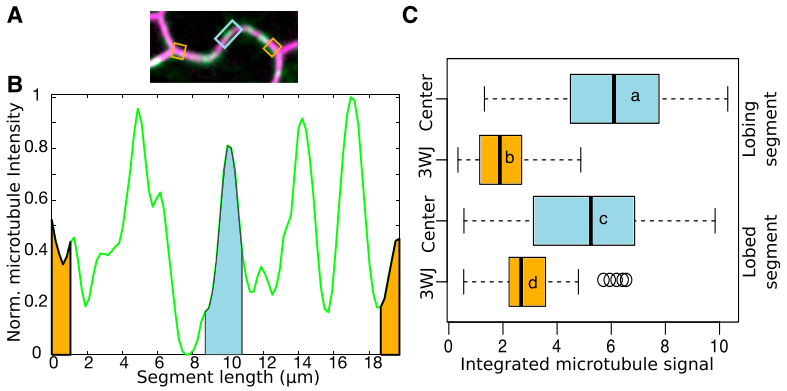

Figure 9. Microtubule signals are significantly lower near three-way junctions compared with a central region of the segment. A, Live-cell image of a segment with microtubule marker in green and plasma membrane marker in magenta. B, Microtubule signal intensity plot of the segment in A. Orange is the area under the microtubule signal curve 1 μm from the three-way junctions. Light blue is the area under the microtubule signal curve 2 μm from the cortex centered at the segment midpoint. C, Box plot of the microtubule signal intensity from three-way junctions and center of segments for both lobing and lobed segments. Letters represent statistically equivalent groups.

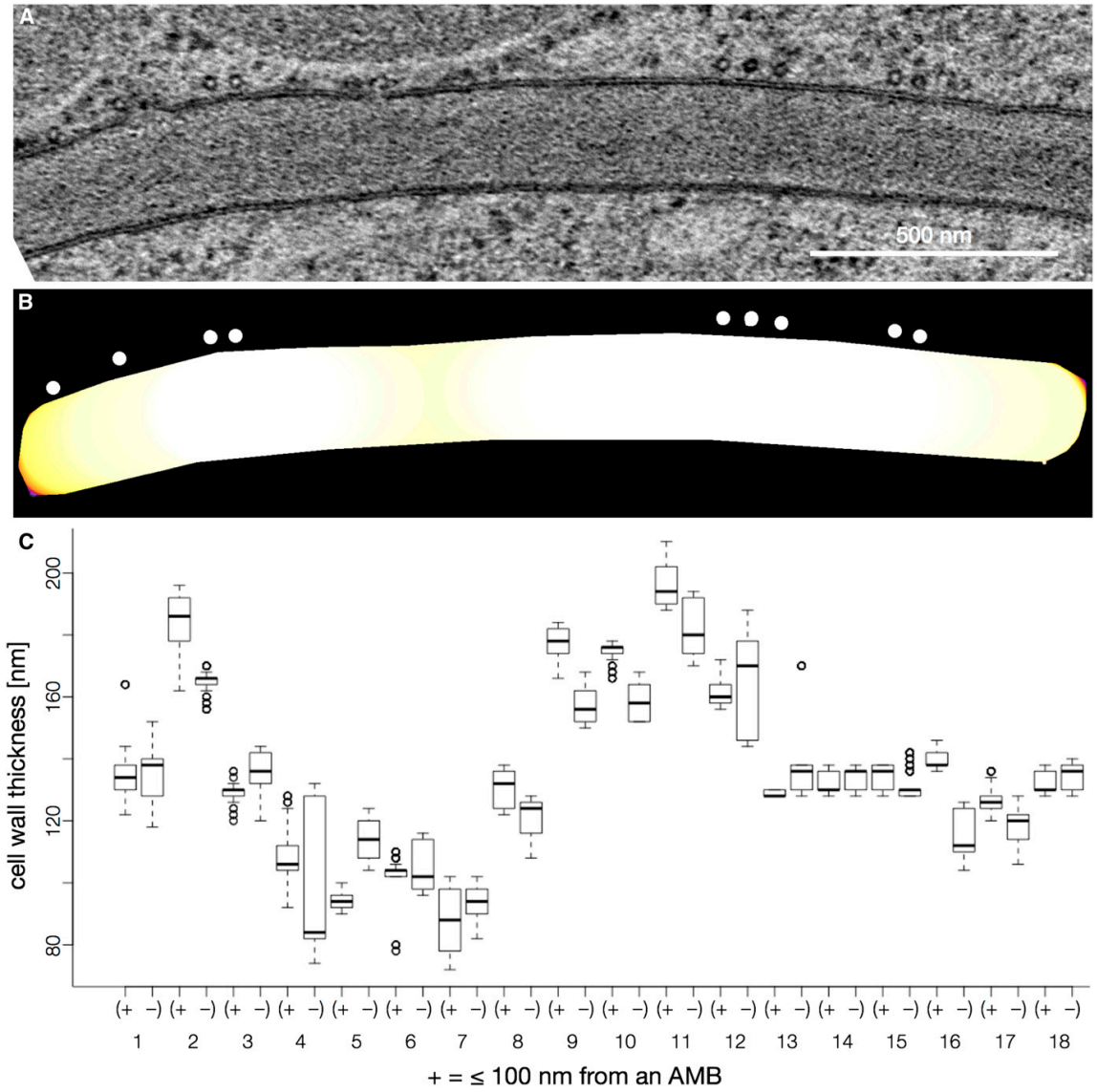

Figure 10. The domains of the anticlinal wall that underlie anticlinal microtubule bundles (AMBs) are not thicker than adjacent cell wall domains lacking microtubules. A, TEM image of a paradermal section that was perpendicular to the anticlinal wall. B, Thresholded image of A in which the cell wall is color coded from thinnest (yellow) to thickest (white). Microtubules are indicated with white circles. C, Box plot of cell wall thickness values in cell wall domains that overlaid the AMBs (+) and in adjacent regions of the wall not associated with microtubules (−).

membrane and tended to reside within one of the two cells. If the cell had a local convex geometry, the microtubules were often, but not always, localized along the convex cell surface. A gallery of TEM images that were analyzed as part of Figure 10 is provided as Supplemental Figure S13. In bundles 4 and 6, there were five or more microtubules (some with visible cross-links to the plasma membrane) within a bundle, and the local wall thickness in these two regions was among the thinnest in the entire data set (Fig. 10C). These data indicate that microtubule bundles do not necessarily mark regions of the wall with an increased cell wall thickness. We could not distinguish the thickness of the two individual anticlinal cell walls in

these TEM images because the middle lamella was not clearly detected, so we simply divided the total cell wall width by 2. The geometries of the adjacent cells hardly varied at the spatial scale of our cell wall thickness analyses, and alternating patterns of microtubules in adjacent cells were not detected. Therefore, there was no indication that either microtubules or complementary cell shapes could generate a constant total wall thickness but alternating patterns of varying wall thickness in the opposing cells. However, we are not saying that the material properties in the wall do not vary as a function of anticlinal microtubule bundle localization. For example, an anticlinal microtubule bundle could increase the local proportion of aligned cellulose fibers in the wall, which could influence the local strain behaviors of the cell.

DISCUSSION

Leaf epidermal morphogenesis is a multiscale process in which interdigitated growth of expanding polyhedral pavement cells drives epidermal growth (Panteris et al., 1993, 1994; Frank et al., 2003; Zhang et al., 2011). This evolutionarily conserved form of tissue morphogenesis may influence the morphology or mechanical integrity of the leaf. Existing models describe a feedback control mechanism in which the output of signaling is a stable pattern of actin filaments and microtubules in opposing cells that pattern the wall and specify the sites for lobe initiation (Fu et al., 2005; Xu et al., 2010). Such alternating patterns are widespread in lobed cells and may reflect a valid cell shape control mechanism in many cell types such as the crenulated epidermal cells in maize (*Zea mays*) leaves (Panteris and Galatis, 2005). Our data indicate that there are no such stable cytoskeletal arrays in the anticlinal cortex of Arabidopsis pavement cells, and their localization does not predict or reflect the changing geometry of the cell boundary in a simple way.

Our live cell imaging pipeline allowed us to analyze lobe formation at high spatial resolutions over the time scale of hours during which lobe formation occurs. The first detectable landmark of lobe initiation is a shallow deflection of ~300 nm at the interface of the anticlinal and periclinal walls (Supplemental Fig. S4). Therefore, the challenge is to discover the cytoskeletal control and cell wall patterning mechanisms that drive a subtle but stable cell wall feature that sets the polarized growth process into motion. Our data are not consistent with a model in which a plasma membrane-localized PIN auxin efflux carrier is a key molecule for pavement cell polarization. We found that a *pin1-1* mutant had no noticeable effect on lobe formation at several developmental stages (Table I), and the functional PIN1::PIN1:GFP reporter (Benková et al., 2003) was not expressed in fields of leaf and cotyledon pavement cells that are making new lobes. PIN3, PIN4, and PIN7 are expressed in fields of lobing pavement cells, but with no clear clustering within protrusions as described previously (Xu et al., 2010). A broader genetic analysis of plasma membrane-localized PINs also failed to detect a lobing phenotype (Table II). The *pin3*, the *pin3;7* double, and the *pin3;4;7* triple mutants had wild-type lobe numbers. The severely dwarfed *pin1;3;4;7* quadruple mutant had much smaller cells but only a slight reduction in lobe number. We also failed to detect a lobing defect in *ric4* (Table II), which is proposed to be a target of *PIN1* signaling that controls cortical actin polymerization and functions in a negative feedback loop that is needed to generate alternating patterns of cortical actin and microtubules in developing pavement cells (Fu et al., 2005; Xu et al., 2010). These negative results do not reflect our inability to detect a subtle lobing initiation phenotype using LobeFinder, because the *dis2/arpc2* phenotypes were clear (Table II). The negative data with *ric4*, and the lack of stable patterns of microtubules along the anticlinal wall, also suggest that there are no stable cortical actin domains that are proposed to alternate with microtubules via a PIN-based mechanism (Fu et al., 2005; Nagawa et al., 2012). We are not claiming that auxin has no role in lobe formation, as long-term treatments with exogenous auxin can increase cell lobe number (Xu et al., 2010; Gao et al., 2015). Exogenous auxin may extend the developmental window during which pavement cells are competent to form lobes, or auxin may have a general effect on the cell wall that makes lobing more permissive. Our results suggest that the details of the ROP-based signaling pathways that influence lobe formation (Fu et al., 2002; Qiu et al., 2002) remain to be discovered.

Our results on PINs do not agree with those from previous publications (Fu et al., 2005; Xu et al., 2010; Guo et al., 2015). Conflicting data can arise because pavement cell morphogenesis is far more complicated and variable than previously thought. Their shapes and sizes depend on their developmental stages and are strongly affected by their positions on the organ. Cell population-based phenotyping is unreliable, and the recent movement toward time-lapse analysis of lobing is a step in the right direction (Zhang et al., 2011; Armour et al., 2015). The prior lack of an objective lobe detection tool like LobeFinder (Wu et al., 2016), and the peak prominence feature (Supplemental Fig. S4) used here, made it more likely that subjective phenotyping could cause variability among different groups working on the same mutants with weak phenotypes. We attempted to minimize these errors by (1) analyzing *pin1-1* at several developmental stages at specific leaf positions; (2) using LobeFinder as a validated lobe-counting tool; and (3) using the circularity parameter to objectively analyze cell shape (Tables I and II). A polarized localization of PIN proteins has been reported in lobe tips following transient ectopic overexpression (Xu et al., 2010; Li et al., 2011; Guo et al., 2015). However, the interpretation of localization data in pavement cells also is complicated, even when tagged proteins are expressed with native promoters. First, the brightness of tagged protein signals along the cell perimeter is highly sensitive to small tilt angles of the sample and the highly variable cytoplasmic density and

membrane geometry along the cell perimeter. More importantly, given the unpredictable and heterogenous growth behaviors of lobing pavement cells, it is impossible to relate the localization of a candidate regulatory factor to lobe initiation based on a single image. At present, we are not aware of any protein that localizes to and predicts the sites of lobe initiation.

Based on a previous report (Armour et al., 2015) and current models in which long-lived anticlinal microtubule bundles generate local wall thickenings that influence lobe formation (Fu et al., 2005; Panteris and Galatis, 2005), we expected to detect populations of stable anticlinal microtubules that predict lobe initiation sites. Our quantitative long-term time-lapse imaging analysis of microtubules and cell geometry showed that this clearly was not the case. The same microtubule signal peak was rarely, if ever, present at the same location 1 h later in regions undergoing lobe formation (Fig. 5E). In our time-lapse experiments, it was possible to backtrack to the time points that immediately preceded lobe initiation and test for anticlinal microtubules in the cortical regions that were expected to give rise to lobes at later time points (Supplemental Fig. S12). Anticlinal microtubules were not continuously present at these locations, conclusively showing that these microtubules are not stable structures that predict the site of lobe initiation.

Microtubule turnover also was observed in highly lobed cells (Supplemental Fig. S8), and by graphing microtubule and cell geometry dynamics on a common coordinate system, it was clear that microtubule signals were not strictly correlated with a specific cell shape in either lobing or lobed segments (Supplemental Figs. S7 and S8). The limitation of not knowing from which cell the microtubules originate does not weaken our ability to test the hypothesis that stable anticlinal microtubules are enriched in highly curved regions of the cell compared with the relatively straight flanking region of the lobe. If anticlinal microtubules were stable markers of lobe initiation and lobe outgrowth, the microtubule signals would strongly correlate with regions of high local cell curvature, and they do not. We examined the persistence of microtubule peak signals within existing lobes by dividing the cortex into an extreme apical domain and an adjacent flanking domain that was spatially isolated from the convex region of both cells at the cell-cell interface. Even in lobes that were present through the entire time lapse, anticlinal microtubules were equally likely to be observed at the apex and flanking regions (Fig. 6B). Our data clearly show that cell geometry is not sufficient to predict the patterns of anticlinal microtubules.

However, we are not stating that there is never a correlation between cell geometry and microtubule localization. Microtubule localization to the convex regions of cells has been reported for lobed pavement cells for many species (Panteris and Galatis, 2005) and has been reported repeatedly in Arabidopsis pavement cells (Wasteneys et al., 1997; Fu et al., 2002, 2005; Qiu et al., 2002; Zhang et al., 2011; Sampathkumar et al., 2014). Our TEM analyses here detected a similar bias for microtubule localization to the convex regions of cells (Fig. 10; Supplemental Fig. S13). Microtubules may be more likely to reside in convex regions of one cell, and if there is a transcellular mechanism to inhibit microtubule polymerization in the adjacent cortical region of a neighboring cell, this would generate an offset pattern of microtubules in curved regions of opposing cells. This offset pattern is not always observed (Supplemental Fig. S9C), but when it is present, it cannot be resolved in our analysis because we cannot distinguish the cell of origin for the microtubules. In any case, microtubule localization to convex regions of the cell does not explain how a convex shape is generated in the first place.

It was claimed previously that cortical periclinal microtubules were enriched near the convex region of the cell compared with the concave region of the adjacent cell prior to lobe formation (Armour et al., 2015). We found no clear differences in the occupancy of cortical microtubules in the periclinal cortex of the two adjacent cells prior to lobe formation (Fig. 8). We do not believe that we successfully detected and segmented every microtubule in the periclinal cortex, because the image acquisitions were optimized to measure the brighter anticlinal microtubule bundles. However, assuming that all regions of the cell were equally affected, our data suggest that the cortical density of microtubules does not differ greatly among subcellular domains of adjacent cells during lobe formation. We believe that our conclusions differ from those of Armour et al. (2015) because we more accurately detected the timing and location of lobe formation and we sampled microtubule and cell shape dynamics repeatedly prior to lobe initiation. Further analysis of local microtubule order, origin of nucleation, and persistence as a function of lobe initiation will provide greater insight (see below).

Anticlinal and periclinal microtubules clearly have a role in lobe formation based on convincing genetic and pharmacological data (Qiu et al., 2002; Kotzer and Wasteneys, 2006; Armour et al., 2015). However, our results indicate that there are diverse populations of anticlinal and periclinal microtubules that likely have multiple functions in the cell. Lobe initiation is superimposed on diffuse growth and planar increases in cell area (Supplemental Movies S1 and S2), and the most obvious global function of microtubules is to modulate the strain patterns of the anticlinal and periclinal cell faces. Anticlinal microtubule localization within lobes has been reported previously and discussed by our group (Qiu et al., 2002; Zhang et al., 2011), and the results here further indicate that anticlinal microtubules have a general role to promote anisotropic growth of the anticlinal wall. Anticlinal microtubules may serve as transient cortical landmarks to pattern the local synthesis of aligned cellulose fibers that limit the height of the anticlinal wall and promote the expansion of the anticlinal wall in the plane of the epidermis. The anticlinal microtubules do not appear to generate local

regions of increased cell wall thickness. A direct TEM analysis of cell wall thickness as a function of the location of anticlinal microtubule bundles also failed to detect an increased cell wall thickness where it overlaid anticlinal microtubule bundles (Fig. 10). An anticlinal microtubule position and their persistence may have more to do with the tension and shear forces in the wall that vary depending on the geometry of cell/tissue and the local growth behaviors of adjacent cells. Periclinal microtubules with variable orientations may pattern a relatively isotropic but thicker outer cell wall that would resist bulging out of the plane of the leaf surface and enable broad regions of the outer cell wall to expand symmetrically. Therefore, the observation that average microtubule density does not vary greatly along the periclinal cell cortex between two cells is easily explained (Fig. 8).

The distribution of microtubules in the anticlinal cortex is not completely random. They are highly aligned parallel to the leaf surface (Supplemental Fig. S6). The microtubule array in cotyledon pavement cells can align parallel to predicted patterns of cell wall stress, and a static finite element model of a pavement cell predicts that tension forces are maximal at the interface of the outer periclinal and anticlinal walls (Sampathkumar et al., 2014). Tension forces in the anticlinal wall would be expected to be oriented toward the outer periclinal wall, and these forces may dictate the observed alignment of microtubules perpendicular to the outer periclinal wall (Fig. 5C; Supplemental Fig. S6). If microtubules can sense and align parallel to cell wall stress tensors, this may be a plausible mechanism to bias microtubules in the anticlinal wall of any elongated epidermal cell toward a transverse alignment. Time-lapse imaging detected many instances in which a subset of microtubule signal persistence peaks correlated weakly with future sites of lobe initiation (Supplemental Fig. S12). However, their locations were not correlated with cell curvature. Instead, the spatial distributions of persistent microtubule signals were most strongly correlated with tissue geometry: microtubule signals increased away from three-way cell wall junctions in lobing pavement cells (Fig. 9). This pattern also is consistent with predicted cell wall stress patterns, as the magnitude of cell wall stress was predicted to be reduced near three-way junctions, where the cell wall is mechanically reinforced by adjacent cells (analogous to a supported beam; Sampathkumar et al., 2014). Cell wall stress also depends on cell wall thickness (Yanagisawa et al., 2015). Perhaps the localized clustering of microtubules in the thin sections of the anticlinal wall (Supplemental Fig. S13) reflects the localized response of the microtubule system to local regions of increased growth, transient wall thinning, and elevated cell wall stress. Collectively, the above results suggest that stress patterns in the cell wall, due in part to tissue geometry, may pattern the microtubule system and explain why simple parameters like local cell curvature do not explain microtubule patterns. Finite element computational modeling combined with multivariate live-cell imaging is a powerful method with which to analyze how cytoplasmic components, cell wall mechanical properties, and wall stress interact during polarized diffuse growth (Yanagisawa et al., 2015). The development of realistic finite element growth models of pavement cell clusters has the potential to guide experiments that unravel the interactions and feedback controls among cell geometry, cell signaling, and cell wall patterning during epidermal morphogenesis.

We are still left with unanswered questions about which subset of microtubules influences lobe formation. Our data indicate that the microtubules that pattern lobes are transient features that cannot be resolved in an approximately hourly sampling regime. It is also apparent from this and previous work that future experiments should thoroughly analyze the presence and order of periclinal microtubules as a function of lobe initiation (Panteris and Galatis, 2005; Szymanski, 2014). Anticlinal microtubules can exist either as bundles that are restricted to the anticlinal wall or as a component of a transfacial microtubule array that spans the anticlinal and periclinal walls (Zhang et al., 2011). We propose that this later class of aligned transfacial microtubules can pattern cellulose fibers that persist in the primary cell wall to generate a localized patch of anisotropic cell wall that expands asymmetrically at both the anticlinal and periclinal faces (Szymanski, 2014). Locally aligned periclinal microtubules and cellulose microfibrils adjacent to the cell-cell interface could generate an anisotropic strain that could be sufficient to break symmetry and initiate a lobe. Given that a very small deformation of the anticlinal wall is needed to initiate a lobe, it may be that relatively few, short-lived microtubules are sufficient to pattern the cell wall and symmetry-breaking events. Perhaps subsets of specialized transfacial microtubules are decorated with microtubule-associated proteins that efficiently recruit cellulose synthase complexes and orient their motility in the plasma membrane. Solving the puzzle of microtubule-dependent lobing will require genetic and cellular analyses of microtubule order, cell wall strain, and lobe initiation at high spatial and temporal resolutions.

MATERIALS AND METHODS

Plant Materials and Growth Conditions

Arabidopsis (*Arabidopsis thaliana*) seedlings were grown at 22°C on one-half-strength Murashige and Skoog medium with 1% Suc (w/v) and 0.8% (w/v) Bacto agar under continuous illumination. Arabidopsis ecotype Columbia-0 was used as the wild type. PIN null mutants were described previously: *pin1-1* (Sawchuk et al., 2013), *pin3-3* (Friml et al., 2002), *pin4-2* (Friml et al., 2002), and $pin7^{EN}$ (Blilou et al., 2005). The *pin* double, triple, and quadruple mutants were obtained by crossing the above lines. PIN3::PIN3:GFP was described previously (Zádníková et al., 2010). PIN7::PIN7:GFP is a translational fusion of *PIN7* (AT1G23080; −1,537 to +2,830; primers: PIN7 prom *Sal*I forw and PIN7 UTR *Kpn*I rev) to EGFP (Clontech; insertion at +921 of PIN7; primers: EGFP *Sac*I forw and EGFP *Sac*I rev). Primer sequences are as follows: PIN7 prom *Sal*I forw, 5′-TAAGTCGACAAAAATAATATTTTTATTTAAGATAATTATG-3′; PIN7 UTR *Kpn*I rev, 5′-TATGGTACCCTTTCTCAAATAATCTC-3′; EGFP *Sac*I forw, 5′-TAAGAGCTCAGGTGAGCAAGGGCGAGGAG-3′; and EGFP *Sac*I rev,

5′-TATGAGCTCCCTTGTACAGCTCGTCCATGC-3′. PIN4::PIN4:GFP is a translational fusion of PIN4 (AT2G01420; −4,598 to +3,095; primers: PIN4 prom *Pst*I forw and PIN4 1032 *Sal*I rev, PIN4 1033 *Sal*I forw and PIN4 UTR *Eco*RI rev) to EGFP (Clontech; insertion at +1,032 of PIN4; primers: EGFP *Sal*I Forw and EGFP *Sal*I Rev). Primer sequences are as follows: PIN4 prom *Pst*I forw, 5′-TCTCTGCAGTTTGTGTATCTTAATTATTTGAGTATG-3′; PIN4 1032 *Sal*I rev, 5′-TATGTCGACGTCATGGCTCGCTTTGCTATC-3′; PIN4 1033 *Sal*I forw, 5′-TATGTCGACGCTAAGGAGCTTCACATG-3′; PIN4 UTR *Eco*RI rev, 5′-TACGAATTCCAGTATAAACCACTTAACTAGAAAC-3′; EGFP *Sal*I Forw, 5′-TATGTCGACGTGAGCAAGGGCGAGGAG-3′; and EGFP *Sal*I Rev, 5′-TATGTCGACCTTGTACAGCTCGTCCATGC-3′. *ric4-2* is a T-DNA insertional line obtained from the Arabidopsis Biological Resource Center (SALK_015799), and its genotype was confirmed by PCR analysis. The plasma membrane marker plasmid, pm-RB (CD3-1008; Nelson et al., 2007), was obtained from the Arabidopsis Biological Resource Center and introduced using *Agrobacterium tumefaciens*-mediated transformation to a GFP:TuB6-expressing line in the Columbia-0 background. GFP-tagged PINs and GFP:TUB6 were imaged as described below for confocal microscopy and time-lapse imaging.

Imaging and Analysis of Cotyledon Pavement Cell Shape: Population-Level Studies

Whole seedlings were stained using FM4-64 (1 μM) for 15 to 30 min. Cotyledons were dissected and imaged using a chambered slide and imaged using a Bio-Rad 2100 laser-scanning confocal microscope mounted on a Nikon Eclipse E800 stand. Samples were excited with a 488-nm laser, and the fluorescence signal was collected using a 490-nm long-pass dichroic and a 500- to 550-nm band-pass emission filter. A 40× oil-immersion, 1.3 numerical aperture (NA) objective was used for 2- and 5-DAG cotyledons, and a 20× 0.5 NA objective was used for 10-DAG cotyledons. Image fields from the apical half of the cotyledon were obtained from 2 DAG, and the apical third of the cotyledon was used for 5 and 10 DAG. Complete pavement cells that were not part of the stoma cell linage were traced manually using the polygon tool in FIJI 4.0 and ROIs were splined using the line tool option in FIJI. ROIs were analyzed using LobeFinder (Wu et al., 2016), and statistical analyses were done in R.

Confocal Microscopy and Time-Lapse Imaging of Lobe Initiation

The 1.5-DAG whole seedlings were mounted in our homemade long-term chamber system as described previously (Yanagisawa et al., 2015). Confocal fluorescence microscopy was performed using a 60× C-Apo 1.2 NA water-immersion objective. Images were acquired using a spinning disk CSU-10 confocal head (Yokogawa Electric) mounted on a Zeiss Oberver.Z1 inverted microscope controlled using Slidebook software (Intelligent Imaging Innovations). mCherry and GFP were excited by 561- and 488-nm laser lines, respectively. Approximately hourly sequential image acquisition was done using an Evolve 512 camera (Photometrics) through band-pass filters (617/73 and 482/35; Semrock).

Analysis of Microtubules in Segments

Using the plasma membrane channel, cell boundaries spanning from three-way junctions were segmented manually using the segmented line tool with the spline function activated in FIJI and saved as an ROI. After all time points were obtained for a segment, the ROIs were saved as a zip file from the ROI Manager window in FIJI. To obtain information about anticlinal microtubules and segment geometry, the macro AMB.IJM was used, which asks for an input folder containing microtubule-tagged image stacks, an output folder, and the ROI.zip file for the segment. The output will produce, for each time point, a .csv file containing information about the summed resliced anticlinal microtubules and a .txt file containing the *xy* coordinates of the segment. For details, including input requirements and additional options this macro, refer to the AMB_README file included as part of the documentation provided with the GitHub submission (see below). In Matlab, the code InputFiji.m will do the following processes to the *xy* coordinates: move one end to the *xy* origin, rotate the segment so that both ends are in the *x* axis line, interpolate the segment to 500 points and normalize its length from 0 to 1, identify lobes using the prominence method in the findpeaks algorithm, returning for each lobe in a segment its peak position and midheight width, which, in turn, are used to calculate the lobe apex and flanking regions. To the AMB file (.csv), it will do the following: calculate a line scan of anticlinal microtubules in the segment by summing the column values of the image text file and normalize the signal intensity from 0 to 1, interpolate the line to 500 points and normalize the segment length from 0 to 1, identify anticlinal microtubule peaks using the prominence method in the findpeaks algorithm, obtaining the peak position for each identified peak. The code will produce an overlapping plot containing both the normalized anticlinal microtubule signal and the normalized segment with identified lobes subdivided into apex and flank for each time point. It will also calculate a Pearson correlation coefficient for both temporal and location base analysis between the anticlinal microtubule and the absolute lobe height value. For details including additional analysis and options about this code, refer to InputFiji_README. For sublobe microtubule localization, overlapping plots of anticlinal microtubule signals and segment shape produced from Matlab were combined as a stack in FIJI and counted for each subregion. The sum of occupancy was divided by the number of time points and multiplied by 100 to obtain a percentage. Persistence plots were done by plotting the anticlinal microtubule signals using the area tool plot in Matlab. PCC analysis of the final shape with anticlinal microtubule persistence was conducted using the sum of anticlinal microtubule signal with the final segment shape acquired. For microtubule analyses at three-way junctions, the areas of anticlinal microtubules on the first and last five pixels (1.06 μm) of the segment were calculated using the trapz function in Matlab. For the middle section, 10 pixels (2.12 μm) were used. PCC analyses were performed in Matlab. Other statistical analyses were done in R. Code is available at https://github.com/yamsissamy/PlantPhys2017.

Analysis of Microtubules along the Periclinal Cortex

Using the plasma membrane channel, ROIs of equal area dimensions at the convex and concave sides of a lobe were created using the polygon selection in FIJI. The ROIs were analyzed from the beginning of the time lapse to the time of lobe detection. The images were processed in the following manner: smooth, background reduction using a 15-pixel ball, sharpening, despeckle, Z-projection using the max intensity option, band-pass filtering from one to five pixels, binarize, skeletonized, and saved as an eight-bit image. The total integrated intensity was measured for each ROI and divided by 255 to obtain the number of occupied pixels (OP). The total number of pixels (TP) in the ROI was determined. The occupancy percentage was calculated as follows: occupancy = 100 × (OP/OT).

TEM and Cell Wall Thickness Analysis

The 2-DAG cotyledons were high-pressure frozen with a Leica EMPact2 high-pressure freezer in 0.2-mm-deep planchets (Leica Microsystems) using 0.15 M Suc as a cryoprotectant. Next, freeze substitution was carried out in a Leica AFS2 automated freeze substitution unit in 1% OsO_4 (EMS). The samples were dehydrated by solution exchange with increasing concentrations of acetone. After dehydration, the samples were infiltrated with Eponate 812 (EMS) by incubating at room temperature for several hours to overnight in increasing concentrations of resin diluted in acetone. The samples were transferred to capsules, and the resin was polymerized in a 60°C oven overnight. Resin-embedded samples were sectioned to ~60 nm with a Diatome diamond knife on a Leica EM UTC ultramicrotome (Leica Microsystems). Sections were collected on 0.5% formvar-coated slot grids (SPI Supplies) and were poststained for 3 min with 2% aqueous uranyl acetate and for 2 min with Reynolds lead citrate. Images were taken with a four-megapixel Gatan UltraScan 1000 camera on a FEI Tecnai G2 20 Twin 200-kV LaB6 transmission electron microscope. To analyze cell wall thickness in relation to anticlinal microtubule bundles, TEM micrographs were segmented using FIJI's circle selection tool for microtubules and the polygon selection tool for cell walls. ROIs were selected to include cell wall segments within 100 nm of a point on the cell wall adjacent to microtubules within a bundle. Anticlinal microtubule bundles contained two or more microtubules that were within ~50 nm. Cell wall thickness was compared with an equivalent length of adjacent cell that did not overlay anticlinal microtubule bundles. The images were then converted to binary and duplicated. One binary image was processed to a Eulerian distance map and the other to an image skeleton. The FIJI image calculator tool was used to identify cell wall thickness values from the distance map along the skeleton points. Those values were saved as *xy* value coordinates. The middle lamella was not detectable in these samples, so the cell wall thickness values were divided by 2 to account for the presence of two primary cell walls and were analyzed and displayed as box plots using R. Cell wall segments from six independent cells were analyzed.

Supplemental Data

The following supplemental materials are available.

Supplemental Figure S1. Neither *pin1-1* nor *pin1;3;4;7* leaf pavement cells have a detectable lobing phenotype.

Supplemental Figure S2. PIN1 is expressed only in leaf margins of young developing leaves.

Supplemental Figure S3. Lobe formation is not inhibited in plasma membrane-localized PIN mutants or its effector RIC4 but is affected in distorted mutants.

Supplemental Figure S4. A robust method for lobe detection along the cell segment boundary.

Supplemental Figure S5. Expansion in subregions of a segment can warp an adjacent subregion so that it temporarily falls below the identification threshold.

Supplemental Figure S6. Anticlinal microtubules are perpendicular to the leaf surface plane.

Supplemental Figure S7. Pearson correlation analysis between microtubule signals and segment shape for lobing segments.

Supplemental Figure S8. Pearson correlation analysis between microtubule signals and segment shape for lobed segments.

Supplemental Figure S9. Pearson correlation analysis between microtubule signals and segment shape for segments of 5-DAG seedlings.

Supplemental Figure S10. Additional examples of the correlation study between microtubule persistence and final segment shape for lobing segments.

Supplemental Figure S11. Additional examples of the correlation study between microtubule persistence and final segment shape for lobed segments.

Supplemental Figure S12. Microtubule signal persistence before lobe formation occurred but is not highly correlated with new lobe formations.

Supplemental Figure S13. Anticlinal microtubule bundles do not correspond to regions of increased thickening of the anticlinal cell wall.

Supplemental Movie S1. Time-lapse capture of a field of expanding pavement cells.

Supplemental Movie S2. Time-lapse capture of a field of expanding pavement cells.

Supplemental Movie S3. Time lapse of anticlinal microtubules for segment 4 in Supplemental Movie S1.

Supplemental Movie S4. Time-lapse images of anticlinal microtubules that are illustrated in Figure 5.

ACKNOWLEDGMENTS

We thank Austin Blackwell and Sarah Mendoza for help with *pin* genotyping and Peter Ciesielski for assistance with TEM sample preparation. Thanks also to Joe Turner and David Umulis for helpful pavement cell discussions.

Received October 27, 2017; accepted November 22, 2017; published November 13, 2017.

LITERATURE CITED

Abe T, Hashimoto T (2005) Altered microtubule dynamics by expression of modified alpha-tubulin protein causes right-handed helical growth in transgenic Arabidopsis plants. Plant J **43:** 191–204

Abe T, Thitamadee S, Hashimoto T (2004) Microtubule defects and cell morphogenesis in the lefty1lefty2 tubulin mutant of Arabidopsis thaliana. Plant Cell Physiol **45:** 211–220

Ambrose JC, Shoji T, Kotzer AM, Pighin JA, Wasteneys GO (2007) The *Arabidopsis* CLASP gene encodes a microtubule-associated protein involved in cell expansion and division. Plant Cell **19:** 2763–2775

Andriankaja M, Dhondt S, De Bodt S, Vanhaeren H, Coppens F, De Milde L, Mühlenbock P, Skirycz A, Gonzalez N, Beemster GT, et al (2012) Exit from proliferation during leaf development in Arabidopsis thaliana: a not-so-gradual process. Dev Cell **22:** 64–78

Armour WJ, Barton DA, Law AM, Overall RL (2015) Differential growth in periclinal and anticlinal walls during lobe formation in *Arabidopsis* cotyledon pavement cells. Plant Cell **27:** 2484–2500

Baskin TI (2005) Anisotropic expansion of the plant cell wall. Annu Rev Cell Dev Biol **21:** 203–222

Benková E, Michniewicz M, Sauer M, Teichmann T, Seifertová D, Jürgens G, Friml J (2003) Local, efflux-dependent auxin gradients as a common module for plant organ formation. Cell **115:** 591–602

Blilou I, Xu J, Wildwater M, Willemsen V, Paponov I, Friml J, Heidstra R, Aida M, Palme K, Scheres B (2005) The PIN auxin efflux facilitator network controls growth and patterning in *Arabidopsis* roots. Nature **433:** 39–44

Burk DH, Liu B, Zhong R, Morrison WH, Ye ZH (2001) A katanin-like protein regulates normal cell wall biosynthesis and cell elongation. Plant Cell **13:** 807–827

Buschmann H, Lloyd CW (2008) *Arabidopsis* mutants and the network of microtubule-associated functions. Mol Plant **1:** 888–898

Cosgrove DJ (2016) Plant cell wall extensibility: connecting plant cell growth with cell wall structure, mechanics, and the action of wall-modifying enzymes. J Exp Bot **67:** 463–476

El-Din El-Assal S, Le J, Basu D, Mallery EL, Szymanski DB (2004) *DISTORTED2* encodes an ARPC2 subunit of the putative Arabidopsis ARP2/3 complex. Plant J **38:** 526–538

Elsner J, Michalski M, Kwiatkowska D (2012) Spatiotemporal variation of leaf epidermal cell growth: a quantitative analysis of Arabidopsis thaliana wild-type and triple cyclinD3 mutant plants. Ann Bot **109:** 897–910

Frank MJ, Cartwright HN, Smith LG (2003) Three Brick genes have distinct functions in a common pathway promoting polarized cell division and cell morphogenesis in the maize leaf epidermis. Development **130:** 753–762

Friml J, Benková E, Blilou I, Wisniewska J, Hamann T, Ljung K, Woody S, Sandberg G, Scheres B, Jürgens G, et al (2002) AtPIN4 mediates sink-driven auxin gradients and root patterning in Arabidopsis. Cell **108:** 661–673

Fu Y, Gu Y, Zheng Z, Wasteneys G, Yang Z (2005) Arabidopsis interdigitating cell growth requires two antagonistic pathways with opposing action on cell morphogenesis. Cell **120:** 687–700

Fu Y, Li H, Yang Z (2002) The ROP2 GTPase controls the formation of cortical fine F-actin and the early phase of directional cell expansion during *Arabidopsis* organogenesis. Plant Cell **14:** 777–794

Fu Y, Xu T, Zhu L, Wen M, Yang Z (2009) A ROP GTPase signaling pathway controls cortical microtubule ordering and cell expansion in Arabidopsis. Curr Biol **19:** 1827–1832

Fujita M, Himmelspach R, Ward J, Whittington A, Hasenbein N, Liu C, Truong TT, Galway ME, Mansfield SD, Hocart CH, et al (2013) The *anisotropy1* D604N mutation in the Arabidopsis cellulose synthase1 catalytic domain reduces cell wall crystallinity and the velocity of cellulose synthase complexes. Plant Physiol **162:** 74–85

Gao Y, Zhang Y, Zhang D, Dai X, Estelle M, Zhao Y (2015) Auxin binding protein 1 (ABP1) is not required for either auxin signaling or Arabidopsis development. Proc Natl Acad Sci USA **112:** 2275–2280

Guo X, Qin Q, Yan J, Niu Y, Huang B, Guan L, Li Y, Ren D, Li J, Hou S (2015) TYPE-ONE PROTEIN PHOSPHATASE4 regulates pavement cell interdigitation by modulating PIN-FORMED1 polarity and trafficking in Arabidopsis. Plant Physiol **167:** 1058–1075

Higaki T, Kutsuna N, Akita K, Takigawa-Imamura H, Yoshimura K, Miura T (2016) A theoretical model of jigsaw-puzzle pattern formation by plant leaf epidermal cells. PLOS Comput Biol **12:** e1004833

Higaki T, Kutsuna N, Sano T, Kondo N, Hasezawa S (2010) Quantification and cluster analysis of actin cytoskeletal structures in plant cells: role of actin bundling in stomatal movement during diurnal cycles in Arabidopsis guard cells. Plant J **61:** 156–165

Jacques E, Verbelen JP, Vissenberg K (2014) Review on shape formation in epidermal pavement cells of the Arabidopsis leaf. Funct Plant Biol **41:** 914–921

Kotzer AM, Wasteneys GO (2006) Mechanisms behind the puzzle: microtubule-micofilament cross-talk in pavement cell formation. Can J Bot **84:** 594–603

Le J, Mallery EL, Zhang C, Brankle S, Szymanski DB (2006) *Arabidopsis* BRICK1/HSPC300 is an essential WAVE-complex subunit that selectively stabilizes the Arp2/3 activator SCAR2. Curr Biol **16:** 895–901

Li H, Lin D, Dhonukshe P, Nagawa S, Chen D, Friml J, Scheres B, Guo H, Yang Z (2011) Phosphorylation switch modulates the interdigitated pattern of PIN1 localization and cell expansion in Arabidopsis leaf epidermis. Cell Res **21:** 970–978

Nagawa S, Xu T, Lin D, Dhonukshe P, Zhang X, Friml J, Scheres B, Fu Y, Yang Z (2012) ROP GTPase-dependent actin microfilaments promote PIN1 polarization by localized inhibition of clathrin-dependent endocytosis. PLoS Biol **10:** e1001299

Nelson BK, Cai X, Nebenführ A (2007) A multicolored set of *in vivo* organelle markers for co-localization studies in Arabidopsis and other plants. Plant J **51:** 1126–1136

Onoda Y, Schieving F, Anten NPR (2015) A novel method of measuring leaf epidermis and mesophyll stiffness shows the ubiquitous nature of the sandwich structure of leaf laminas in broad-leaved angiosperm species. J Exp Bot **66:** 2487–2499

Panteris E, Apostolakos P, Galatis B (1993) Microtubule organization and cell morphogenesis in two semi-lobed cell types of *Adiantum capillus-veneris* L. leaflets. New Phytol **125:** 509–520

Panteris E, Apostolakos P, Galatis B (1994) Sinuous ordinary epidermal cells: behind several patterns of waviness, a common morphogenetic mechanism. New Phytol **127:** 771–780

Panteris E, Galatis B (2005) The morphogenesis of lobed plant cells in the mesophyll and epidermis: organization and distinct roles of cortical microtubules and actin filaments. New Phytol **167:** 721–732

Paradez A, Wright A, Ehrhardt DW (2006) Microtubule cortical array organization and plant cell morphogenesis. Curr Opin Plant Biol **9:** 571–578

Qiu JL, Jilk R, Marks MD, Szymanski DB (2002) The Arabidopsis SPIKE1 gene is required for normal cell shape control and tissue development. Plant Cell **14:** 101–118

Remmler L, Rolland-Lagan AG (2012) Computational method for quantifying growth patterns at the adaxial leaf surface in three dimensions. Plant Physiol **159:** 27–39

Sahaf M, Sharon E (2016) The rheology of a growing leaf: stress-induced changes in the mechanical properties of leaves. J Exp Bot **67:** 5509–5515

Sampathkumar A, Krupinski P, Wightman R, Milani P, Berquand A, Boudaoud A, Hamant O, Jönsson H, Meyerowitz EM (2014) Subcellular and supracellular mechanical stress prescribes cytoskeleton behavior in Arabidopsis cotyledon pavement cells. eLife **3:** e01967

Savaldi-Goldstein S, Peto C, Chory J (2007) The epidermis both drives and restricts plant shoot growth. Nature **446:** 199–202

Sawchuk MG, Edgar A, Scarpella E (2013) Patterning of leaf vein networks by convergent auxin transport pathways. PLoS Genet **9:** e1003294

Staff L, Hurd P, Reale L, Seoighe C, Rockwood A, Gehring C (2012) The hidden geometries of the *Arabidopsis thaliana* epidermis. PLoS ONE **7:** e43546

Szymanski DB (2014) The kinematics and mechanics of leaf expansion: new pieces to the Arabidopsis puzzle. Curr Opin Plant Biol **22:** 141–148

Szymanski DB, Cosgrove DJ (2009) Dynamic coordination of cytoskeletal and cell wall systems during plant cell morphogenesis. Curr Biol **19:** R800–R811

Tsukaya H, Tsuge T, Uchimiya H (1994) The cotyledon: a superior system for studies of leaf development. Planta **195:** 309–312

Wasteneys GO, Galway ME (2003) Remodeling the cytoskeleton for growth and form: an overview with some new views. Annu Rev Plant Biol **54:** 691–722

Wasteneys GO, Willingale-Theune J, Menzel D (1997) Freeze shattering: a simple and effective method for permeabilizing higher plant cell walls. J Microsc **188:** 51–61

Wernicke W, Jung G (1992) Role of cytoskeleton in cell shaping of developing mesophyll of wheat (Triticum aestivum L.). Eur J Cell Biol **57:** 88–94

Whittington AT, Vugrek O, Wei KJ, Hasenbein NG, Sugimoto K, Rashbrooke MC, Wasteneys GO (2001) MOR1 is essential for organizing cortical microtubules in plants. Nature **411:** 610–613

Wiśniewska J, Xu J, Seifertová D, Brewer PB, Růžička K, Blilou I, Rouquié D, Benková E, Scheres B, Friml J (2006) Polar PIN localization directs auxin flow in plants. Science **312:** 883

Wu TC, Belteton SA, Pack J, Szymanski DB, Umulis DM (2016) LobeFinder: a convex hull-based method for quantitative boundary analyses of lobed plant cells. Plant Physiol **171:** 2331–2342

Xu T, Wen M, Nagawa S, Fu Y, Chen JG, Wu MJ, Perrot-Rechenmann C, Friml J, Jones AM, Yang Z (2010) Cell surface- and rho GTPase-based auxin signaling controls cellular interdigitation in Arabidopsis. Cell **143:** 99–110

Yan DW, Wang J, Yuan TT, Hong LW, Gao X, Lu YT (2013) Perturbation of auxin homeostasis by overexpression of wild-type IAA15 results in impaired stem cell differentiation and gravitropism in roots. PLoS ONE **8:** e58103

Yanagisawa M, Desyatova AS, Belteton SA, Mallery EL, Turner JA, Szymanski DB (2015) Patterning mechanisms of cytoskeletal and cell wall systems during leaf trichome morphogenesis. Nat Plants **1:** 15014

Zádníková P, Petrásek J, Marhavy P, Raz V, Vandenbussche F, Ding Z, Schwarzerová K, Morita MT, Tasaka M, Hejátko J, et al (2010) Role of PIN-mediated auxin efflux in apical hook development of Arabidopsis thaliana. Development **137:** 607–617

Zazímalová E, Murphy AS, Yang H, Hoyerová K, Hošek P (2010) Auxin transporters: why so many? Cold Spring Harb Perspect Biol **2:** a001552

Zhang C, Halsey LE, Szymanski DB (2011) The development and geometry of shape change in Arabidopsis thaliana cotyledon pavement cells. BMC Plant Biol **11:** 27

Zhu XG, Long SP, Ort DR (2010) Improving photosynthetic efficiency for greater yield. Annu Rev Plant Biol **61:** 235–261

4. MICROTUBULES TRANSLATE CELL WALL STRESSES INTO EPIDERMAL MORPHOGENESIS

4.1 Introduction

Over the lifetime of a plant, the vast majority of photosynthetic occurs in leaves. Leaves tend to be thin, however there is incredible diversity in their sizes and shapes [1]. The plant's epidermis plays an important role in decoding different types of hormone signals that can either promote or restrict organ expansion [2]. Time-lapsed tracking and computational modeling has shown that regional variabilities in the rate and direction of growth in the epidermis can dictate the size and shape of organs [5, 8, 31]. However, the means by which individual leaf epidermal pavement cells control their shape and contribute to tissue- and organ-level growth processes remains unknown.

In Arabidopsis, like in the majority of eudicots, ferns, and monocots [3], the most prevalent type of epidermal cell, the pavement cell, has a flatten but highly lobed shape. This cell shape and interdigitation generates thin mechanical stable leaves. The expansion of epidermal cells is highly heterogeneous between neighboring cells [5,8] and there is some evidence of differential subcellular growth rates [32] with no clear rules are available to predict lobe formations. Additionally, lobe formation is a slow process that occurs in the timeframe of hours with its initiation being a subtle $\sim$300 nm deflection [29]. To extract useful information about the mechanism for lobe formation, accurate identification and several snapshots of the cells prior to the symmetry breaking is necessary. A time-lapse approach extends the ability to correlate molecular systems and how their patterning dictates or responds to cell shape.

Pavement cell morphogenesis provides a challenging but useful system to analyze cell polarity and coordinated growth among cells across a cell wall boundary. Initially, static image analysis of *Vigna sinensis* [21] led to a local cell wall thickening model for shape change where splaying microtubules spatially correlated with regions of increased cell wall thickenings at the outer-periclinal/anticlinal wall junction. The lobed phenotype observed was believed to have formed due to the local expansion restriction of the cell wall due to its thickening through cellulose deposition guided by stable microtubules. This model was extended to Arabidopsis pavement cells where a similar correlation of microtubules localization at the convex side of a lobes was observed even if the cell wall thickening was not directly monitored [5, 16, 22, 33]. An alternative mechanism of growth restriction was based on theorized microtubule bands which would act as growth-restricting loops around the cell and generate convex cell regions [25]. In fact these bands have never been shown to predict the sites of lobe formation [29] and only recently has it been shown that there is a subtle bias in cortical microtubules in convex regions of the cell [34]. In an alternative model, microtubules do not locally restrict growth, but instead generate a small patch of isotropic expansion in the outer-periclinal cell wall [4] and this is enough to cause symmetry breaking at the cell-cell interface.

More recently, a number of additional explanations of the morphogenesis process have been generated based primarily on the behavior behaviors of finite element (FE) mechanical models of pavement cells. FE models simulate the cells as thin-walled pressurized shells in which the user has the ability to define the material properties of the wall as a function of location. Majda et al., 2017 [25] propose that cell wall compositional differences between opposing walls drive lobe formation. However this paper analyzed highly lobed cells and provided no clear genetic and biomechanical data that this wall composition difference affects lobe initiation. The plausibility of this particular FE model has also been challenged [28]. Lobe initiation due to buckling activity due to compressive forces has also been predicted using a different finite element model [35]. In this model, expansion of these small symmetry break-

ing events are believed to depend on a stiffness increase due to de-esterified pectin deposition [26]. Lastly, super-resolution imaging of lobed cells revealed the presence of methylesterified homogalacturan nanofibers as longitudinal strips in the anticlinal wall [36]. The methylesterification process of these nanofibers was hypothesized to be the driving force for local anisotropic expansion. Similarly to Bidhendi et al., 2019 [35], it is important to validates these findings using genetics or time-series analyses to determine if these nanofiber structures predict lobe initiation sites. Anticlinal microtubules have a similar longitudinal orientation in pavement cells, but their mere presence does not predict lobe initiation sites [29]

Genetic and pharmacological evidence points to a lobe initiation mechanism involving the microtubule and cellulose systems. Microtubules have been consistently implicated in lobe initiation [4,37,38]. Application of the oryzalin, an established microtubule de-polymerizing drug [12], blocks new lobe formation in pavement cells [5]. Null mutants can provide information of how the lack of functioning proteins can affect the cellular processes, in this case how the morphogenesis of the epidermis cells were affected. For example, the microtubule plus-end tracking protein *MOR1* mutation results in a temperature sensitive protein [39], and example images of unlobed bulged cells has been reported under non-permissive temperatures [37]. A similar phenotype can be observed in selected images of the low crystalline cellulose mutant *any1* [11]. Similar images are shown for the reduced pectin mutant *qua1-1* [40]; however, recent analysis of pavement cell shape shows subtle but clear lobes in cotyledon pavement cells of the *qua1-1* mutant [25]. Supporting this genetic data, chemical inhibition of these systems produced a similar phenotype. Treatment with isoxaben, an transport inhibitor of cellulose synthase complex delivery to the plasma-membrane [13], altered the shape of pavement cells. Interestingly, pectinase treatment disrupting cell shape has not been reported in pavement cells however pectinase treatment on pollen tubes resulted in tubes with swollen tips [41].

Here we determine how lobe initiation occurs in the context of the expanding epidermis of early stage cotyledons testing the hypothesis that local anisotropic regions

along the cell periphery driven by the microtubule directed microfibril deposition initiated the symmetry breaking events. To capture lobe initiation events, long-term and multi-variate imaging of pavement cells were conducted utilizing a plasma-membrane marker to capture the subtle shape changes and a microtubule marker to map their location along the segment in each time-point. Close monitoring of these lobing cells revealed a subset of microtubules that traverse the anticlinal and periclinal walls accurately predict the location and direction of lobe formations. A battery of mutants and inhibitor experiments were conducted to prove that the microtubule-cellulose system is the primary driver of lobe initiation. Realistic 3D finite element modeling of cell clusters and the development of a cell autonomous cell lobing system were used to show the tensile forces in the cell wall likely functions as an upstream patterning element of the microtubule cytoskeleton.

4.2 Results

4.2.1 Sub-segmental analysis of expanding cells fails to link growth with shape and stress

As pavement cells expand irreversibly for days, generating cells that vary wildly in size, lobe number, and shape [3]. Also in the time scales of days, pavement cells can oscillate between lobe initiation and extended maintenance phases in which the cells increase greatly in area but maintain their shape [5, 6]. Therefore TEM and localization analyses based on snapshots of already lobed cell populations [16, 17, 36, 42], cannot provide mechanistic insight. Recently high resolution time-lapsed analysis showed that the new lobe is first detected as a tiny ∼300 nm deflection in the anticlinal cell wall (see diagram Fig. 4.1A) that is stably propagated for hours [29]. Here we initiated time-lapsed analysis cell shape and subcellular strain patterns at 15 minute intervals (Fig. 4.1 B). By tracking the plasma-membrane coordinates between two 3-way cell wall junctions, it was apparent that the height and width of the lobe feature

increased over time, which is not consistent with a growth restriction model (Fig. 4.1 D).

To determine if segment's growth was symmetrical, the distance along the segment was measured to the center of mass of the segment itself for the initial and final time-points (Fig 4.1 E). If the growth was isotropic, then the shape from the first time-point would remain the same and only the magnitude of the distance to the center of mass would increase. It was very clear that these segments were warping locally during the duration of the time-lapse (Fig 4.1 E) which is a characteristic of anisotropic expansion. Cell wall marking experiments have detected subcellular heterogeneity in growth [5,7,32]. Bead labelling exactly at the surface of anticlinal wall is possible but rare, leading to sparse coverage [5, 32]. To overcome this limitation, the previously described fluorescent tagged proteins that localized to the periphery and/or within the plasmodesmata aptly named **p**lasmo**d**esmata **l**ocalized **p**roteins (PDLPs) were used as fiducial markers along the anticlinal wall segments of these cells. PDLP3:GFP expressed under its native promoter, provided the best density along the segment and the particles were displaced primarily in the x-y plane during growth (Fig 4.1 B,C; 4.S1.1 A-C). To obtain the sub-segmental growth rates, the distance between the trackable PDLPs and 3-way junctions were measured over time (Fig 4.S1.1 D-F). For all of the analysis here, the sum of the subsegment growth rates was within 3% of the growth rate of the full segment measured using the terminal 3-way junctions. The displacements were due to growth because when the seedlings kept at kept at 4°C particle displacements were not detectable (Fig 4.S1.2 A-F).

There was a high degree of heterogeneity within individual segments (Fig 4.1 F,H). To determine if there were differences in the growth rates of lobe apex or flanks, segments were assigned as sub-domains of a lobe (Fig 4.1 G - top). Sub-segments that occupied at least 60% of the lobe apex were classified as 'apex' sub-segments, similarly, sub-segments that occupied at least 60% of the lobe flank were classified as 'flank' sub-segment; anything else was classified as 'mixed'. A population level analysis of the apex, flank, and mix sub-segments, showed no difference in growth rates between

these regions (Fig 4.1G – Bottom). This indicates that the growth status of the lobe is not determined solely by its geometry, as previously claimed [27]. Instead these data suggests that there are widespread spatial heterogeneities in the material properties of the cell wall. If cell wall properties were uniform strain behaviors would correlate with the amount of tensile forces in the wall. In order to get an accurate estimate of the cell wall stress patterns of highly pressurized pavement cells, a 3D finite element model of the cell clusters was generated based on live-cell image data (Fig. 4.1I). The FE model simulates the wall as thin walled shell compromised of neo-Hookian hyperelastic composite of isotropic materials (see Methods). The model has been validated using nanoindentation (W. Li, J.A Turner, unpublished results). Because the outer-periclinal wall is not in contact with neighboring cells (Fig. 4.1A) turgor pressure generates strong in-plane tensile forces on this cell face and it pulls upwards on the contiguous anticlinal wall that is glued to the neighboring cell via the middle lamella. When turgor pressure was simulated on these cells, the maximal principal stress in the anticlinal wall was aligned perpendicular to the leaf surface towards the outer-periclinal wall (Fig 4.S1.3) and the stress distribution was broad, and in general, minimal near 3-way junctions (Fig 4.1 K,L - magenta). No clear correlation between the sub-segmental growth rates and the geometry-based stress pattern was seen (Fig 4.1 L). Collectively these data indicate that spatial patterning of cell wall heterogeneity plays an important role in pavement cell morphogenesis. The next step was to determine what gene activities and molecular functions control lobe formation.

The prominence-based coordinate system showed the potential to be a powerful tool and provided an opportunity to not only evaluate how the cell segments shape changes but also the ability to correlate this shape change with the localization of molecular players that are known to be essential for normal cell morphogenesis. However, as previously shown [29] the methodology of shape quantification dictates how cells shape phenotypes are classified. Due to the importance of microfibril alignment and anisotropic expansion and the role of microtubules in microfibril deposition patterning, the importance of these systems on cell morphogenesis was tested in a

genetic and pharmacological approach. This was an important first step which would maximize the value from the aforementioned coordinate system.

4.2.2 Genetic and pharmacological analysis of lobe initiation

There is a plethora of known *Arabidopsis* morphology mutants many of which have been implicated in pavement cell morphogenesis [43]. The majority of these mutants with aberrant cell shape belong to microtubule associated proteins such as katanin mutant (*ktn1-2*) [19], microtubule organization 1 mutant (*mor1-1*) [37, 44]. However other systems such as cellulose, anisotropy1 mutant (*any1*) [11], and pectinase, quasimodo mutant (*qua2-1*) [40, 45] have also showed a reduction in the complexity of these cells shape. By utilizing LobeFinder [46], allowed the objective re-evaluation of known cell shape mutants in mature cotyledons (Fig 4.2, Table 4.1). Surprisingly, *ktn1-2* [47] showed no difference in lobe numbers compared to the wild-type. This was also the case with the double γ-tubulin mutant (*tubg1-1;tubg2-2*) which came as a surprise due to the dramatic organ level phenotypes previously analyzed [48]. In accordance to previous images of defective cell shape [49], the temperature sensitive mutant *mor1-1*, showed clear pavement cell defects most clearly seen in the reduction of lobe numbers when it was grown in non-permissive conditions (Table 4.1). The mutant *any1* defective in cellulose synthase, which has been shown to have a reduction in anisotropic expansion, as expected had a reduce lobe phenotype. The pectin mutant, *qua2-1*, had both a reduced areal growth and lobe number. The high lobe number per cell is deceptive due to the method to which LobeFinder identifies a lobe. LobeFinder works on a cell-by-cell basis, for that reason it does not distinguish between lobes and 3-way junction protrusions. When the *qua2-1* three-way junctions were filtered out, the average of lobe per cell was reduced by 54% changing the lobe per area to dropped to 1.71 ± 0.76. In a subset of the wild-type whose lobe number average was representative of the population, the number of lobes per cell was reduced only 29%.

In agreement with the genetic results, chemical interference of microtubule, cellulose, and pectin systems resulted in aberrant cell shapes. The number of lobes produced under the well-established microtubule depolymerizing drug oryzalin [12] was greatly reduced (Table 4.2). Equally, treatment using isoxaben, a well-known drug that interferes with CesA delivery to the plasma-membrane [13, 50], reduced the lobe rate in these cells. Lastly, partial degradation of pectin, an important polysaccharide found in the middle-lamella, with pectinase [51, 52] interfered with lobe production albeit a lower degree. Importantly, treatment combinations of pectinase with either isoxaben or oryzalin completely blocked the ability for pavement cells to undergo any new lobe formation but the cells continue to expand. These latter results showed how lobe formation is interdependent not only to one specific system but to a mechanism dependent on the microtubule, pectin, and cellulose systems. The microtubule effect is mediated through patterned cellulose synthesis as expected [13]. Short time-lapses imaging of YFP:CesA6 and mCherry:TuA5 at 1 DAG in cells a the lobe formation stage showed strong colocalization a permissive (Fig 4.S2.1). The drastic reduction of lobe number on depolymerized microtubule cells such as those in *mor1-1* under restrictive temperatures and after oryzalin treatment, the dependency of cellulose movement on microtubules, and the lack of live-cell tools to monitor pectin composition on these cells guided us towards the analysis of microtubule patterning in lobing cells.

4.2.3 Transfacial microtubules predicts the location and direction of lobe formation

To test how microtubules organization and localization over time affected cell shape morphogenesis high-temporal and -spatial time-lapses were necessary. Most of the current analysis of microtubule organization in expanding cells base most of their conclusions from either snapshots or limited time-lapses [5, 16, 35, 53]. From previous studies, it was clear that high-temporal resolution was necessary when ana-

lyzing microtubule dynamics since hourly snapshots showed a high degree of change in microtubules localization along the cell periphery [29]. More importantly, lobe initiation involves the deformation of the anticlinal and periclinal walls and analysis of the microtubule system must take place across these walls as well. Snapshots of pavement cells with plasma-membrane and microtubule markers showed that microtubules traverse both anticlinal and periclinal walls (Fig 4.3 A-B) however to obtain these images required both high laser power and an increased in image depth to capture the inner periclinal wall. The principal goal was to map the distribution of microtubules as a function of shape change with the intent of testing the hypothesis that transfacial microtubules persist at future location of lobe formation. Since long-term imaging was a necessity, the imaging conditions were set up to capture the outer-periclinal wall and part of the anticlinal wall as a proxy for microtubules that traverse across the periclinal and anticlinal walls, hereafter referred to as transfacial microtubules. This was an acceptable proxy for these transfacial microtubules as the cell wall tilt of emerging lobes did no show local tilt as a function of lobe initiation or lobe expansion (Fig 4.S3.1), meaning that the anticlinal wall moves together. The shape change of these cells takes hours to emerge [5, 29] but microtubule dynamics takes place in the window of minutes [54, 55]. However, if transfacial microtubules are directing cell shape then their patterning over time is expected to scale up to the cell shape time-frame. To strike a balanced interval between microtubules dynamics and cell shape, 3D long-term time-lapses at an interval of 10 minutes ranging from at least $\sim$4 to 8 hours were conducted. Interval image testing showed a high degree of microtubule organization even in 2 minute interval image captures (not shown) but high interval image depleted the signal rapidly preventing long-term analysis to be conducted. Again, since the goal was to map regions of consistent microtubules over time and not necessarily the organization of individual microtubules, 10 minute interval imaging increased or temporal resolution in long-term time-lapses. To clearly score the location of transfacial microtubules along the segment, the image stack was processed (Fig 4.3E-H) to get a composite image of both anticlinal wall and outer-

periclinal wall for both neighboring cells (Fig 4.3I), for further detail see method sections. Tracking the location of transfacial microtubules along the segment over time prior to lobe detection showed that transfacial microtubules localized at the future regions of lobe formation (Fig 4.3 J). More importantly, the transfacial microtubules across the anticlinal wall was bias towards the cell to which the lobe would expand into (Fig 4.3I-top histogram). In all 6 time-lapses analyzed, there was a clear peak of transfacial microtubules at the location where the new lobe emerged (Fig 4.S3.2).

To remove the labor-intensive manual scoring from these analyses and to increase the quantity of segments analyzed, a new microtubule workflow was created. The goal of the semi-automated approach was to capture the increase microtubule presence at the future convex side of the new lobe. The dominant orientation of microtubule alignment at the outer-periclinal and anticlinal wall is perpendicular on the straighten segment (Fig 4.3I) [29]. Extracting the signal intensity of the anticlinal and outer-periclinal walls, produced a 2D matrix datasets whose columns and rows corresponded to the dimension of the walls. Reduction these 2D datasets to line plots as a function of segment location was obtained by summing the columns of the datasets, similarly to what was done previously for the anticlinal wall [29]. The signal at the isolated anticlinal wall was normalized from 0 to 1 at each time-point to give equal weight to persistence plots and removing the variability of imaging conditions. For the outer-periclinal wall, it was desirable to keep the signal intensity difference between the cells, for that reason the signal was normalized from 0 to 1 based on the maximum and minimum values of the combined cells values. Even with a noisier outcome due to incorporating all the microtubule signal at the outer-periclinal wall, an enrichment at the future apex region was consistent in all lobing segments. As the goal was focused on the lobing regions, this method served as a good proxy to quantify transfacial microtubules at these sites of interest (Fig 4.S3.3). Initially, attempts at measuring local microtubule orientation and organization, here measured as coherency where aligned microtubules would received a score of 1, were not very

informative (Fig 4.S3.4) most likely due to inconsistent imaging conditions. Utilizing the summed microtubule signal provided a way to quantitatively measure the enrichment of the outer-periclinal walls of two neighboring cells which was clearly visible from summed signal projections of these time-lapses prior to the lobe formation (Fig 4.4B). Additionally, this method allowed the capture of microtubule enrichment as function of time at the future lobe apex (Fig 4.4D). When all 11 lobing segments were pooled, there was a clear enrichment of microtubules at the future convex side of the lobe of 148 $\pm$ 109% compared to the concave region at the neighboring cell (Fig 4.4E, Fig 4.S4.1). Most importantly, this enrichment seemed to be independent of the initial segment shape. This is clearly exemplified in one of the segments that had a new symmetry breaking event against the bulging direction already established (Fig 4.S4.2) revealing how these features are active events and not just a consequence from a buckling event as previously claimed [35]. Together, the results from manually scored transfacial microtubules and with the new microtubule persistent method show how the organization of microtubules over time dictate the location and direction of new lobe formation. Additionally, symmetry breaking events in bulging segments show how lobe initiations are active anisotropic expanding features independent of the segment geometry.

4.2.4 Microtubules are patterned by geometry-based cell wall stresses

The results of locally persistent microtubules that predict the location of lobe formation produced the question of what was patterning the microtubules at this location. In previously studies from lobed pavement cells snapshots, a correlation was found with predicted stresses and microtubule organization at the convex side of lobes [35, 53]. To evaluate how cell wall stresses were influencing microtubule organization a 3D model was constructed in the same manner as in Fig 4.1. Since the patterning of stresses are very sensitive to geometry [35] it was necessary to evaluate the stress patterns prior to lobe formation using live cell images of pavement cell

just prior to lobe detection (Fig 4.4 F-H, Fig 4.S4.3 C,G). The predicted cell wall stresses were extracted from both the anticlinal wall and outer-periclinal wall near the anticlinal/periclinal wall junction. The models revealed how the principal stress patter of the cells correlated with microtubule persistence plots for the anticlinal wall showing a clear microtubule persistence peak at a location of high stress (Fig 4.4 I). When the outer-periclinal walls were analyzed, the stress was bias towards the cell that the lobe will expand into (Fig 4.4 J, Fig 4.S4.3 D,H) mirroring the enrichment microtubule at those sites towards the same cell. Together these results suggested how microtubules were responding to cell wall stresses resulting in lobe formation.

4.2.5 Furrows are self-autonomous features of de-coupled lobing cells

The microtubule system is highly dynamic [29] but microtubules over time localized to regions where a new lobe will form which were also regions of predicted high stress. It is still unclear if the microtubules themselves serve as a stress sensor or if an unknown molecular player is responsible. The inability to selectively disrupt the transfacial microtubules, presented a challenging problem. Fortunately, unrelated experiments using the distorted mutant *dis2-1*, which has been shown to have cell adhesion problems [56], produced cell invaginations, from hereafter refer to as furrows (Fig 4.5 B). These features were also visible in the pectin synthesis mutant *qua2-1* (Fig 4.5 A) just as previously shown [45]. Close inspection using an TEM image revealed invaginated cell with two closely appressed cell wall with a highly rounded apex. Importantly, microtubules were clearly seen at the apex of furrows (Fig 4.5 E – yellow arrows). This provided a method to disrupt the cell boundary and test if lobe initiations are a protruding force or an inward directed cell autonomous event. Furrows were induced in the wild-type after extended pectinase treatment (Fig 4.5 C) and reinforcing their dependence of microtubules, addition of the microtubule stabilizing drug paclitaxel, we could see the emergence of very rare opposing furrows (Fig 4.5 D). The ability for neighboring cells to have bidirectional furrows hints that

both cells are capable of undergoing a symmetry breaking event. Furrows were absent when pectinase and either oryzalin or isoxaben were combined (Fig 4.S5.1). This is consistent with of the reduction of lobes with these treatments (Table 4.2). The necessity of an intact pectin, cellulose, and microtubule system for normal morphogenesis suggested that the underlying mechanism behind furrow formation is the same mechanism behind lobe initiation albeit in a partially decoupled cell.

4.2.6 Microtubule are preferentially localized at the apex of nascent furrows

Furrow formations are rare events in pectinase treated seedlings and their location on a cotyledon is hard to predict. Despite these limitations, furrows provide an opportunity to analyze shape change in a semi-isolated cell. Due to their similarity to lobes, it became crucial to test if the microtubule patterning in furrows was consistent to the patterning seen in lobes. The focus was directed towards active features and the study was narrowed to nascent furrows (Fig 4.5 F) instead of mature furrows (Fig 4.5 E). This was done because as stated before, the location of the rare induced furrows is hard to predict and because previous analysis in *qua2-1* seedlings showed that these features formed as narrow local invagination events that progressed from nascent furrows to mature furrows [45]. In high resolution images, the microtubules splay across the anticlinal wall (Fig 4.6 B – insert) and the outer-periclinal wall (Fig 4.5 G) at the apex of nascent furrows. To analyze if the apex was a hot-spot for microtubules, the microtubule signal was plotted as a function of furrow length placing the apex of these highly symmetrical feature at the midpoint of the normalized furrow length (Fig 4.5 I,J). Population level analysis showed that microtubules are preferentially localized to the apex of these features (Fig 4.5 K) and most likely are responsible for their formation and elongation.

4.2.7 Furrow originate at regions of maximal cell wall stress

The preference of microtubules to localize at regions expected to have maximal geometrical-base stresses hints at how microtubules can translate cell wall stresses to cell morphogenesis. Naturally, the question emerged on how the geometric-based stress pattern in pectinase treated cells correlated with the observed location of furrows. Furrow behaviors can be used as a cell shape change proxy to analyze lobe initiation, and how cell shape, cell wall stress, and microtubule organization interact during polarized growth. Utilizing the cell shapes of a cell pair that produced a furrow (Fig 4.6A), a mock pre-furrow FE model was created (Fig 4.6B) using the contour of the neighboring cell (Fig 4.6C). Interestingly, the predictive cell wall stresses varied between the cells and it was maximal and spatially corresponded to the region where the furrow appeared (Fig 4.6D). In straight segments, in agreement with previous models [28, 35, 53] our FE models predicted that the location farther away from 3-way junctions would experience the highest amount of stress and perhaps the patterning force for cell wall deformation. When the location of furrows from relative straight segments were mapped, their appearance was greatly bias towards the center of these segments (Fig 4.6F) indicating that their location was a response to the maximal internal cell wall stress. Concurrently , these cell wall stresses showed high spatial correlation with the shape and curvature of the furrow, indicating how the curvature of the cell was a key factor for cell wall stress (Fig 4.6E) consistence with the population level analysis showing the apex to be a hotspot for microtubules (Fig 4.5K).

Spatial overlap between microtubule organization and predicted stress along the wall suggested that microtubules might be responding to geometrical stress to initiate a symmetry breaking event. The furrow data also provided an opportunity to evaluate spatial correlation between shape, predicted cell wall stress, and microtubule organization. The finite element simulation predicted cell wall stress to be maximum at the apex of (Fig 4.6G), the region of highest curvature of the furrow. Analyzing the

microtubule signal along this segment, a clear microtubule intensity peak localizes to the region of expected cell wall stress (Fig 4.6H). Together, these results support the hypothesis that furrow formation is being driven by microtubule organization which itself is directed by cell wall stresses.

4.3 Discussion

The complexity of epidermal tissue morphogenesis can be exemplified by the interdigitated phenotype of its most prevalent cell type. How this drastic shape change from a simple polyhedral cell is initiated remains unknown. Here, the goal was to test two main hypotheses, is shape sufficient to pattern the morphogenesis of pavement cell and to evaluate if microfibril deposition directed by microtubule organization is the patterning mechanism for lobe formation. Lobes emerge following symmetry breaking are subtle changes along the cell periphery that requires high spatial- and temporal-resolution. Previously, using a plasma-membrane marker, allowed for the detection of lobes which can be identified by a stable small ∼300nm deflection [29] which was never detected along the flanks of existing lobes. Building on this technique, stable makers along the anticlinal wall by the genetically encoded PDLP3:GFP allowed the sub-segmental mapping of growth rates along the cell periphery (Fig 4.1). The lack of correlation of growth rates with either predicted stress patterns or sub-segmental shape implies that the wall must be have differential mechanical properties. There have been two recent reports that pectin is involved in generating the cell wall asymmetry that controls lobe initiation. In one, de-esterified pectin deposition at the convex side of established lobes [35] was claimed to drive lobe initiation. However, robust localization of pectin along the segment and mutant analysis is necessary to test this result. Along similar lines, super-resolution imaging identified perpendicular methylesterified pectin nanofibers in the anticlinal walls of lobed pavement cells [36]. The same reservations from Bidhendi et al., 2019 [35] apply to this study and further analyses are still necessary. It is not known if the patterns on these studies

emerge prior to lobe formation or if the patterns are the results on the segment shape change. Without time-lapse data or evaluation of unlobed cells this question cannot be answered.

In this study true mechanism of lobe formation is revealed. Pharmacological and genetic data (Fig. 4.2, Tables 4.1,4.2), showing a clear reduced cell shape phenotype, presented the microtubule system as a good candidate for analysis of its dynamic behavior paired with our coordinate system for lobe detection. The exact microtubule behaviors that underlie lobe initiation is difficult to discover. Initially, local analysis of microtubules orientation and coherency was conducted at opposing regions across a lobing region but provided little supporting information (Fig 4.S3.4) with highly variable values which are very sensitive to image quality. However, microtubule signal sum projections of the segments prior to lobe detection revealed clear signs of cortical microtubule enrichment at lobing locations (Fig. 4.4 A, Fig 4.S3.4 A,E). Furthermore, montaged images of the anticlinal and outer-periclinal wall revealed that a subset of microtubules splays across these walls and that their localization over time was biased toward regions where new lobe initiation would form (Fig. 4.3). Finite element modeling of cell shapes prior to lobe detection showed that the persistence of these microtubules colocalized to regions of predicted high stress (Fig. 4.4 J, Fig 4.S4.3 D,H). Taken together these results suggest a morphogenic system based on transfacial microtubule whose localization is cell wall stress dependent. While cellulose was clearly microtubule directed during this timeframe (Fig. 4.S2.1), direct testing of anisotropic patches could not be done due to the lack of transfacial microtubule targeted depolymerization. Partial degradation of pectin promoted the invagination of the cell wall and expose the cell autonomous mechanism of shape change. Cell adhesion mutants *qua1-1* [45] and *qua2-1* (this study) form rare furrowing features. Time-lapse analysis of these furrows indicates that the invaginations become progressively longer rather than representing a region of growth repression [45] and it suggested that they might use the same mechanism as lobe formation. Induced furrowing with pectinase treatment on wild-type seedlings was blocked when the microtubule or cellulose systems

were disrupted using oryzalin and isoxaben respectively (Fig 4.S5.1) showing high similarity to the lobe blocking effects of these drugs in intact tissue (Table 4.2). Interestingly, microtubule stabilization using paclitaxel would in very rare occasions produce opposing furrows in neighboring cells (Fig 4.5 D) suggesting that both cells have the ability to produce a lobe. The location where these furrows emerged was of high interest as they could elucidate the patterning mechanism of shape change. Population level analysis of furrow location on straight segments showed a bias at the region further away from 3-way junctions (Fig 4.6) a region of high predicted cell wall stress [28]. Within the furrow, microtubules were highly localized to the apex of the feature (Fig 4.5 K) and similarly to lobing regions they transverse the anticlinal and outer-periclinal walls (Fig 4.5 G, insert). The localization of microtubules to regions of high stress in furrows (Fig 4.6 H) and their narrow extension after they are formed supports the localized anisotropic expansion of lobes. Together both of these systems propose a mechanism where microtubules localized at regions of high cell wall stresses serve as tracks for cellulose deposition. The localized cellulose deposition produces patches of anisotropic expansion leading to symmetry breaking events be it lobe or furrow initiation (Fig 4.7).

4.3.1 Future directions

Here, local correlative analysis of cell wall stresses, shape change, and microtubule localization has been presented proposing the key role of microtubules in translating cell wall stresses to cellular morphogenesis. However, further analysis is required to elucidate if the shape change that occurs in pavement cells promotes anisotropic organ expansion or if lobe formation is a buffering mechanism for differential epidermal cell expansion. The results shown here propose a high cell wall stress responsive mechanism rather than a patterning mechanism for anisotropic organ expansion. However, to carefully evaluate this, organ level analysis is necessary to track how pavement cells expand in the context of organ level growth. Mapping organ level expansion,

predicted cell wall stresses, and cellular morphogenesis in long-term time-lapses can elucidate if lobe formations are a consequence or the driving force behind organ morphogenesis.

4.4 Materials and methods

4.4.1 Plant Material and Growth Conditions

Arabidopsis thaliana seedlings were grown at 22°C on $\frac{1}{2}$-strength Murashige and Skoog medium with 1 % Sucrose (w/v) and 0.8% (w/v) Bacto-agar under continuous illumination. For the chemical treatment; the seeds were transferred and completely submerged in liquid media, which omits the Bacto-agar, after germination under continuous illumination with the respective treatment. For low-light chemical treatment, the seedlings were grown until 1 DAG and then transferred to plates with the chemical compound dissolved onto the media which were placed vertically on (5 μmol m^{-2} sec^{-1}) at room temperature. Arabidopsis ecotype Columbia-0 was used as the wild type. Mutants lines were described previously: *bpp1;2;5* [34], *tubg1-1;2-2* [57], *any1* [11], *qua2-1* [40], *exo84b1* [58], *clasp1* [18], *ktn1-2* [59], *dis2* [60], *zwi3* [61]. PDLP3::PDLP3:GFP [62] was crossed to PIP2:mCherry line [63]. PIP2:mCherry; TuB6:GFP was previously described [29].

4.4.2 Imaging and Analysis of Cotyledon Pavement Cell Shape: Population-Level studies

Whole seedlings were stained using FM4-64 (1 μM) for 30 min. Cotyledons were dissected and imaged using a Vaseline chamber sliced and imaged Bio-Rad 2100 laser-scanning confocal microscope mounted on a Nikon Eclipse E800 stand. Samples were excited with a 488-nm laser, and the fluorescence signal was collected using a 490-nm long-pass dichroic and a 500- to 550-nm band-pass emission filter using a 20x 0.5 NA objective. Image fields were obtained from the apical 1/3 of the cotyledon.

Representative complete pavement cells not part of the stomata cell linage was traced manually using the polygon tool in Fiji and the traces were splined using the line-tool option. Pavement cell traces were analyzed using LobeFinder [46] and statistical analyzes were done in R.

4.4.3 Subsegmental growth rate analysis

Confocal Microscopy and Time-lapse Imaging of Lobe Initiation. 1.5-DAG whole seedlings were mounted in our in-house long-term chamber system as previously described [24]. Confocal fluorescence microscope was performed using a 100x Plan-APO 1.46 NA oil-immersion objective and images were acquired using a spinning disk CSU-10 confocal head (Yokogawa Electric) mounted on a Zeiss Oberver.Z1 inverted microscope controlled using Slidebook software (Intelligent Imaging Innovation). GFP and mCherry were excited by 488- and 561-nm laser lines respectively. Approximately 10-min sequential image acquisition was performed for microtubule and plasma-membrane time-lapses and 0.5-or-1 hourly for plasma-membrane and PDLP time-lapses using an Evolve 512 camera (Photometrics) through band-pass filters (482/35 and 617/73; Semrock).

Imaging of delamination and furrows after pectinase treatment

mCherry was excited by the 561nm laser line through bandpass filters described above. For low-light chemical treatment; 6-8 image fields at the basal region of the cotyledon were collected using the 60x C-Apo 1.2 NA water immersion objective. Images were acquired using the Evolve 512 camera. For submerged chemical treatment; 2 DAG whole seedlings were imaged completely using the 20x Plan-APO 0.8 NA objective using the montage method in Slidebook then the image stacks were merged to obtain an 3D montaged imaged. Images were acquired using a Prime 95B camera (Photometrics).

4.4.4 Analysis of Sub-segmental growth rates

Segments with at least 1 PDLP were identified and the 3-way-junctions were manually tagged using a 3-by-3 pixel square 1.5 μm below the 3-way-junction for 2 image slices. Using the plasma-membrane, cell boundaries spanning from slightly passed the three-way junction were segmented manually using the segmented line tool with the spline function activated in FIJI and saved as an ROI. After all time-points were collected the ROI series were saved as an ".zip" file. The macro PDLP.ijm, which acts on both the plasma-membrane and PDLP channels at each time-point, straightens the segment, re-slices the straighten segment, and then a max-projected image is produced. To reduce the tilt due to sample or mounting, one time-point was aligned to the x-axis using the 3-way-junction marks and the rest of the time-points were aligned to it using the resliceAlignement.ijm that worked on lines drawn from 3WJ to 3-way-junction. PDLPs were tracked using the Particle Tracker 2D/3D tool from the MOSAIC imaging toolset [64]. Non-overlapping PDLPs at least 2μm apart were used to calculate pair-wise distance as a function of time and a linear-fitted to obtain the sub-segmental growth rate, if the total displacement was less than image resolution then a growth rate of zero was awarded. To verify the outputs, the sub-segmental growth displacement was summed and evaluated to the displacement from the 3-way-juncions. If the value was less than 3% error, then the measurements were accepted.

4.4.5 Finite element model

Stress field analysis in the pavement cell walls was studied using commercial finite element (FE) software Abaqus. The structural model of the cells was based on the segmented cell wall boundary and surrounding anticlinal wall. All the cells were divided by a middle lamellar layer of pectin. The model before application of turgor pressure consisted of a flat periclinal wall bonded to the anticlinal walls. The thickness of the periclinal and anticlinal walls was 300 and 35 nm, respectively. All cells were

surrounded with pectin to approximate the confinement of adjacent cells. The turgor pressure in each cell was set to 0.6 MPa. The material for all cells was assumed to be a neo-Hookean, hyperelastic isotropic material assigned uniformly across the model. The elastic modulus was assumed as 600 MPa with a Poisson's ratio of 0.47. The whole material was assumed to be a standard linear solid with a primary relaxation time of 6.8 s with a ratio of infinite modulus to the total elastic modulus of 0.85 [65]. The middle lamellar pectin was assumed to have the same properties as the surrounding pectin with an elastic modulus of 100 MPa [66]. For all pairs of segmented cells, after 20 s of pressurization and sufficient relaxation, the stress field in the cell wall was used for analysis. For the five cells model of the sub-segmental growth rate, after the first step of 20 s pressurization, the deformed structural model at the end of the first step was used as the initial structure in the second step and was pressurized for another 20 s, and then the stress field in the walls at the end of second step was used for analysis.

4.4.6 Anticlinal wall tilt analysis

Segment shapes were traced as explained above. Lobes detection and their location were identified by using the find_peaks, peaks_prominences modules in python restricted to features greater than 286 nm as previously described [29]. To get the local tilt at apex as a function of lobe formation; the relative position of the lobe in a length normalized segment was used for its position prior to the lobe detection. A re-slice of the anticlinal wall at the apex was traced using the segmented line tool in Fiji for a time-point prior to lobe detection, at detection, and at least one time-point after detection. The traces were analyzed by first rotating it to the y-axis then measuring its width giving a score of zero to widths smaller than the imaging resolution. To measure the tilt along the segments, the segments were straighten then re-sliced along the x-axis to get the cross-section of the anticlinal wall. The OrientationJ Dominant Direction plug-in was used to obtain the tilt along the segment.

4.4.7 Microtubule persistence at the anticlinal and outer-periclinal wall for neighboring cells

Using segment traces as described above. The zip file for a segment's time-series was run through the imageTextOfMTWalls.ijm macro which allows the extraction of the microtubule signal from the anticlinal and outer-periclinal wall. For each time-point, the segment was straighten, re-sliced, and a SUM projected image was created of the plasma-membrane which allows the user to create a bounding box that defines the extent of the anticlinal wall on the image stack. This information is propagated to the microtubule channel to obtain a text image of the outer-periclinal wall for each cell after a MAX intensity projection and a text image of the anticlinal wall after SUM projection of 6 image slides from the image stack center and are saved in their respective folders. To create the persistence peaks of microtubules, the python code; createAnticlinalAndOuterPericlinalPersistenceMaps.py is executed. This requires information about which cell is the initiating cell, what time-point the lobe is detected, the location of the lobe at detection, and the width of the lobe apex at detection. For each time-point, using the three matrices produced by imageTextOfMTWalls.ijm, 1 for anticlinal wall and one for outer-periclinal wall for each neighboring cell, the columns are summed to obtain a one-dimensional value for each cell face. The values for the anticlinal wall are normalized from zero to one using the equation:

$$normValue_i = \frac{value_i - min(array)}{max(array) - min(array)}$$

For the periclinal wall, the values are normalized from zero to one from using the maxima and minima of both datasets combined. Stacks-plots are created using the normalized value for the timepoints before lobe initiation, after lobe initiation and for the whole time-lapse. For enrichment, first; the area the area under the curve of the accumulated plot that spans the width of the apex centered at the location

of first detection using the trapezoid method for the initial and following cells. The enrichment is calculated using the following equation:

$$Enrichement = -1 + \frac{Area_{cell1}}{Area_{cell2}} * 100$$

This is also done at each time-point individually to obtain the enrichment at each time-point.

4.4.8 Microtubule orientation and coherency analysis

Segment of interest were aligned to the first time-point by drawing a line across its 3-way-junctions and saving them as ROIs. The regIndSegWith3WJLines.ijm macro is then run selecting the max-projected images, ROI zip file location, and output folder. The location of a new lobe is then identified as explained above and two ROIs 2-by-2 μm were placed across the anticlinal wall at the location where a new lobe will form. The OrientationJ Dominant Direction plug-in was used to obtain the orientation and coherency of microtubules.

4.4.9 Manual transfacial microtubule scoring

Text image outputs from imageTextOfMTWalls.ijm were imported into Fiji and converted to RGB color. In order to observe which bundles were transfacial, it was necessary to combine the anticlinal and outer periclinal wall images using the combine tool in Fiji. The images were combined vertically with the anticlinal wall positioned directly below the outer periclinal wall that corresponded to the same time point. This was done for both cells both sharing the anticlinal wall. Transfacial microtubule bundles were then scored by marking them in the middle of the bundle. Only clear, distinct transfacial microtubule bundles were scored which we defined as microtubules that directly connected from the anticlinal wall into the outer periclinal wall. These bundles appear as a continuous, vertical line of high intensity pixels in the combined image. The pixel locations for all marked transfacial microtubule bundles, along with

the pixel width of the entire image, were recorded in order to generate normalized segment length histograms. A density curve was obtained using these values. To match the y-value range to the histogram, the density values were multiplied by the proportional difference between the max value of the density plot and the maximal value of the histogram graph.

4.4.10 Microtubule organization within furrows and furrow position on straight segments

Nascent furrows were traced to and from regions where the anticlinal wall separated. For each furrow, the microtubule intensity was measured at the anticlinal wall and then normalized the signal from 0 to 1. The length of each furrow was normalized from 0 to 1. A stack-plot was constructed of the normalized signal to obtain a population level plot of microtubule preference within a furrow. Furrow normalized peak location was obtained from otherwise straight segments and histogram was created using R.

4.5 Tables

Table 4.1. The microtubule, pectin, and cellulose systems are key for normal pavement cell morphogenesis in fully expanded cotyledons.

		Area (μm^2)	Circularity	Lobe Number	LpA*1K
Genotype	N	Mean ± S.D	Mean ± S.D	Mean ± S.D	Mean ± S.D
WT	30	10111 ± 4641	0.26 ± 0.09	16 ± 4	1.81 ± 0.55
tubg1-1;tubg2-2	25	6377 ± 2289 *	0.18 ± 0.06 *	19 ± 5 *	3.22 ± 0.71*
any1	38	10741 ± 3190	0.59 ± 0.10 *	8 ± 2 *	0.84 ± 0.27*
qua2-1	26	3281 ± 1932 *	0.55 ± 0.01 *	10 ± 2 *	3.81 ± 1.48*
exo84b1	23	10746 ± 5138	0.17 ± 0.07 *	21 ± 6 *	2.18 ± 0.67*
clasp1	20	10619 ± 4032	0.33 ± 0.06 *	16 ± 3	1.68 ± 0.48
ktn1-2	22	9249 ± 4480	0.34 ± 0.09 *	16 ± 2	2.05 ± 0.70
zwi3	24	11264 ± 5316	0.18 ± 0.08 *	20 ± 6 *	1.97 ± 0.57
WT @ 31˚C	20	4518 ± 1311 *	0.26 ± 0.07	16 ± 3	3.61 ± 0.79
mor1-1 @ 21˚C	13	5274 ± 1900 *	0.33 ± 0.07 *	16 ± 4	3.32 ± 0.86
mor1-1 @ 31˚C	23	3764 ± 994 ◊	0.68 ± 0.1 ◊	10 ± 2 ◊	2.77 ± 0.81◊

*Significant satistical difference betweeen the null mutant and WT at 21˚C *, WT at 31˚C ◊ by Wilcox-Whitney test (p<0.05)*

Table 4.2. Disruption of the pectinase and cellulose or microtubule system blocks lobe initiation

DAG	Treatment	Area (μm^2) Mean ± SD	Lobe # Mean ± SD
1	NT	634 ± 163	7 ± 2
2	NT	1454 ± 484	11 ± 2
	DMSO	1717 ± 531▲▼	12 ± 2▲
	Oryzalin	1852 ± 533▲▼	8 ± 2▲▼
	Isoxaben	1450 ± 443▲	9 ± 2▲▼
	Pectinase	1332 ± 334▲	11 ± 2▲
	Pectinase + Oryzalin	941 ± 205▲▼	7 ± 1 ▼
	Pectinase + Isoxaben	818 ± 222▲▼	7 ± 2 ▼

▲Statistical difference between treatment and 1DAG

▼Statistical difference between treatment and 2DAG

4.6 Figures

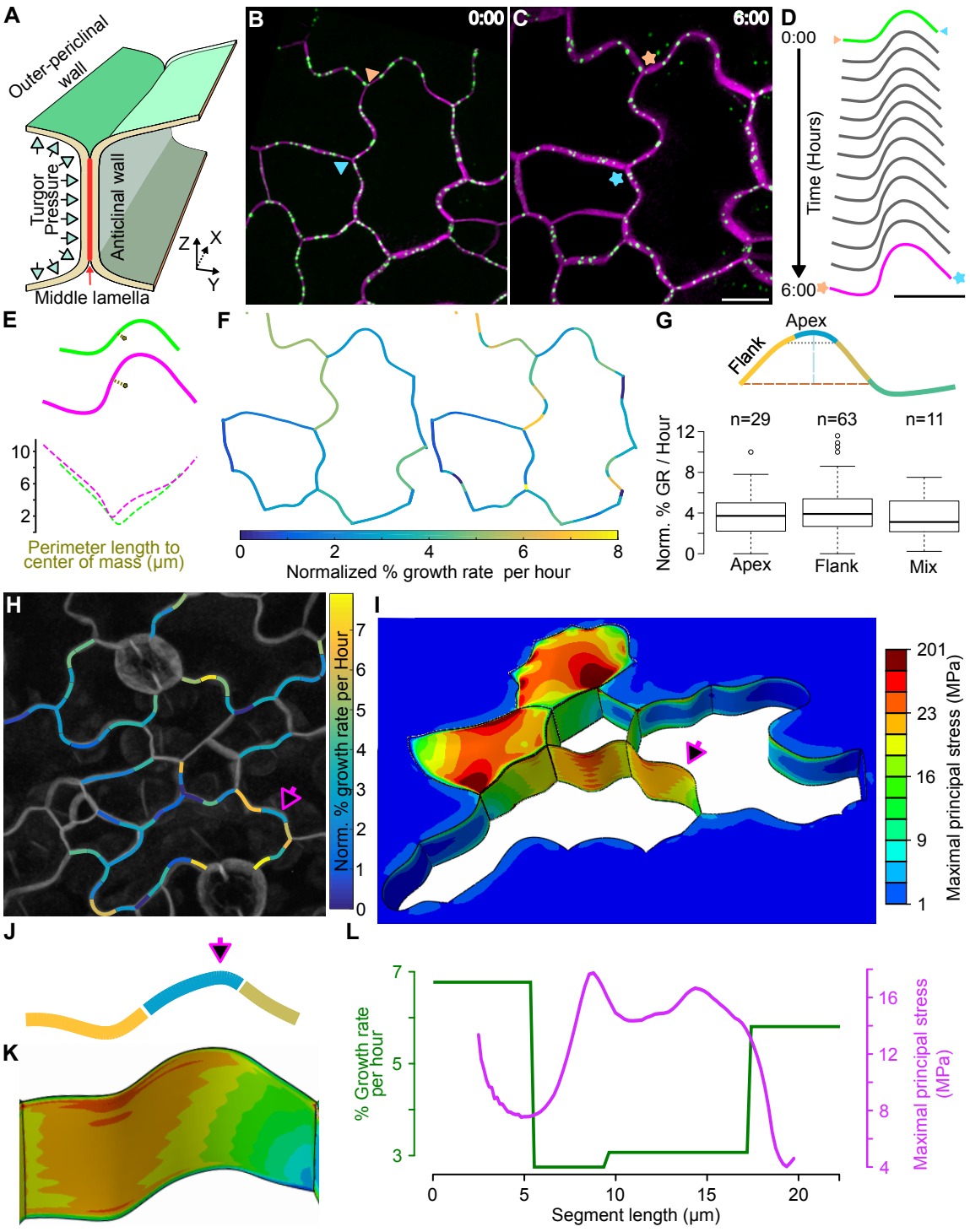
A
Outer-periclinal wall
Turgor Pressure
Anticlinal wall
Middle lamella
Z
X
Y
B
0:00
C
6:00
D
0:00
Time (Hours)
6:00
E
10
6
2
Perimeter length to center of mass (µm)
F
0
2
4
6
8
Normalized % growth rate per hour
G
Apex
Flank
n=29
n=63
n=11
Norm. % GR / Hour
12
8
4
0
Apex
Flank
Mix
H
Norm. % growth rate per Hour
7
6
5
4
3
2
1
0
I
201
23
16
9
1
Maximal principal stress (MPa)
J
K
L
% Growth rate per hour
7
5
3
0
5
10
15
20
Segment length (µm)
16
12
8
4
Maximal principal stress (MPa)

Fig. 4.1. Segment geometry is insufficient to predict growth rates in expanding pavement cells. (A) Illustration of interface between pavement cells in a cross-section view. Wall nomenclature and coordinate system for image data are shown. (B-C) Snapshot of pavement cell time-lapse of plasma membrane (magenta) and PDLP3 (green). Example segment, triangles t=0, stars t=6 hr. (D) Shape change of a segment over time between vertices shown in (B,C) color coded triangles and stars indicate the directionality of the segment. (E) Distance from segment outline to center of mass were obtained to analyze the pattern of shape change at the extreme time points. Dashed lines are the color coded to match the time points. (F) Whole segment strain rates calculated using 3-way junctions (left). Subsegment strain rates calculated from the displacement of genetically encoded fiducial marks (right). (G) Population level analysis of subsegment strain rates as a function of their location on a lobe. (H) Heat map of subsegment strain rates in a field of cells. (I) Finite element model was constructed to evaluate the relationship between sub-segmental growth patterns (J) and predicted stresses along the segment (K) showing a disconnect between these two parameters (L). Scale bar = 10 μm.

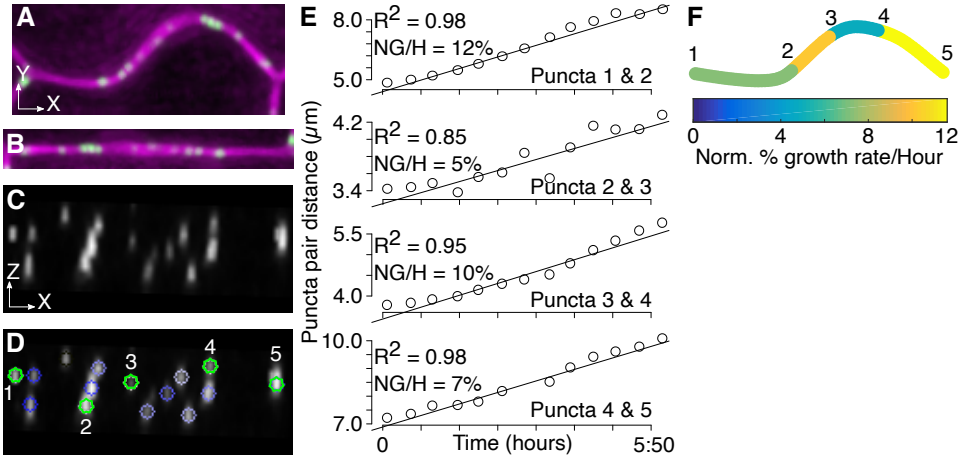

Fig. 4.S1.1. Particle tracking of PDLPs allows for an efficient way to measure sub-segmental growth rates. (A) Segments were traced at the anticlinal/outer-periclinal junction, straighten (B) and resliced to obtain a face-on view of the anticlinal wall (C). (D) Non-overlapping PDLPs, including manually labeled 3-way-junctions were tracked over time to obtain average growth rates between PDLP pairs over the time course. (E) Example linear-fitted plots of the PDLP pairs that were mapped back to the cell segment (F).

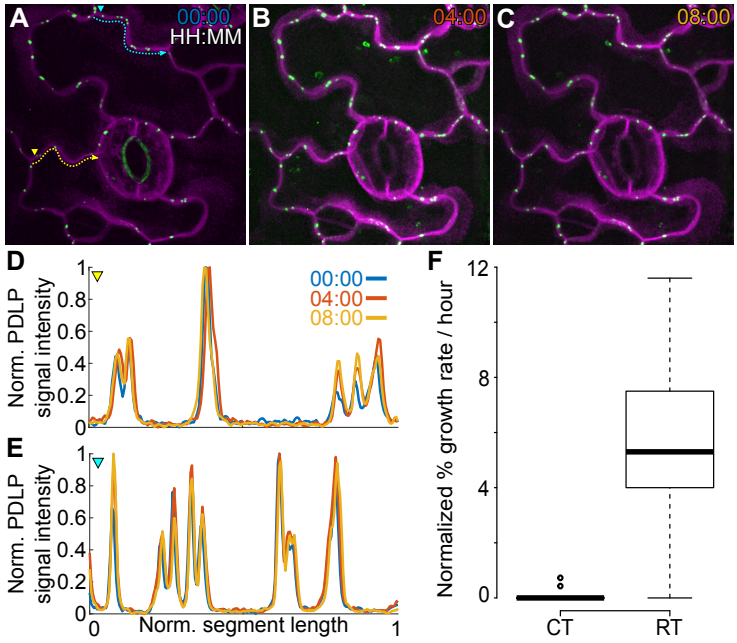

Fig. 4.S1.2. PDLPs are stable features in the anticlinal wall, and their displacement is growth dependent. (A-C) Cold-treated seedlings were imaged at a 4-hour interval. (D-E) Signal intensity plots of segments shown on (A) show tight peak overlap over the time-course. (F) The growth rate per hour of subsegments were dramatically lower compared to its room temperature counterpart showing that the PDLP movement is directly linked to the growth of the cells.

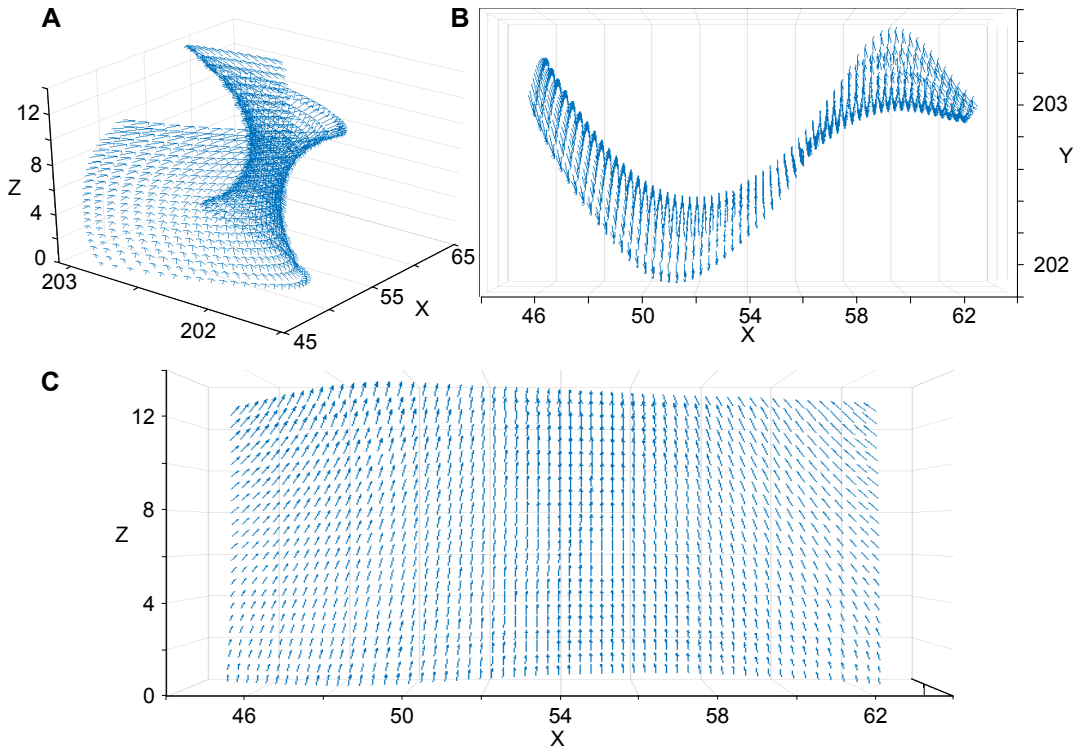

Fig. 4.S1.3. The maximal principal stresses in the anticlinal wall are in plane and perpendicular to the leaf surface. Arrows reflect the magnitude and direction of the stresses. (A) Orthographic projection of representative segment; showing how the maximal principal stresses are perpendicular to the leaf surface pointing towards the outer-periclinal wall. (B) Top-down view of the same segment highlighting its shape. (C) Face-on view of the segment anticlinal wall in the same x-z plane orientation, stress tensors are strongly oriented.

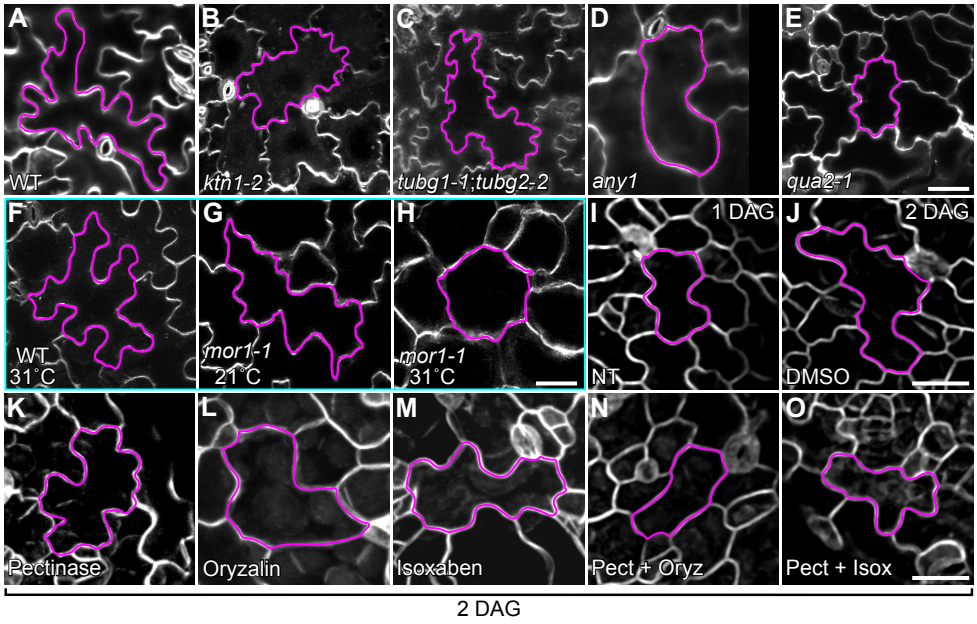

Fig. 4.2. The microtubule, pectin, and cellulose systems are required for normal tissue morphogenesis. Example images cotyledon pavement cells at 10 DAG (A) Wild-type, (B) *ktn1-2*, (C) *tubg1-1;tubg2-2*, (D) *any1*, (E) and *qua2-1*. The temperature sensitive *mor1-1* allele was grown at permissive (G) and restrictive temperatures (H). (I-O) Analysis of lobe initiation rates from 1 to 2 DAG in control and inhibitor-treated seedlings. (I) Wild-type pavement cells at 1 DAG. (J) Buffer-treated control cells at 2 DAG. (K) 0.2% pectinase treated; (L) 10 μM oryzalin; (M) 5nM isoxaben. (N) Combination of 0.2% pectinase and 1 μM oryzalin; (O) 0.2% pectinase and 5 nM isoxaben. Scale bar = 50 μm (A-H), 25 μm (I-O).

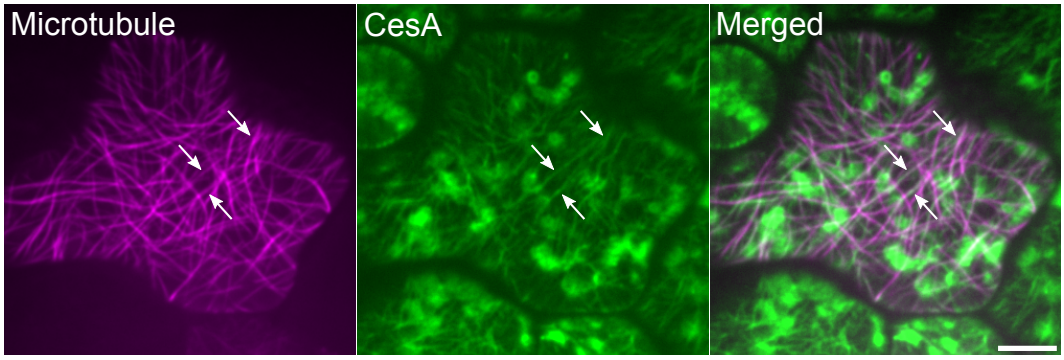

Fig. 4.S2.1. Cellulose synthase complexes strongly colocalize with cortical microtubules in fields of cells in which lobe formation is permissive. 8 min time-lapse projection of 15 sec intervals in a single image plane in the double-marked strain TuA5:mCherry (left panel); CESA6:YFP (center panel) ; CesA6 and microtubule co-localized throughout the cell cortex in the merged image (right panel). Scale bar = 5 μm.

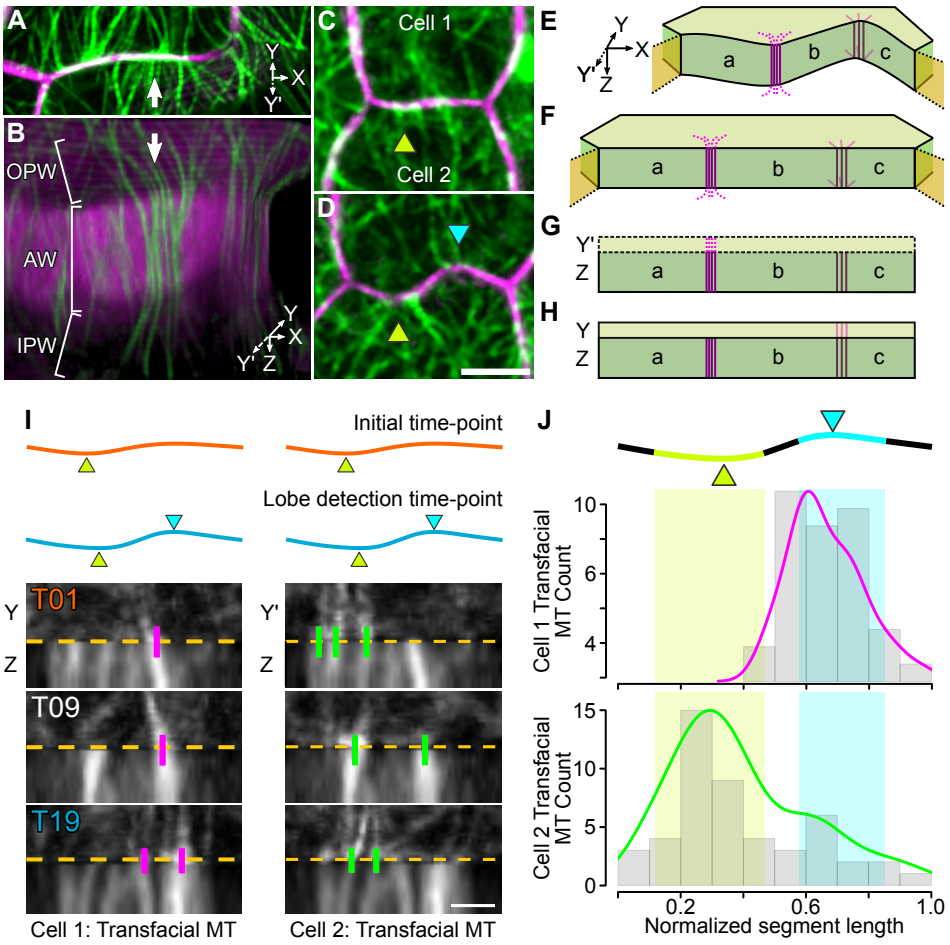

Fig. 4.3. Transfacial microtubules predict the location and directionality of lobe initiation events. (A) Top-down view of plasma-membrane (magenta) and microtubules (green) in a 3D- rendered image. Y and Y' refer to the two periclinal walls at the cell interface. (B) Cortical microtubule bundles span the anticlinal, inner-, and outer-periclinal walls (IPW and OPW respectively). (C) Initial and (D) final time-point of a segment that has undergone a lobe formation event (cyan arrowhead) an existing lobe is marked with a yellow arrowhead. (E-H) Summary of image processing for microtubule analysis (see methods for further details). (E) Curved segment containing opposing periclinal wall domains and the anticlinal wall is straightened to generate (F). (G) The outer periclinal wall in the Y-direction is projected above the anticlinal wall. (H) The outer periclinal wall in the Y'-direction is projected above the same anticlinal wall. (I) Time series analysis of cell shape and cortical microtubules. Upper, examples of a lobing segment showing its shape at the initial time-point and at the time of lobe detection. Lower, montage images constructed as shown above. Example transfacial microtubules at the start of the time-point (T01, orange), an intermediate time-point (T09, white), and at lobe detection (T19, cyan). (J) Manual scoring of the locations of all transfacial microtubules prior to lobe detection. Local enrichments are present where the lobe will be detected (blue arrowheads) in cell 1 (upper panel) and in the convex region of the existing feature (yellow arrowheads) of cell 2 (lower panel). Shaded regions are the lobe widths at 1/2 lobe height (I - cyan curve). Scale bar = 5 μm (C-D); 2 μm (I).

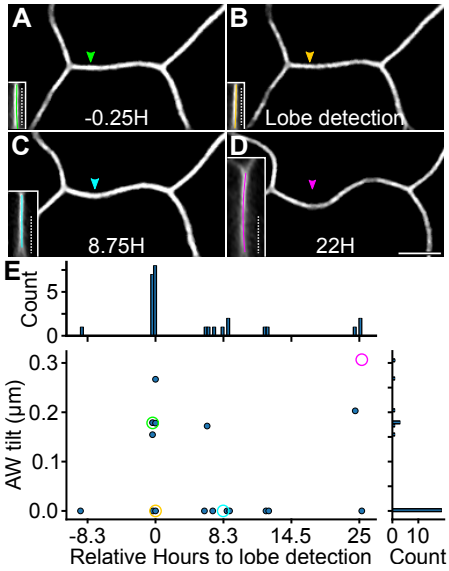

Fig. 4.S3.1. The anticlinal wall at the apex of emerging lobes remain perpendicular to the leaf surface during lobe formation. (A-D) Cross-section tilt analysis of the anticlinal wall at the apex of the emerging lobe over time shows that the wall does not tilt (measured as the bounding box width of the anticlinal wall when its endpoints are placed on the y-axis) locally during this period of expansion (E). Histograms on x- and y-axis are the distribution of the scatterplot based on time and tilt respectively.

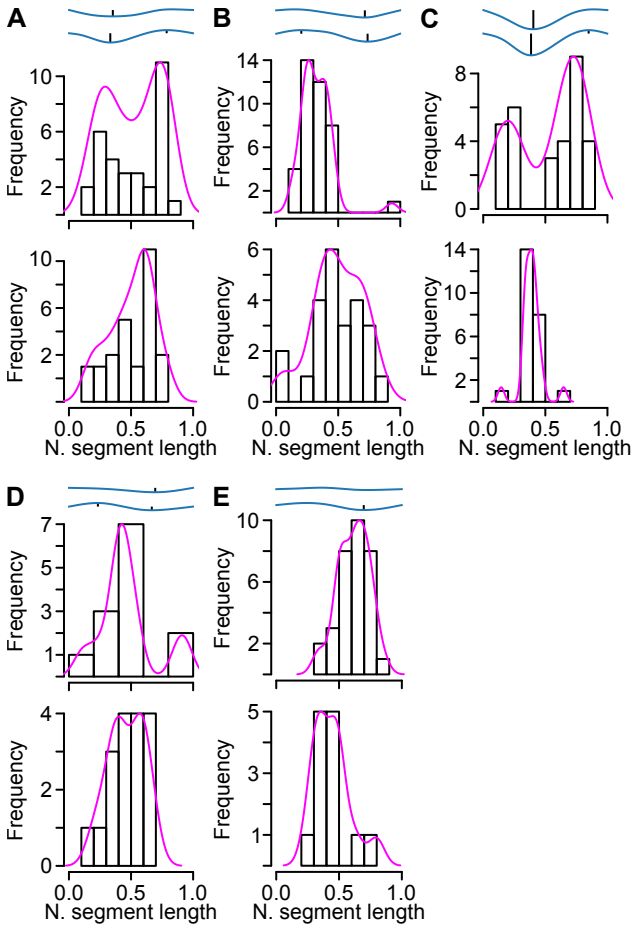

Fig. 4.S3.2. Additional examples of transfacial microtubules predicting lobe initiation. (A-E) Manually scored transfacial microtubules; on each, the top outline is the segment shape prior to lobe detection, below it is the segment shape after lobe detection. Top histogram are the counts for the transfacial microtubules of the cell unto which the lobe will expand and beneath it is the histogram for the neighboring cell.

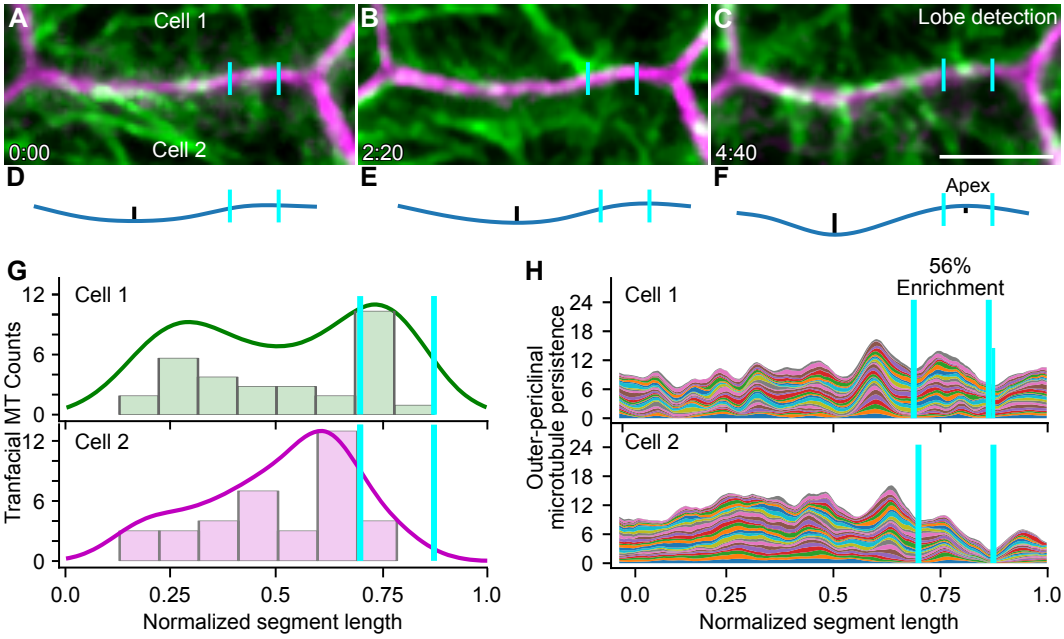

Fig. 4.S3.3. Semi-automated microtubule persistence analysis can detect the local enrichment at the future lobe apex. (A-C) Time-lapsed images the plasma membrane and microtubules of a lobing segment that was captured for > 4 hours prior to lobe detection. (D-F) Outline of the segment shape for the segment corresponding to the live-cell images above where the apex of the new lobe is between the vertical cyan lines, lobes are marked by a black vertical line. (G) Density plot of manually scored transfacial microtubules where cell 1 has a peak at the apex of the new lobe prior to its detection. (H) The persistence method returns a microtubule enrichment at the apex of cell 1. Scale bar $= 5$ μm.

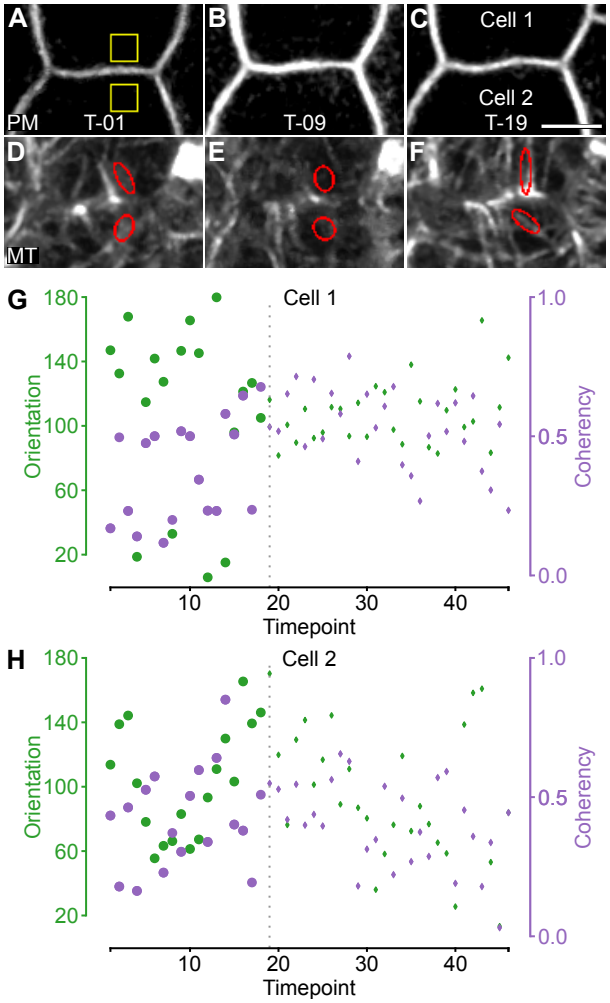

Fig. 4.S3.4. Microtubule organization in the opposing periclinal cell cortex is highly dynamic and disorganized. (A-C) Snapshots of lobing segment prior to lobe formation with local analysis of microtubules at sites across the anticlinal wall where the lobe apex will appear (D-F). (G-H) Both the orientation and coherency fluctuate prior to lobe detection (vertical dotted line) for both neighboring cells. Scale bar = 5 μm.

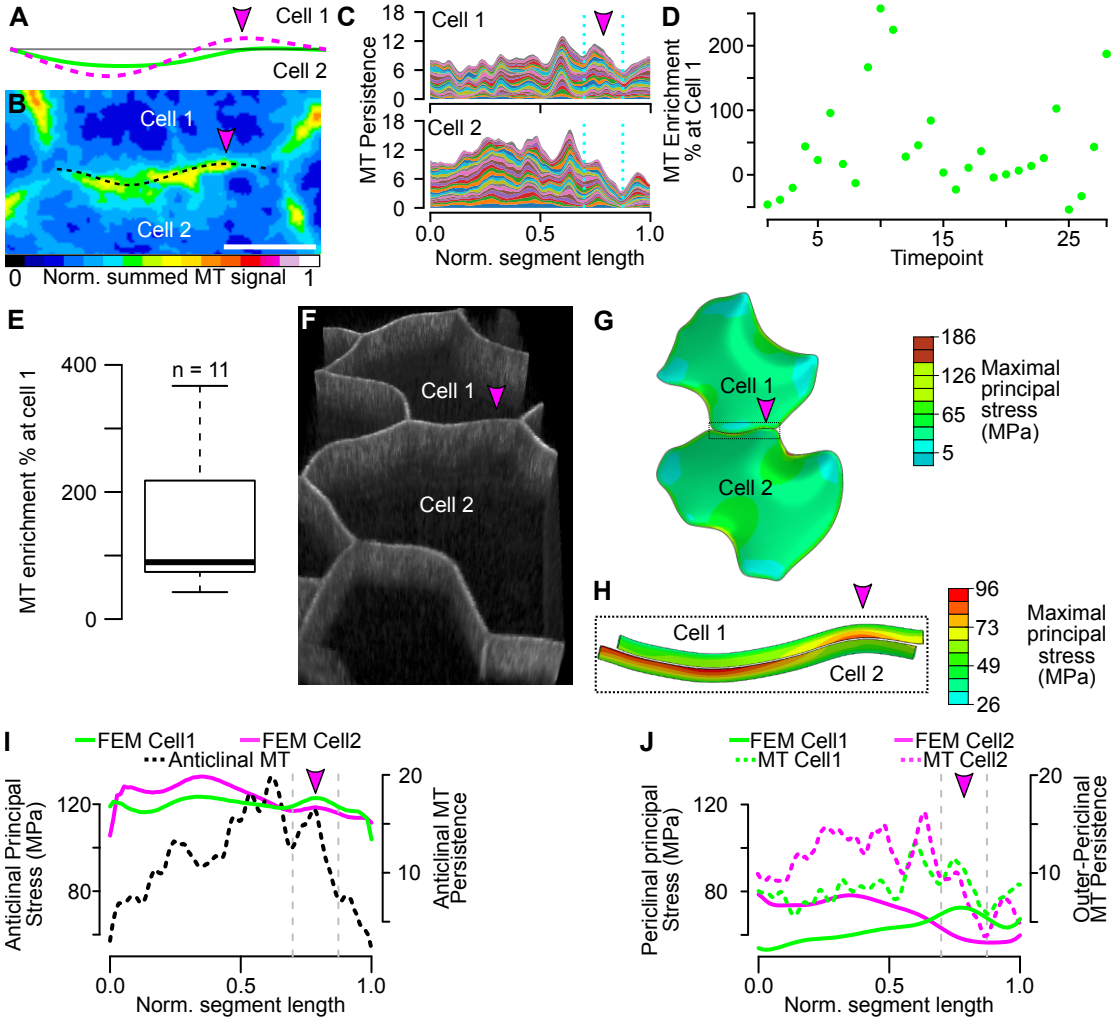
A
Cell 1
Cell 2
B
Cell 1
Cell 2
0 Norm. summed MT signal 1
C
Cell 1
Cell 2
MT Persistence
18
12
6
0
0.0
0.5
1.0
Norm. segment length
D
MT Enrichment % at Cell 1
200
100
0
5
15
25
Timepoint
E
MT enrichment % at cell 1
400
200
0
n = 11
F
Cell 1
Cell 2
G
Cell 1
Cell 2
186
126
65
5
Maximal principal stress (MPa)
H
Cell 1
Cell 2
96
73
49
26
Maximal principal stress (MPa)
I
FEM Cell1
FEM Cell2
Anticlinal MT
Anticlinal Principal Stress (MPa)
120
80
20
10
Anticlinal MT Persistence
0.0
0.5
1.0
Norm. segment length
J
FEM Cell1
FEM Cell2
MT Cell1
MT Cell2
Periclinal principal Stress (MPa)
120
80
20
10
Outer-Periclinal MT Persistence
0.0
0.5
1.0
Norm. segment length

Fig. 4.4. Increased microtubules persistence at lobe initiation sites correlates with local cell domains of increased cell wall tensile stress. (A) Segment shape outline at the start of the time-lapse (green) and at time of lobe detection (dashed – magenta) that is used for the analysis on (C-D, F-J). (B) Summed projection of time-lapsed microtubule signal shows hotspots at regions where a new lobe will form (Magenta arrowhead). (C) Microtubule persistence plots show an enrichment of microtubules for cell 1 at the future convex region of the emerging lobe (dashed – cyan lines). (D) Microtubule enrichment plotted as the percent enrichment of cell 1 (future convex) to cell 2 (future concave) as function of time. (E) Population level analysis of the percent enrichment of periclinal signal in future convex lobes, n = 11 lobing segments analyzed prior to lobe initiation. (F) 3D rendering of cell pair used to construct a FE model of lobing cell interface. (G) FE model predicted stress patterns. (H) Stress patterns of the anticlinal walls of each cell and the periclinal walls of each cell near the anticlinal and outer-periclinal wall junction were extracted. (I) Correlation analysis of anticlinal cell wall stress of the convex lobing cell 1 (green) and the concave lobing cell 2 (magenta) and anticlinal microtubule persistence (black dashed line) as a function of location along the cell segment. (J) Correlation analysis of periclinal cell wall stress (green) and periclinal microtubule persistence (green-dashed) of future convex cell 1. Correlation analysis of periclinal cell wall stress (magenta) and periclinal microtubule persistence (magenta-dashed) of future concave cell 2. Scale bar = 5 μm.

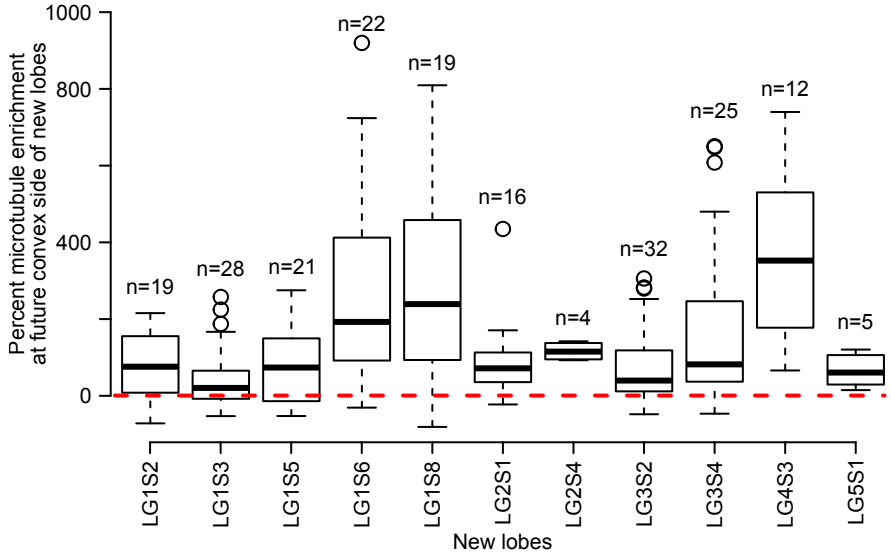

Fig. 4.S4.1. Summary of periclinal microtubule enrichment predicting the location of lobe formation in eleven independent lobing events. Boxplots show the enrichment distribution of individual lobes at the apex prior to its detection. The number of time-points analyzed per lobe are noted above each boxplot.

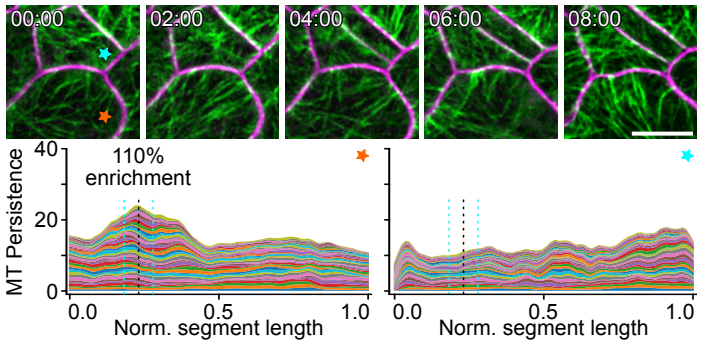

Fig. 4.S4.2. Symmetry breaking events are not restricted by existing segment shape. (Top-row) Eight-hour time-lapse snapshots of a segment that has a symmetry breaking event going against the bulging shape of the segment. (Bottom-row) Microtubule persistence plots at the new feature apex shows an enrichment of microtubule of the bottom cell compared to its neighbor at the same location. Scale bar = 10 μm.

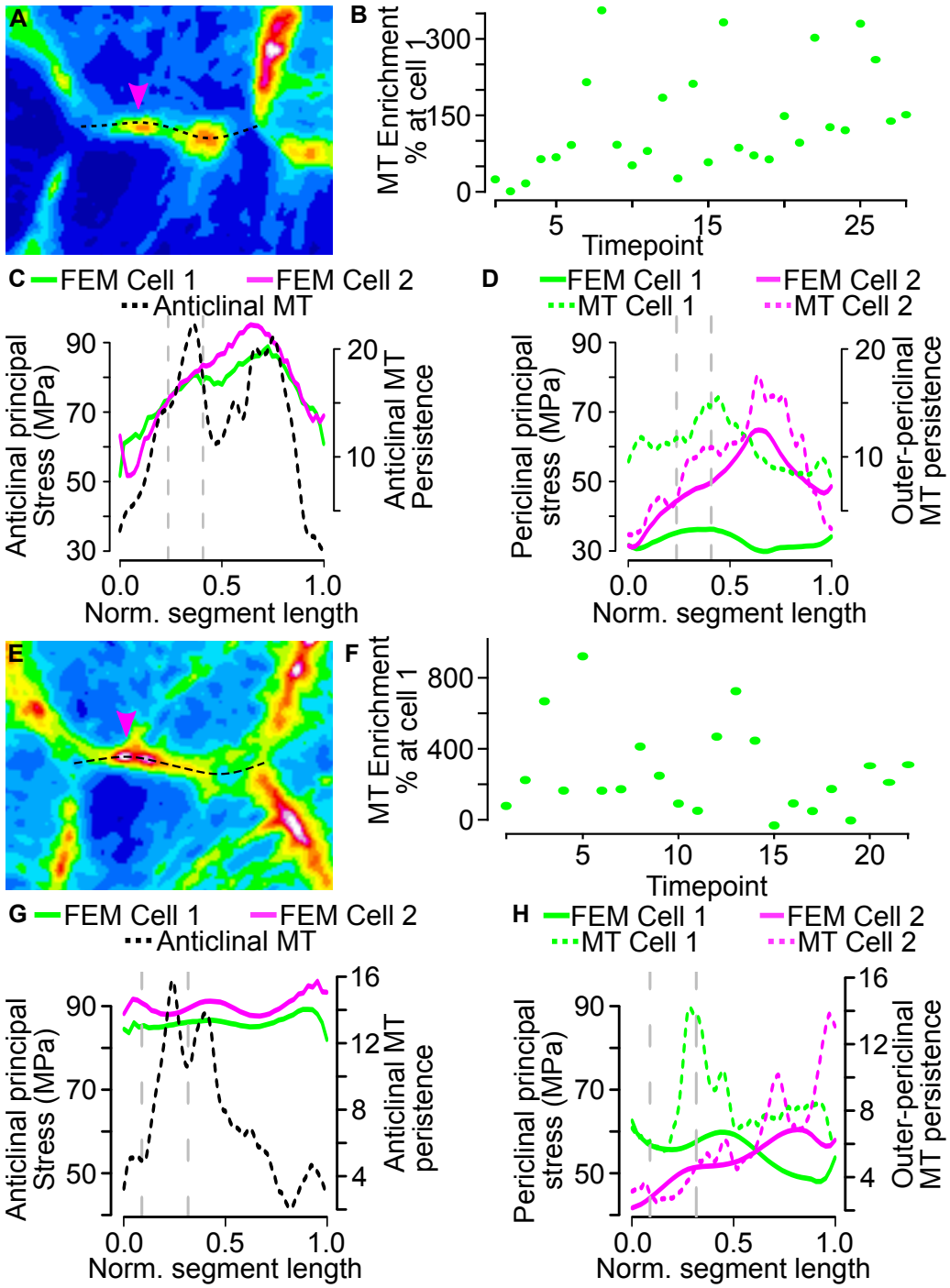
A
B
MT Enrichment % at cell 1
300
150
0
5
15
25
Timepoint
C
FEM Cell 1
FEM Cell 2
Anticlinal MT
Anticlinal principal Stress (MPa)
90
70
50
30
20
10
Anticlinal MT Persistence
0.0
0.5
1.0
Norm. segment length
D
FEM Cell 1
FEM Cell 2
MT Cell 1
MT Cell 2
Periclinal principal stress (MPa)
Outer-periclinal MT persistence
Norm. segment length
E
F
MT Enrichment % at cell 1
800
400
0
5
10
15
20
Timepoint
G
FEM Cell 1
FEM Cell 2
Anticlinal MT
Anticlinal principal Stress (MPa)
16
12
8
4
Anticlinal MT peristence
Norm. segment length
H
FEM Cell 1
FEM Cell 2
MT Cell 1
MT Cell 2
Periclinal principal stress (MPa)
Outer-periclinal MT persistence
Norm. segment length

Fig. 4.S4.3. Additional microtubule and predicted stress correlations. (A,E) Summed projection of time-lapse microtubule signal shows hotspots at region where a new lobe will form (Magenta arrowhead. (B, F) Microtubule enrichement plotted as the percent enrichment of cell 1 (future convex) to cell 2 (future concave) as a function of time. (C-G) Correlation analysis of anticlinal cell wall stress of the convex lobing cell (green) and the concave lobing cell 2 (magenta) and the anticlinal microtubule persistence (black dashed line) as a function of location along the cell segment. (D-H) Correlation analysis of periclinal wall cell stress (green) and periclinal microtubule persistence (green - dashed) of future convex cell 1. Correlation analysis of periclinal wall stress (magenta) and periclinal microtubule persistence (magenta - dashed) of future concave cell 2.

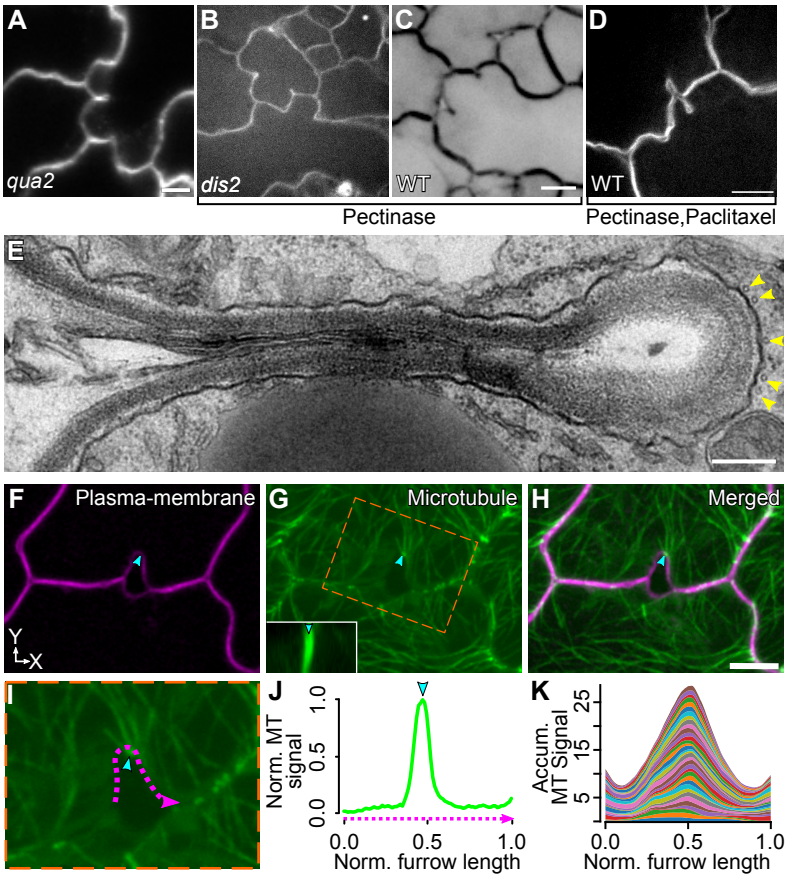

Fig. 4.5. Development of a semi-cell autonomous system to analyze lobe formation. Cell invaginations mirror lobe formation events and are cellulose and microtubule dependent. (A) The pectin deficient mutant, *qua2-1*, develops cell invaginations in pavement cells. (B-C) Pectinase treatment promote furrow formation in *dis2* and WT. (E) TEM images of *dis2* furrows revealed microtubules at the apex of these invaginations (yellow arrowheads). (D) In rare events, opposing furrows can be seen with the addition of paclitaxel to wild-type seedlings in low-light conditions showing the capability of both cells to undergo shape change. (F) Plasma-membrane image show the geometry of a nascent furrow used to obtain high resolution images of microtubules organization (G). Similarly to lobes, microtubules splay across the anticlinal (G - insert) and outer-periclinal wall (H). (I) Line scans of the microtubule signal within the furrow were conducted. (J) Each plot was normalized from 0 to 1 (J) to aid in a population level analysis. (K) Microtubules show a high degree of preference to the apex of these highly symmetrical invaginations. Scale bar = 10 μm (A, C, D); 250 nm (E); 5 μm (H).

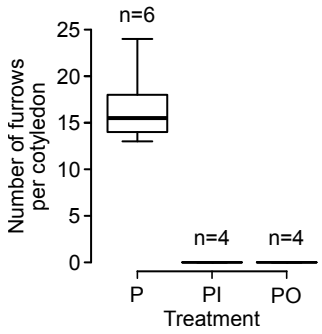

Fig. 4.S5.1. Furrow formation is blocked with interference of the cellulose or microtubule systems. P – pectinase, O – Oryzalin, and I – Isoxaben at 0.2%, 10 nM, and 5 nM concentration respectively.

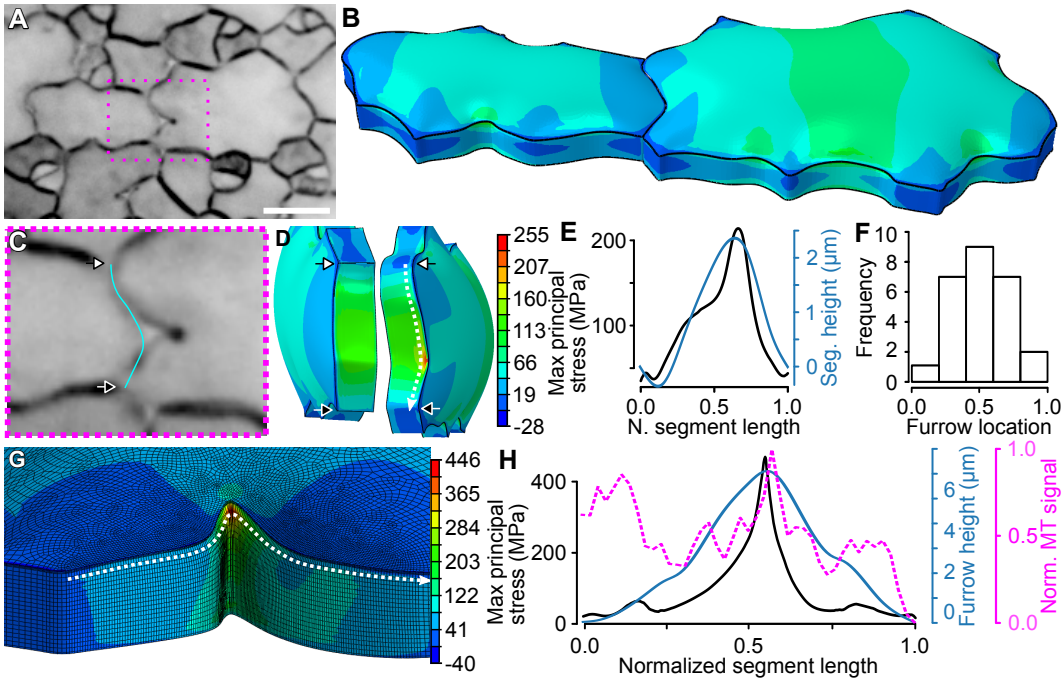

Fig. 4.6. Stress dictates the location for furrow formation. (A) Live-cell image of 2 DAG seedling after being exposed to 0.2% pectinase for 24 hours showing a nascent furrow. (B) Finite element model of the un-furrowed cell pair was constructed from (A) by utilizing the shape of the neighboring cell – cyan line; (C) close-up view. (D) Face-view of the anticlinal walls showing cell wall predicted stresses along the segments with a clear hotspot on the furrowing cell. (E) The stress of the furrowing cell was dependent on the shape of the segment. (F) Population level analysis of furrow location along straight segments revealed a bias towards the center of the segment a place of predicted higher stress. (G) Stress maxima is predicted to be located at the apex of the furrow and this location co-localizes to both the shape of the furrow and microtubule peak (H). Scale bar = 10 μm.

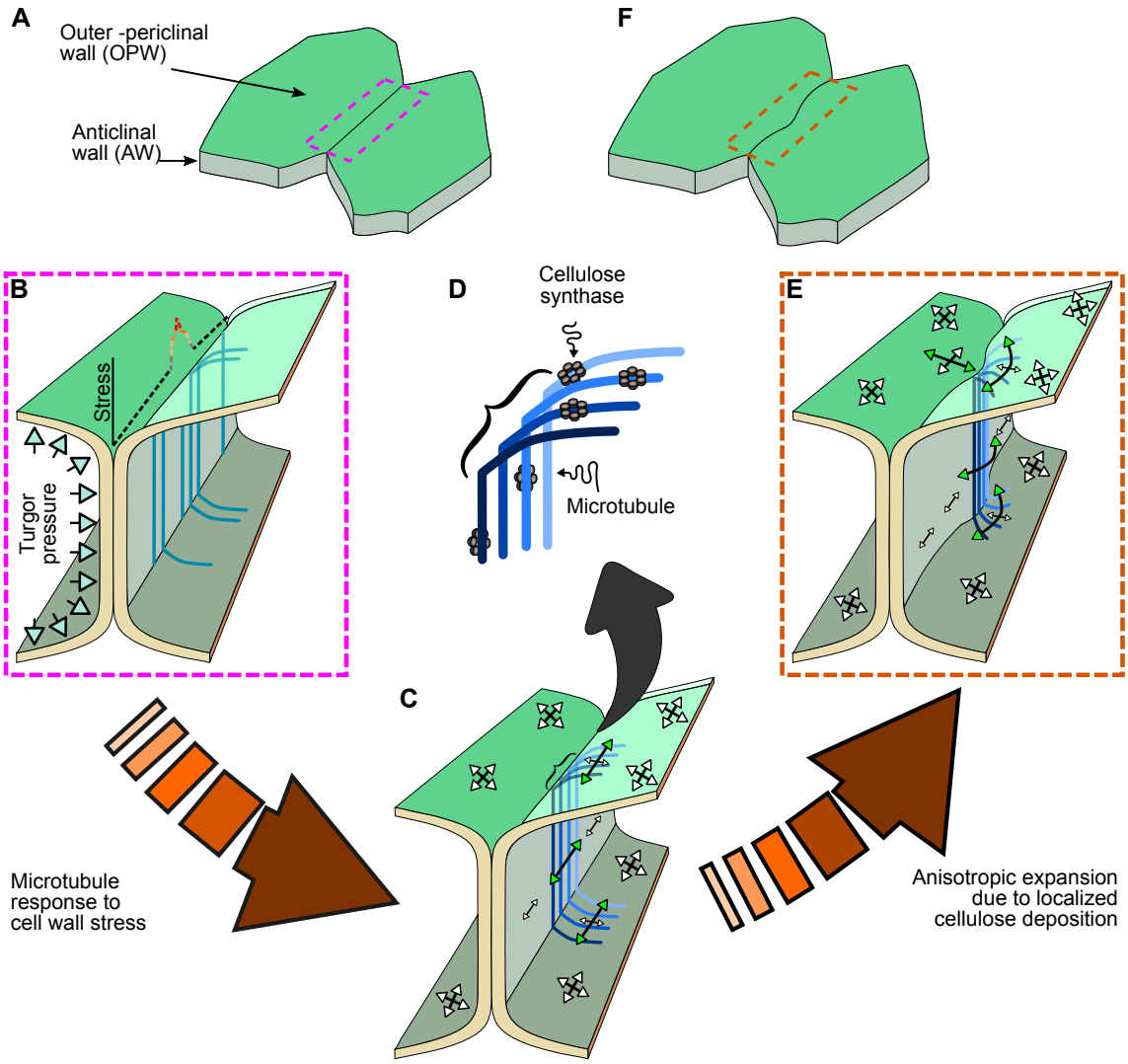

Fig. 4.7. Cellulose and microtubule dependent shape change in response to cell wall stresses. (A) Model of neighboring epidermal cells prior and after (F) lobe formation. (B) Magnified region of dashed box from (A) showing a cross section view of the anticlinal walls from each cell with microtubules throughout the segment. Geometry based cell wall stresses are predicted to be maxima at the center of the segment. (C) Anisotropic expansion is perpendicular to cellulose deposition. (D) Zoom-in view of microtubules serving as tracks for cellulose synthase. (E) Local anisotropic expansion is maintained after lobe formation resulting in lobe expansion.

REFERENCES

REFERENCES

[1] Y. Y. Li, P. B. Reich, B. Schmid, N. Shrestha, X. Feng, T. Lyu, B. S. Maitner, X. Xu, Y. Y. Li, D. Zou, Z.-H. Tan, X. Su, Z. Tang, Q. Guo, X. Feng, B. J. Enquist, and Z. Wang, "Leaf size of woody dicots predicts ecosystem primary productivity," *Ecology Letters*, vol. n/a, no. n/a, 2019. [Online]. Available: https://onlinelibrary.wiley.com/doi/abs/10.1111/ele.13503

[2] S. Savaldi-Goldstein, C. Peto, and J. Chory, "The epidermis both drives and restricts plant shoot growth," *Nature*, 2007.

[3] R. V. Vőfély, J. Gallagher, G. D. Pisano, M. Bartlett, and S. A. Braybrook, "Of puzzles and pavements: a quantitative exploration of leaf epidermal cell shape," 2018.

[4] D. B. Szymanski, "The kinematics and mechanics of leaf expansion: New pieces to the Arabidopsis puzzle," *Current Opinion in Plant Biology*, vol. 22, pp. 141–148, 2014. [Online]. Available: http://dx.doi.org/10.1016/j.pbi.2014.11.005

[5] W. J. Armour, D. A. Barton, A. M. Law, and R. L. Overall, "Differential Growth in Periclinal and Anticlinal Walls during Lobe Formation in Arabidopsis Cotyledon Pavement Cells," *The Plant Cell*, 2015.

[6] C. Zhang, L. E. Halsey, and D. B. Szymanski, "The development and geometry of shape change in Arabidopsis thaliana cotyledon pavement cells," *BMC Plant Biology*, vol. 11, 2011. [Online]. Available: http://www.biomedcentral.com/1471-2229/11/27

[7] J. Elsner, M. Michalski, and D. Kwiatkowska, "Spatiotemporal variation of leaf epidermal cell growth: A quantitative analysis of Arabidopsis thaliana wild-type and triple cyclinD3 mutant plants," *Annals of Botany*, 2012.

[8] M. Andriankaja, S. Dhondt, S. DeBodt, H. Vanhaeren, F. Coppens, L. DeMilde, P. Mühlenbock, A. Skirycz, N. Gonzalez, G. T. Beemster, and D. Inzé, "Exit from Proliferation during Leaf Development in Arabidopsis thaliana: A Not-So-Gradual Process," *Developmental Cell*, 2012.

[9] B. M. Jordan and J. Dumais, "Biomechanics of Plant Cell Growth," *Encyclopedia of Life Sciences*, no. July, 2010.

[10] R. Gutierrez, J. J. Lindeboom, A. R. Paredez, A. M. C. Emons, and D. W. Ehrhardt, "Arabidopsis cortical microtubules position cellulose synthase delivery to the plasma membrane and interact with cellulose synthase trafficking compartments," *Nature Cell Biology*, 2009.

[11] M. Fujita, R. Himmelspach, J. Ward, A. Whittington, N. Hasenbein, C. Liu, T. T. Truong, M. E. Galway, S. D. Mansfield, C. H. Hocart, and G. O. Wasteneys, "The anisotropy1 D604N mutation in the Arabidopsis cellulose synthase1 catalytic domain reduces cell wall crystallinity and the velocity of cellulose synthase complexes," *Plant Physiology*, vol. 162, no. 1, pp. 74–85, 2013.

[12] L. C. Morejohn, T. E. Bureau, J. Molè-Bajer, A. S. Bajer, and D. E. Fosket, "Oryzalin, a dinitroaniline herbicide, binds to plant tubulin and inhibits microtubule polymerization in vitro," *Planta*, vol. 172, no. 2, pp. 252–264, 1987.

[13] A. R. Paredez, S. Persson, D. W. Ehrhardt, and C. R. Somerville, "Genetic Evidence That Cellulose Synthase Activity Influences Microtubule Cortical Array Organization," *PLANT PHYSIOLOGY*, 2008.

[14] J. Mathur, "Mutations in Actin-Related Proteins 2 and 3 Affect Cell Shape Development in Arabidopsis," *THE PLANT CELL ONLINE*, 2003.

[15] J.-L. Qiu, "The Arabidopsis SPIKE1 Gene Is Required for Normal Cell Shape Control and Tissue Development," *THE PLANT CELL ONLINE*, 2002.

[16] Y. Fu, Y. Gu, Z. Zheng, G. Wasteneys, and Z. Yang, "Arabidopsis interdigitating cell growth requires two antagonistic pathways with opposing action on cell morphogenesis," *Cell*, 2005.

[17] Y. Fu, "The ROP2 GTPase Controls the Formation of Cortical Fine F-Actin and the Early Phase of Directional Cell Expansion during Arabidopsis Organogenesis," *THE PLANT CELL ONLINE*, 2002.

[18] J. C. Ambrose, T. Shoji, A. M. Kotzer, J. A. Pighin, and G. O. Wasteneys, "The Arabidopsis CLASP Gene Encodes a Microtubule-Associated Protein Involved in Cell Expansion and Division," *THE PLANT CELL ONLINE*, 2007.

[19] D. H. Burk, "A Katanin-like Protein Regulates Normal Cell Wall Biosynthesis and Cell Elongation," *THE PLANT CELL ONLINE*, 2001.

[20] B. Galatis, "Microtubules and epithem-cell morphogenesis in hydathodes of Pilea cadierei," *Planta*, 1988.

[21] E. Panteris, P. Apostolakos, and B. Galatis, "Microtubules and morphogenesis in ordinary epidermal cells of Vigna sinensis leaves," *Protoplasma*, 1993.

[22] Y. Fu, T. Xu, L. Zhu, M. Wen, and Z. Yang, "A ROP GTPase Signaling Pathway Controls Cortical Microtubule Ordering and Cell Expansion in Arabidopsis," *Current Biology*, 2009.

[23] P. Fayant, O. Girlanda, Y. Chebli, C. É. Aubin, I. Villemure, and A. Geitmann, "Finite element model of polar growth in pollen tubes," *Plant Cell*, vol. 22, no. 8, pp. 2579–2593, 2010.

[24] M. Yanagisawa, A. S. Desyatova, S. A. Belteton, E. L. Mallery, J. A. Turner, and D. B. Szymanski, "Patterning mechanisms of cytoskeletal and cell wall systems during leaf trichome morphogenesis," *Nature Plants*, 2015.

[25] M. Majda, P. Grones, I. M. Sintorn, T. Vain, P. Milani, P. Krupinski, B. Zagórska-Marek, C. Viotti, H. Jönsson, E. J. Mellerowicz, O. Hamant, and S. Robert, "Mechanochemical Polarization of Contiguous Cell Walls Shapes Plant Pavement Cells," *Developmental Cell*, 2017.

[26] A. J. Bidhendi, B. Altartouri, F. P. Gosselin, and A. Geitmann, "Mechanical stress initiates and sustains the morphogenesis of wavy leaf epidermal cells," *bioRxiv*, vol. 2019, no. May, p. 563403, 2019. [Online]. Available: https://www.biorxiv.org/content/early/2019/03/04/563403.full.pdf

[27] A. Sapala, A. Runions, A. L. Routier-Kierzkowska, M. D. Gupta, L. Hong, H. Hofhuis, S. Verger, G. Mosca, C. B. Li, A. Hay, O. Hamant, A. H. Roeder, M. Tsiantis, P. Prusinkiewicz, and R. S. Smith, "Why plants make puzzle cells, and how their shape emerges," *eLife*, 2018.

[28] A. J. Bidhendi and A. Geitmann, "Geometrical Details Matter for Mechanical Modeling of Cell Morphogenesis," *Developmental Cell*, vol. 50, no. 1, pp. 117–125.e2, 2019. [Online]. Available: https://doi.org/10.1016/j.devcel.2019.05.001

[29] S. Belteton, M. G. Sawchuk, B. S. Donohoe, E. Scarpella, and D. B. Szymanski, "Reassessing the roles of PIN proteins and anticlinal microtubules during pavement cell morphogenesis," *Plant Physiology*, 2018.

[30] E. Jacques, J. P. Verbelen, and K. Vissenberg, "Review on shape formation in epidermal pavement cells of the Arabidopsis leaf," *Functional Plant Biology*, vol. 41, no. 9, pp. 914–921, 2014.

[31] E. E. Kuchen, S. Fox, P. B. De Reuille, R. Kennaway, S. Bensmihen, J. Avondo, G. M. Calder, P. Southam, A. Bangham, and E. Coen, "Generation of leaf shape through early patterns of growth and tissue polarity," *Science*, 2012.

[32] J. Elsner, M. Lipowczan, and D. Kwiatkowska, "Differential growth of pavement cells of Arabidopsis thaliana leaf epidermis as revealed by microbead labeling," *American Journal of Botany*, 2018.

[33] T. Xu, M. Wen, S. Nagawa, Y. Fu, J. G. Chen, M. J. Wu, C. Perrot-Rechenmann, J. Friml, A. M. Jones, and Z. Yang, "Cell surface- and Rho GTPase-based auxin signaling controls cellular interdigitation in Arabidopsis," *Cell*, 2010.

[34] J. H. Wong, T. Kato, S. A. Belteton, R. Shimizu, N. Kinoshita, T. Higaki, Y. Sakumura, D. B. Szymanski, and T. Hashimoto, "Basic proline-rich protein-mediated microtubules are essential for lobe growth and flattened cell geometry," *Plant Physiology*, vol. 181, no. 4, pp. 1535–1551, 2019.

[35] A. J. Bidhendi, B. Altartouri, F. P. Gosselin, and A. Geitmann, "Mechanical Stress Initiates and Sustains the Morphogenesis of Wavy Leaf Epidermal Cells," *Cell Reports*, vol. 28, no. 5, pp. 1237–1250.e6, 2019.

[36] K. T. Haas, R. Wightman, E. M. Meyerowitz, and A. Peaucelle, "Pectin homogalacturonan nanofilament expansion drives morphogenesis in plant epidermal cells," *Science*, vol. 367, no. 6481, pp. 1003–1007, 2020. [Online]. Available: https://www.sciencemag.org/lookup/doi/10.1126/science.aaz5103

[37] A. Kotzer and G. Wasteneys, "Mechanisms behind the puzzle: microtubule–microfilament cross-talk in pavement cell formationThis review is one of a selection of papers published in the Special Issue on Plant Cell Biology." *Canadian Journal of Botany*, 2006.

[38] W. Qiao, M. Mooney, A. J. Bird, D. R. Winge, and D. J. Eide, "Zinc binding to a regulatory zinc-sensing domain monitored in vivo by using FRET," *Proceedings of the National Academy of Sciences*, 2006.

[39] A. T. Whittington, O. Vugrek, K. J. Wei, N. G. Hasenbein, K. Sugimoto, M. C. Rashbrooke, and G. O. Wasteneys, "MOR1 is essential for organizing cortical microtubules in plants," *Nature*, vol. 411, no. 6837, pp. 610–613, 2001.

[40] S. Bouton, "QUASIMODO1 Encodes a Putative Membrane-Bound Glycosyltransferase Required for Normal Pectin Synthesis and Cell Adhesion in Arabidopsis," *THE PLANT CELL ONLINE*, 2002.

[41] E. Parre and A. Geitmann, "Pectin and the role of the physical properties of the cell wall in pollen tube growth of Solanum chacoense," *Planta*, vol. 220, no. 4, pp. 582–592, 2005.

[42] E. Panteris and B. Galatis, "The morphogenesis of lobed plant cells in the mesophyll and epidermis: Organization and distinct roles of cortical microtubules and actin filaments," 2005.

[43] H. Buschmann and C. W. Lloyd, "Arabidopsis mutants and the network of microtubule-associated functions," *Molecular Plant*, vol. 1, no. 6, pp. 888 – 898, 2008. [Online]. Available: http://www.sciencedirect.com/science/article/pii/S1674205214604470

[44] E. Kawamura, "MICROTUBULE ORGANIZATION 1 Regulates Structure and Function of Microtubule Arrays during Mitosis and Cytokinesis in the Arabidopsis Root," *PLANT PHYSIOLOGY*, 2005.

[45] S. Verger, Y. Long, A. Boudaoud, and O. Hamant, "A tension-adhesion feedback loop in plant epidermis," *eLife*, 2018.

[46] T.-C. Wu, S. Belteton, J. Pack, D. B. Szymanski, and D. Umulis, "LobeFinder: a convex hull-based method for quantitative boundary analyses of lobed plant cells," *Plant Physiology*, 2016.

[47] M. Nakamura and T. Hashimoto, "A mutation in the Arabidopsis -tubulin-containing complex causes helical growth and abnormal microtubule branching," *Journal of Cell Science*, 2009.

[48] Z. Kong, T. Hotta, Y.-R. J. Lee, T. Horio, and B. Liu, "The -Tubulin Complex Protein GCP4 Is Required for Organizing Functional Microtubule Arrays in Arabidopsis thaliana," *The Plant Cell*, 2010.

[49] A. M. Kotzer and G. O. Wasteneys, "Mechanisms behind the puzzle: Microtubule-microfilament cross-talk in pavement cell formation," *Canadian Journal of Botany*, vol. 84, no. 4, pp. 594–603, 2006.

[50] F. Tolmie, A. Poulet, J. McKenna, S. Sassmann, K. Graumann, M. Deeks, and J. Runions, "The cell wall of Arabidopsis thaliana influences actin network dynamics," *Journal of Experimental Botany*, 2017.

[51] M. C. Jarvis, S. P. Briggs, and J. P. Knox, "Intercellular adhesion and cell separation in plants," 2003.

[52] C. M. Rounds, E. Lubeck, P. K. Hepler, and L. J. Winship, "Propidium Iodide Competes with Ca ²⁺ to Label Pectin in Pollen Tubes and Arabidopsis Root Hairs," *Plant Physiology*, 2011.

[53] A. Sampathkumar, P. Krupinski, R. Wightman, P. Milani, A. Berquand, A. Boudaoud, O. Hamant, H. Jönsson, and E. M. Meyerowitz, "Subcellular and supracellular mechanical stress prescribes cytoskeleton behavior in Arabidopsis cotyledon pavement cells," *eLife*, 2014.

[54] D. W. Ehrhardt and S. L. Shaw, "Microtubule Dynamics and Organization in the Plant Cortical Array," *Annual Review of Plant Biology*, vol. 57, no. 1, pp. 859–875, 2006.

[55] S. Zhou, Q. Chen, X. Li, and Y. Li, "MAP65-1 is required for the depolymerization and reorganization of cortical microtubules in the response to salt stress in Arabidopsis," *Plant Science*, vol. 264, no. August, pp. 112–121, 2017. [Online]. Available: http://dx.doi.org/10.1016/j.plantsci.2017.09.004

[56] S. O. Kotchoni, T. Zakharova, E. L. Mallery, J. Le, S. E.-D. El-Assal, and D. B. Szymanski, "The Association of the Arabidopsis Actin-Related Protein2/3 Complex with Cell Membranes Is Linked to Its Assembly Status But Not Its Activation," *PLANT PHYSIOLOGY*, 2009.

[57] M. Pastuglia, "Tubulin Is Essential for Microtubule Organization and Development in Arabidopsis," *THE PLANT CELL ONLINE*, 2006.

[58] M. Fendrych, V. Žárský, L. Synek, T. Pečenková, H. Toupalová, R. Cole, E. Drdová, J. Nebesářová, M. Sedinová, M. Hála, and J. E. Fowler, "The Arabidopsis exocyst complex is involved in cytokinesis and cell plate maturation," *Plant Cell*, vol. 22, no. 9, pp. 3053–3065, 2010.

[59] M. Nakamura, "Microtubule nucleating and severing enzymes for modifying microtubule array organization and cell morphogenesis in response to environmental cues," 2015.

[60] S. E. D. El-Assal, J. Le, D. Basu, E. L. Mallery, and D. B. Szymanski, "Distorted2 encodes an ARPC2 subunit of the putative Arabidopsis ARP2/3 complex," *Plant Journal*, 2004.

[61] D. G. Oppenheimer, M. A. Pollock, J. Vacik, D. B. Szymanski, B. Ericson, K. Feldmann, and M. D. Marks, "Essential role of a kinesin-like protein in Arabidopsis trichome morphogenesis," *Proceedings of the National Academy of Sciences of the United States of America*, vol. 94, no. 12, pp. 6261–6266, 1997.

[62] E. Bayer, C. Thomas, and A. Maule, "Symplastic domains in the Arabidopsis shoot apical meristem correlate with PDLP1 expression patterns," *Plant Signaling & Behavior*, vol. 3, no. 10, pp. 853–855, 2008.

[63] B. K. Nelson, X. Cai, and A. Nebenführ, "A multicolored set of in vivo organelle markers for co-localization studies in Arabidopsis and other plants," *Plant Journal*, vol. 51, no. 6, pp. 1126–1136, 2007.

[64] I. F. Sbalzarini and P. Koumoutsakos, "Feature point tracking and trajectory analysis for video imaging in cell biology," *Journal of Structural Biology*, vol. 151, no. 2, pp. 182–195, 2005.

[65] E. Forouzesh, A. Goel, S. A. MacKenzie, and J. A. Turner, "In vivo extraction of Arabidopsis cell turgor pressure using nanoindentation in conjunction with finite element modeling," *Plant Journal*, 2013.

[66] G. Zsivanovits, A. J. MacDougall, A. C. Smith, and S. G. Ring, "Material properties of concentrated pectin networks," *Carbohydrate Research*, vol. 339, no. 7, pp. 1317–1322, 2004.

VITA

SAMUEL A. BELTETON

EDUCATION

Plant molecular biology, PhD

2020 Purdue University, West Lafayette, IN

Department: Botany and plant pathology

School: Agronomy

Microbiology, BS

2012 Purdue University, West Lafayette, IN

Department: Microbiology

School: Biology

PUBLICATIONS

Plant Physiology, 2019

Jeh Haur Wong, Takehide Kato, **Samuel A. Belteton**, Rie Shimizu, Nene Kinoshita, Takumi Higaki, Yuichi Sakumura, Daniel B. Szymanski and Takashi Hashimoto
Basic Proline-Rich Protein-Mediated Microtubules Are Essential for Lobe Growth and Flattened Cell Geometry.
Contribution: Experimental design. Image acquisition. Data analysis. Manuscript preparation

Plant Physiology, 2017

Belteton, S., Sawchuk, M. G., Donohoe, B. S., Scarpella, E., Szymanski, D. B.
Reassessing the roles of PIN proteins and anticlinal microtubules during pavement cell morphogenesis.
Contribution: Experimental design. Image acquisition. Software creation. Data analysis. Manuscript preparation
Shared cover image

Plant Physiology, 2016

Wu, T.*, **Belteton, S.***, Lunsford, J., Szymanski, D.B., Umulis, D.
Quantitative image analysis of pavement cell morphogenesis with *LobeFinder*.
*Authors contributed equally.
Contribution: Image acquisition. Software testing, design, and troubleshooting. Manually curated pavement cell results and analysis. Manuscript preparation.
Cover Image

BMC Bioinformatics, 2016

Delibaltov D.L., Gaur, U., Kim, J., Kourakis, M., Newman-Smith, E., Smith W., **Belteton, S.**, Szymanski, D.B., Manjunath, B.S.
CellECT: Cell Evolution Capturing Tool.
Contribution: Image acquisition. Comparison of software results with manually curated pavement cells. Software troubleshooting. Manuscript preparation.

Nature Plant, 2015

Yanagisawa, M., Desyatova, A.S., **Belteton, S.**, M., M.E., Turner, J.A., and Szymanski, D.B.
Patterning mechanisms of cytoskeletal and cell wall systems during leaf trichome morphogenesis.
Contribution: Created a new 4D reflection imaging method. Cell wall thickness measurements from TEM. Manuscript preparation.

AWARDS

2019 Weier Outstanding Graduate Student.

2019 22nd Penn State Plant Cell Dynamics VIII travel grant recipient.

2018 Purdue Research Foundation fellowship.

2017 Midwest plant cell dynamics travel grant recipient.

2016 URM-ICAR travel grant recipient.

TEACHING EXPERIENCE

Fall 2017 Agronomy 321; Genetics.
Purdue University. West Lafayette, IN.

2015||2016 Botany 110; Introduction to plant science.
Purdue University. West Lafayette, IN.

June 2014 Long-term live-cell imaging workshop.
24 participant
Midwest plant cell dynamic conference. Madison, WI.

LABORATORY MENTORING

2017||2018 Sarah Cryer.
Pectinase effect on cell adhesion in newly germinated *Arabidopsis* seedlings.

June 2017 Ethan Stump & Joseph Hsu.
Molecular agriculture summer institutes (MASI) program.

2014||2015 Cody Thorson.
Developmental morphology of *ARPC2* mutant at cellular and organ levels in *Arabidopsis* embryonic leaves.

2013||2015 Adam Fessenden.
[1]Forward genetic screen for subtle distorted trichome mutants in *Arabidopsis*.
[2]Summer undergraduate research fellowship (SURF) program.

2013||2015 Sarah Mendoza.
[1]Effect of mCherry-tubulin on *Arabidopsis* epidermal cell morphogenesis.
[2]Molecular identification of *PIN*s single, double, triple, and quadruple mutants.

2012||2014 Austin Blackwell & Michael Kuhn.
Molecular identification of *PIN*s single, double, triple, and quadruple mutants.

2013 Brian Anderson.
Quantification of mature epidermal cell morphogenics in *Arabidopsis* embryonic leaves across known epidermal cell shape mutants.

SYNERGISTIC ACTIVITIES

2016||2018 Council elected commissioner of the Go Green Committee.
West Lafayette, IN.

November 2018 Oral presentation.
The biomechanics of epidermal cell morphogenesis.
Botany and Plant Pathology Research Showcase. West Lafayette, IN.

November 2018 Poster presentation.[1,2]
Building a knowledge base to enable plant architecture engineering.
Authors: **Samuel A. Belteton**, Jing Li, Tae Yoon Kim, Joe Turner, Daniel B. Szymanski.
[1]Botany and Plant Pathology Research Showcase. West Lafayette, IN
[2]Plant and engineering poster session. West Lafayette, IN

May 2018
Oral Presentation.
The biomechanics of epidermal cell morphogenesis.
Cellular Dynamics symposium. West Lafayette, IN

May 2018
Poster presentation.
Experimental and computational analyses of pavement cell biomechanics.
Authors: **Samuel A. Belteton**, Jiaxiang Jiang, B.S. Manjunath, Joseph Turner, Daniel B. Szymanski.
Midwest Plant Cell Dynamics. Madison, WI.

February 2018
Poster presentation.
Developmental and intracellular mechanisms of lobe initiation in cotyledon pavement cells.
Authors: **Samuel A. Belteton**, Tzu-Ching Wu, Megan Sawchuk, Ehsan Rezaei, Joseph Turner, David M. Umulis, Enrico Scarpella, Daniel B. Szymanski.
BisQue + Scalable Image Informatic workshop. Santa Barbara, CA

October 2017
Poster presentation.
Midwest membrane trafficking and signal symposium.
Purdue University. West Lafayette, IN.

May 2017
Oral and poster presentation.
Midwest plant cell biology.
Madison, WI.

April 2017
Oral and poster presentation.
Computational Science and Engineering Student Conference.
Purdue University. West Lafayette, IN.

April 2017
Poster presentation judge.
Purdue undergraduate research and poster symposium.
Purdue University. West Lafayette, IN.

March 2017
Poster presentation judge.
Lafayette regional science and engineering fair.
Purdue University. West Lafayette, IN.

June 2016
Poster presentation.
27th International Conference on Arabidopsis Research (ICAR).
Gyeong Ju, Korea.

April 2015
Oral presentation.
3D registration and alignment necessity for cell expansion analysis.
Plant Image Analysis Solution Workshop. Madison, WI.

June 2014
Oral presentation.
ARP2/3 mediated patterning of cytoskeletal and cell wall systems during leaf trichome morphogenesis.
Midwest Plant Cell Dynamics Meeting, Madison, WI.